FREIE UNIVERSITÄT

Fluorine, Fluid and Greisen Formation

A Dissertation

Submitted in Partial Fulfilment of the

Requirements for the Degree of Doctor

to the Department of Earth Sciences

of Freie Universität Berlin

by

SHILEI QIAO

Berlin, 2024

Freie Universität Berlin

Department of Earth Sciences

Institute of Geological Sciences

Supervisor: Prof. Dr. Timm John

Second examiner: Dr. Johannes C. Vrijmoed

Reviewer:

Prof. Dr. Timm John

Prof. Dr. Mathias Burish

Dr. Johannes C. Vrijmoed

Date of Defense: 06. 12. 2024

Eigenständigkeitserklärung:

Ich erkläre hiermit, dass ich die vorliegende Dissertation selbstständig und ohne unerlaubte Hilfe angefertigt habe. Ich habe ChatGPT verwendet, um die Kapitel 1 und 5 sprachlich zu verbessern. Jegliche verwendeten Hilfsmittel und Quellen sind im Literaturverzeichnis vollständig aufgeführt. Die aus den benutzten Quellen wörtlich oder inhaltlich entnommenen Stellen sind als solche kenntlich gemacht. Des Weiteren erkläre ich, dass die Arbeit bisher weder in gleicher noch in ähnlicher Form einer Prüfungsbehörde vorlag.

Declaration of academic honesty:

I hereby certify that this thesis has been composed by me and is based on my own work, unless stated otherwise. I used ChatGPT to improve the readability of chapters 1 and 5. All references have been quoted, and all sources of information have been specifically acknowledged. I further declare that I have not submitted this thesis at any other institution in order to obtain a degree.

_____

Shilei Qiao

Berlin, 10, 2024

Contents

Fluorine, Fluid and Greisen Formation

Abstract

Fluid-rock interaction is a fundamental process in the earth system, capable of altering the chemical and physical properties of wall rocks, which in turn significantly influences the large-scale exposure of fluid-altered rock, geophysical observations and hydrothermal ore deposits. Greisenization represents such a fluid-rock interaction characterized by the replacement of biotite + feldspar by quartz + white mica ± topaz ± fluorite, which links fluid-rock interaction to the ore formation, particularly facilitating significant enrichments in W, Sn, and Li. However, the factors controlling greisen variation and the fluid evolution are not well understood. In this dissertation, I integrate natural sample analysis and a reactive transport model to investigate the greisenization process. The results indicate that the initial fluid composition, particularly F concentration and pH value, governs the variation of greisen. Additionally, boiling may serve as a mechanism to introduce F-rich fluid. Further, fluorine content in topaz is a probe to the F concentration change of fluid. This thesis emphasizes a novel perspective on how F influences the process of greisenization from natural observations to numerical modeling, which further contributes to a better understanding of greisen-related ore formation and F-related processes.

The first scientific section presents work on the Zinnwald/Cínovec quartz-topaz greisen, a typical example of fluid-rock interactions involving F-rich fluids. A transect with a width of 12 cm from this deposit presents a sequence of quartz-topaz greisen and weakly altered rhyolite. Mass balance calculation for this transect indicates a net gain of F, Si, etc. during greisenization. Fluid inclusions evidence suggests that boiling occurred during or before greisenization. To explain the observation, I propose a two-stage greisenization model. Initially, fluid boiling induces the phase separation of HF-rich vapor and brine. The vapor reacts with feldspar and biotite to form quartz and topaz, while mineral replacement creates significant transient porosity, which is then filled by brine and later sealed by the precipitation of quartz and fluorite due to oversaturation. This study underscores that fluid boiling, which introduces F-rich fluids, is essential for the formation of quartz-topaz-rich greisen.

Observations on Zinnwald/Cínovec quartz-topaz greisen reveal that the process of boiling introduces the F-rich fluid. However, the evolution of fluid composition is equally crucial to the mobility of metals of interest (e.g., W, Sn). In this case, topaz, a key F-bearing phase in quartz-topaz greisen, can be used to trace the fluid evolution, especially in terms of F content. In the second scientific section, I performed measurements of Raman spectrometry on topaz crystals collected from different locations. The results reveal that the distances of Raman bands shifts around 155 and 562 cm^{-1} correlate with F concentration by a linear correlation ($y = 0.329x – 113.6$, where y represents F concentration and x the

distance of Raman bands shifts around 155 and 562 cm^{-1}). Two types of topazes from the Zinnwald/Cínovec greisen profile were recognized based on CL imaging. The systematic F concentration difference of 0.4 wt. % among these two types of greisen indicates the F content change in the fluid equilibrated with greisen. This approach provides a newly practical method to determine F concentration in topaz, which could be used to trace the temporal (and/or spatial) evolution of aqueous F content during greisenization.

The case study of Zinnwald/Cínovec quartz-topaz greisen offers valuable insights into the formation of quartz-topaz greisen. However, the factors controlling the variation between quartz-topaz and quartz-mica greisen are not well understood. Based on the natural sample study, the third section of this dissertation introduces a reactive transport model to constrain the parameters governing the development of distinct greisen assemblages. The infiltrating fluid with a lower pH value and lower F concentration result in the formation of greisen characterized by a sequence of quartz-topaz and quartz-mica. In contrast, acdic fluid enriched in F (>0.015 mol/kg), lead to mica-free greisen formation. Additionally, the results of the numerical modeling suggest that quartz-topaz greisen has a higher porosity (14 %) compared to quartz-mica greisen (8 %), allowing that larger fluid volumes to pass through quartz-topaz greisen. These findings enhance our understanding of greisen variation and fluid evolution, which are critical to studying greisen-related ore formation.

In conclusion, the comprehensive study emphasizes the significance of quartz-topaz greisen in greisen systems, particularly its F-rich environment, which provides potential for rare metal enrichment. By examining processes from the mineral to the bulk rock scale, this work demonstrates that F plays a critical role in greisen systems. The novel method of determining F concentration in topaz through Raman spectroscopy enables the precise measurement. Moreover, the reactive transport model offers detailed constraints on fluid evolution during greisenization, improving the understanding of both greisen formation and associated ore deposits, such as those of W, Nb, and Ta. This dissertation covers a wide spectrum of greisen, providing valuable insights into the greisenization process.

Kurzfassung

Die Wechselwirkung zwischen Fluiden und Gesteinen ist ein grundlegender Prozess im System Erde, der sowohl die chemischen als auch die physikalischen Eigenschaften von Gesteinen verändern kann. Diese Interaktionen spielen eine bedeutende Rolle bei der großflächigen Verbreitung von fluidverändertem Gestein, geophysikalischen Beobachtungen und der Entstehung hydrothermaler Erzvorkommen. Ein Beispiel für einen solchen Fluid-Gesteins-Prozess ist die Greisenbildung, bei der Biotit und Feldspat durch Quarz, Hellglimmer ± Topas ± Fluorit ersetzt werden. Diese Umwandlung verbindet die Fluid-Gesteins-Wechselwirkung mit der Erzbildung, insbesondere bei der Anreicherung von W, Sn und Li. Dennoch sind die Faktoren, die die Variation der Greisenbildung und die Entwicklung der Fluide steuern, noch nicht vollständig verstanden. In dieser Dissertation kombinieren wir die Analyse von natürlichen Proben mit einem reaktiven Transportmodell, um den Greisenisierungsprozess besser zu verstehen. Die Ergebnisse zeigen, dass die anfängliche Fluidzusammensetzung, einschließlich der F-Konzentration und des pH-Wertes, die Variation der Greisenbildung beeinflusst. Darüber hinaus ist das Sieden ein möglicher Mechanismus zur Einführung von F-reichen Fluiden. Der Fluorgehalt in Topas dient als Indikator für die Veränderung der F-Konzentration im Fluid. Diese Dissertation stellt einen neuen Aspekt der Rolle von Fluor in der Greisenbildung vor– von natürlichen Beobachtungen bis hin zu numerischen Modellen – und trägt so zu einem besseren Verständnis der greisenbedingten Erzbildung und F-verwandten Prozesse bei.

Im ersten wissenschaftlichen Abschnitt wird der Quarz-Topas-Greisen von Zinnwald/Cínovec untersucht, der ein typisches Beispiel für die Interaktion von Gestein mit F-reichen Fluiden darstellt. Ein 12 cm breiter Abschnitt aus diesem Vorkommen zeigt eine Abfolge von Quarz-Topas-Greisen und schwach verändertem Rhyolith. Massenbilanzberechnungen deuten darauf hin, dass während der Greisenbildung ein Nettozuwachs an Fluor, Silicium und anderen Elementen stattfand. Einschlüsse von Fluiden lassen vermuten, dass es während oder vor der Greisenbildung zu einem Siedeprozess kam. Um diese Beobachtungen zu erklären, schlagen wir einen zweistufigen Greisenisierungsprozess vor: Zunächst führt das Sieden des Fluids zur Phasentrennung von HF-reichem Dampf und einer salzhaltigen Lösung. Der Dampf reagiert mit Feldspat und Biotit, wodurch Quarz und Topas entstehen, während der Ersetzung der Ausgangsminerale eine vorübergehende Porosität schafft, die anschließend durch die salzhaltige Lösung gefüllt und durch die Ausfällung von Quarz und Fluorit infolge der Übersättigung geschlossen wird. Diese Studie hebt die Bedeutung des Siedens als Prozess hervor, der F-reiche Fluide einführt und zur Bildung von Quarz-Topas-reichen Greisen beiträgt.

Der erste wissenschaftliche Abschnitt präsentiert Arbeiten zum Quarz-Topas-Greisen von Zinnwald/Cínovec, ein typisches Beispiel für Fluid-Gesteins-Interaktionen mit F-reichen Fluiden. Gleichzeitig ist die Entwicklung der Fluidzusammensetzung entscheidend für die Mobilität der

relevanten Metalle, wie z. B. W und Sn. In diesem Zusammenhang kann Topas, eine wichtige F-haltige Phase im Quarz-Topas-Greisen, zur Untersuchung der Fluidentwicklung, insbesondere der F-Konzentration, verwendet werden. Im zweiten wissenschaftlichen Abschnitt führten wir Raman-Spektroskopie-Messungen an Topas-Kristallen von verschiedenen Standorten durch. Die Ergebnisse zeigen, dass die Verschiebung der Raman-Banden bei etwa 155 und 562 cm^{-1} in einer linearen Korrelation ($y = 0{,}329x - 113{,}6$) mit der F-Konzentration steht, wobei y die F-Konzentration und x die Verschiebung der Raman-Banden ist. Mithilfe dieser Gleichung konnten wir zwei Topas-Typen im Greisenprofil von Zinnwald/Cínovec identifizieren. Der systematische Unterschied von 0,4 Gew.-% F zwischen diesen beiden Typen zeigt die Veränderung der F-Konzentration im Fluid, das mit dem Greisen im Gleichgewicht steht. Diese Methode bietet eine neue Möglichkeit, den Fluorgehalt in Topas zu bestimmen und die zeitliche (und/oder räumliche) Entwicklung des Fluorgehalts im Fluid während der Greisenbildung zu verfolgen.

Die Fallstudie zum Quarz-Topas-Greisen von Zinnwald/Cínovec liefert wertvolle Einblicke in die Greisenbildung. Jedoch sind die steuernden Faktoren hinter der Variation von Quarz-Topas- und Quarz-Glimmer-Greisen unklar. Basierend auf der Untersuchung von natürlichen Proben führt der dritte Abschnitt dieser Dissertation ein reaktives Transportmodell ein, um die Parameter zu bestimmen, die die Entwicklung verschiedener Greisen-Mineralvergesellschaftungen bestimmen. Eine eindringende Flüssigkeit mit einem niedrigeren pH-Wert und einer geringeren F-Konzentration führt zur Bildung von Greisen, die durch eine Abfolge von Quarz-Topas und Quarz-Glimmer gekennzeichnet sind. Im Gegensatz dazu führt saure, mit Fluor angereicherte Flüssigkeit (>0,015 mol/kg) zur Bildung von glimmerfreiem Greisen. Außerdem zeigt das numerische Modell, dass die Bildung von Quarz-Topas-Greisen zu einer höhere Porosität (14 %) führt, als bei der Bildung von Quarz-Glimmer-Greisen (8 %), was darauf hinweist, dass größere Flüssigkeitsmengen durch Quarz-Topas-Greisen fließen können. Diese Ergebnisse verbessern unser Verständnis der beobachteten Greisenvariationen und damit zusammenhängenden Fluidentwicklung und Fluidentwicklung, die entscheidend für die der greisenbezogenen Erzbildung sind.

Zusammenfassend betont diese umfassende Studie die Bedeutung von Quarz-Topas-Greisen in Greisensystemen, insbesondere in einem F-reichen Umfeld, das Potenzial für die Anreicherung seltener Metalle bietet. Durch die Untersuchung der Prozesse auf Mineral- und Gesteinsskala zeigt diese Arbeit, dass Fluor eine zentrale Rolle in Greisensystemen spielt. Die neuartige Methode zur Bestimmung der F-Konzentration in Topas mittels Raman-Spektroskopie ermöglicht präzise Messungen. Noch wichtiger ist, dass das reaktive Transportmodell detaillierte Einblicke zur Fluidentwicklung während der Greisenbildung bietet und somit das Verständnis sowohl der Greisenbildung als auch der damit verbundenen Erzvorkommen, wie z. B. von W, Nb und Ta, verbessert. Diese Dissertation umfasst ein breites Spektrum an Greisenprozessen und liefert wertvolle Erkenntnisse zum Greisenisierungsprozess.

Chapter 1. Introduction

1.1. Motivation

Fluid-rock interactions within the Earth's crust are responsible for the formation of a wide range of economically significant metal deposits. The mobility of elements in aqueous solutions is a key topic in earth sciences, yet a quantitative understanding of the associated processes and their underlying mechanisms remains limited. The speciations of metal cations play a critical role in the mobilization and precipitation of ore-forming elements, with speciations largely influenced by ligands such as hydroxyl, chloride, fluoride, carbonate, and sulfate (Migdisov et al., 2016). Typical deposits include polymetallic veins, greisens, and pegmatites. Among the most significant elements mined from these deposits are the Rare Earth Elements (REEs), High Field Strength Elements (HFSEs) and other rare metals, including Zr, Nb, Mo, Hf, Ta, W, and Sn. These metals, often referred to as "high-tech metals," are crucial for modern technologies such as microelectronics, displays, powerful electric motors, and advanced materials research. Many of them, particularly the HFSEs, are classified as hard acids under the Hard-Soft-Acid-Base (HSAB) theory and preferentially form complexes with hard bases (Pearson, 1997; Vigneresse, 2009). Fluoride, the hardest naturally occurring base, plays a pivotal role in the formation of certain pegmatite and greisen-type deposits. However, its behavior is still not fully understood, partly because conducting experiments involving fluoride is particularly challenging.

Fluoride-rich fluids can strongly influence the distribution of ore metals during metamorphism and partial melting (Oreskes and Einaudi, 1990; Pan and Fleet, 1996; Tropper et al., 2013). Recent studies have investigated the effect of fluoride on element mobility of HFSEs and REEs in highly differentiated granites related to rare metal mineralization (e.g. Keppler and Wyllie, 1991; Pan and Fleet, 1996; Rickers et al. 2006; Chen et al., 2014). Fluoride plays an important but very different role for these two element groups. Migdisov and Williams-Jones (2014) demonstrate that due to the low solubility of REEs-fluoride in aqueous and hydrothermal fluid, REEs-fluoride complexes probably don’t perform as major transporting agents. Instead, chloride and sulfate are the main REE transporting ligands (Williams-Jones et al., 2012; Migdisov et al. 2009, 2016), while fluoride acts as a precipitating agent for REEs. For HFSEs on the other hand, fluoride is a much more potent mobilizer than any other common ligands (Migdisov et al., 2011). This means that fluoride can separate REEs and HFSEs very effectively in geological processes. Interestingly, in aqueous fluoride systems “geochemical twins” such as Ho-Y and Zr-Hf get fractionated, while in all other systems these pairs behave almost identical during chemical processes (Loges et al., 2013, 2024). Recent experimental studies reveal that tungsten fluoride is the dominant phase to mobilize tungsten (Wang et al., 2021; Mei et al., 2024). It is therefore important to understand the evolution of fluorine during the fluid-rock interactions (e.g., greisenization,

skarnization, Halter et al., 1995; Aksyuk, 2000; Lu et al., 2005; Štemprok et al., 2005; Soloviev et al., 2020; Qiao et al., 2024). The fluid derived from highly differentiated granites is always enriched in volatiles (e.g., F, Cl, B, etc.), which reacts with the wall rock resulting in special alterations like greisenization related to mineralizations. This process is crucial for greisen-related ore formation (W, Sn, Li, etc.) and links the magmatic stage to the hydrothermal stage.

In this study, I focus on the role of fluorine (F) in the formation of topaz and the process of greisenization. A case study of quartz-topaz greisen offers insights into the mechanisms that produce concentration-rich fluids, which can lead to the formation of topaz-rich greisen. Quantifying the concentration of F in topaz provides a precise tool to understand the formation environment of topaz. The novel reactive transport modeling recreates the typical types of greisen and reveals the compositional evolution of fluids during greisenization. The results demonstrate that both of F concentration and pH value of the initial fluid control the variation of greisen. which contributes to a better understanding of the greisenization process and the associated mineralization.

1.2. Overview of greisen

1.2.1. Greisen variations

The diversity in greisen mineralogy, e.g., quartz-mica greisen or quartz-topaz greisen, reflects differences in formation conditions. Massive quartz-mica greisen formations are commonly associated with W-Sn ore deposits (e.g., Korges et al., 2018; Launay et al., 2019; Monnier et al., 2019). The predominant micas in greisen are zinnwaldite (Li-Fe dioctahedral mica) and muscovite (e.g., Breiter et al., 2019, 2023; Monnier et al., 2019, 2022). For example, in the Zinnwald/Cínovec deposit, zinnwaldite accounts for 40 vol. % of the greisen (Breiter et al., 2019). In Beauvoir, most of the magmatic phases including feldspar and lepidolite have been altered to muscovite and quartz (Monnier et al., 2019). Compared with quartz-mica greisen, quartz-topaz greisen is less common, but it contains large proportions of topaz.

1.2.1.1. Quartz-topaz greisen

Quartz-topaz greisen often occurs in the inner part of greisen complexes and is often separated from the wall rock by quartz-mica greisen (Halter et al., 1998; Shapovalov and Setkova, 2012), but quartz-topaz greisen veins may also occur in distal parts of a greisen complex (Qiao et al., 2024). Yet, in Kougarok, quartz-topaz greisen is in immediate contact with chlorite schist and is not separated by quartz-mica greisen (Soloviev et al., 2020).

Greisenization is typically confined to shallow crustal levels, near the surface or close to the roof of the pluton (Shcherba, 1970; Štemprok, 1987; Štemprok and Dolejš, 2010). Greisen in Bozi Dar was found via drilling at a depth of 489 – 422 m (Štemprok et al., 2005). Further, at this site, the evolution of bulk rock composition suggests that the quartz-topaz greisen zone corresponds to the enrichment of tungsten, bismuth, and molybdenum. In the shallow part of East Kemptville deposit, quartz-topaz greisen occurs at a depth of <100 m, and it overlies quartz-mica greisen (Halter et al., 1995, 1996, 1998); furthermore, at this location the quartz-topaz greisen corresponds to prior precipitation of cassiterite and sulfides.

1.2.1.2. Quartz-mica greisen

In greisen-related ore deposits, quartz-mica greisen regions often host massive W-Sn mineralization (Korges et al., 2018; Monnier et al., 2019; Launay et al., 2021). Further, in the Zinnwald/Cínovec region, massive quartz-mica greisen bodys are found in the zinnwaldite granite (Breiter et al., 2017a, 2017b), and in the Pansaqueira region, quartz-mica greisen extends from the apical part of the Pansaqueira granite into the surrounding schist. In all of these cases, the host rocks are felsic, which matches the definition of greisenization as being characterized by the breakdown of feldspar and biotite (Burt, 1981).

In Zinnwald/Cínovec, quartz-mica greisenization occurred at the subvolcanic level (Breiter et al., 2005). At crustal levels, P-T conditions generally play an important role in most hydrothermal interactions (Mikucki, 1998; Sillitoe, 2010). For example, an investigation of the fluid inclusions in Beauvoir greisen reveals that the greisen fluid originated from a very shallow magmatic source (Monnier et al., 2020). In that the East Kemptville tin deposit, a single greisenization event was able to form both quartz-topaz greisen and quartz-mica greisen at ~450 °C (Halter et al., 1995). These findings collectively indicate that quartz-topaz greisen and quartz-mica greisen generally form under comparable, relatively low P-T conditions.

1.2.2. Greisen minerals

Quartz is a characteristic and omnipresent phase in greisen system, often constituting over 60 vol. % of the rock. During greisenization, quartz commonly replaces feldspar and biotite (Tempo, 1987). Trace elements in quartz are key indicators for deciphering the transition from magmatic to hydrothermal stages (Breiter et al., 2017a). The Al/Ti and Ge/Ti ratios in quartz reflect the degree of melt fractionation, while hydrothermal quartz tends to be depleted in trace elements (Breiter et al., 2017a; Minnier et al., 2018; Peterková and Dolejš, 2019). Furthermore, hydrothermal quartz is often enriched in mineral inclusions, such as mica and xenotime, in contrast to magmatic quartz (Qiao et al., 2024). This enrichment indicates significant mineral precipitation during the greisenization process.

Mica is a typical mineral found in many greisen formations (Breiter et al., 2023; Launay et al., 2019; Monnier et al., 2019; Peterková and Dolejš, 2019). During greisenization, mica and quartz commonly replace feldspar and biotite (Burt, 1981; tempo, 1987). In greisen, mica generally occurs as muscovite or zinnwaldite (Breiter et al., 2019; Monnier et al., 2022). Its composition is highly sensitive to the changes of the formation environment. In the Zinnwald/Cínovec Sn-W-Li deposit, micas (biotite and zinnwaldite) from different depths display distinct concentrations of F and Li, indicating that they formed in environments with varying concentrations or availability of these elements (Breiter et al., 2019). Mica composition also provides insights into the mobilization and precipitation of economically important metals such as W and Sn. In the Beauvoir greisen, fluid-rock interactions dissolved W- and Sn-rich minerals like lepidolite and cassiterite, leading to the remobilization of these elements (Monnier et al., 2022). Newly formed muscovite incorporated Sn from the fluid, and in Panasqueira, the muscovitization of iron-bearing host rock released iron, which promoted the precipitation of wolframite (Lecumberri-Sanchez et al., 2017; Monnier et al., 2022).

Topaz is a significant F-bearing phase in greisen, particularly in quartz-topaz greisen. The formation of topaz indicates a F-rich fluid environment. Topaz exists as a solid solution ($Al_2SiO_4(F,OH)_2$) between the F- and OH-endmembers in greisen. The X_{OH} value (OH/(OH+F)) of topaz typically ranges between 1.4 and 2 (Barton, 1982). The X_{OH} values can be used as a geothermometer for magmatic and hydrothermal processes (Soufi, 2021). Topaz remains stable under various P-T conditions, such as in subduction zones, orogenic belts, and shallow crust (Wunder et al., 1993; Zhang et al., 2002; Qiao et al., 2024), with formation temperatures ranging broadly from 180 to 800 °C (Soufi, 2021). The presence of topaz offers valuable clues about the forming environment. Firstly, topaz is a OH-bearing mineral, which makes it as a potential agent in deep lithospheric water circulation (Wunder et al., 1993). Secondly, F-rich topaz, whether in igneous or metasomatic settings, indicates a F-rich environment (Soufi, 2021). Finally, topaz influences the distribution of certain elements, such as W and Ge. Tungsten, mobilized by fluoride complexes, can precipitate as wolframite when these complexes are disrupted by topaz formation (Wang et al., 2021). Topaz is also an important carrier of Ge, often incorporating significant amounts of this element from the fluid system (Breiter et al., 2013).

In some greisen-related ore deposits, the mineral modes of greisen may vary with the appearance of new phases such as fluorite, tourmaline, and ore minerals (Soloviev et al., 2020). Due to the low solubility in fluids, fluorite is a common phase with varying abundances across different greisen-related ore deposits. For example, in the Kougarok district, marble acts as one of the wall rocks for greisen. Fluids can extract large amounts of calcium from the marble, leading to widespread fluorite distribution (Soloviev et al., 2020). Additionally, plagioclase can provide calcium to fluorite precipitation (Qiao et al., 2024). Tourmaline is also a typical mineral in greisen, sometimes forming quartz-tourmaline zone (Wright and Kwak, 1989; Baksheev et al., 2019; Soloviev et al., 2020). Its complex composition makes

tourmaline sensitive to fluid composition changes. For example, variations in the Fe^{3+}/Fe^{tot} ratio of tourmaline can indicate changes in the fluid's oxidation state (Baksheev et al., 2019). Tourmaline is also a typical B-bearing phase, and its formation generally suggests a B-rich fluid environment. Greisen is often associated with significant precipitation of metal minerals, especially wolframite and cassiterite (Halter et al., 1996; Monnier et al., 2020; Launay et al., 2021), which are the primary economic ore minerals. Additionally, rare metal-bearing minerals such as xenotime, Nb-Ta-rich rutile, and columbite-group minerals are occasionally found in greisen-related deposits (Breiter et al., 2017c). Base metal sulfides, such as pyrite and chalcopyrite, are also common in the late stage of greisen-related deposits (Halter et al., 1995; Breiter et al., 2017b).

1.2.3. Greisen fluid

Among the important components in greisen fluids that may be responsible for differences in greisen mineralogy are chloride, fluoride, and pH value. Greisen fluids are derived from highly differentiated granitic systems; aqueous fluids exsolved from such systems are enriched in volatiles including Cl, F, B, etc. (Webster et al., 2004; Breiter et al., 2019; Launay et al., 2021; Leopardi et al., 2024).

1.2.3.1. Chlorine in greisen fluid

Numerous studies have proposed that Cl^- is an important component in the greisenization process, because chloride complexes are known to mobilize some metals, including W, Sn, REEs, etc. (Heinrich, 1990; Halter et al., 1996; Zajacz et al., 2008; Migdisov et al., 2016; Korges et al., 2018). A daughter mineral study of fluid inclusions found large proportions of halite, sylvite, calcium chloride, and other chloride minerals, suggesting that many cations in greisen fluids are transported as chloride complexes (Witt, 1988; Leopardi et al., 2024). Sulfide or carbonite is normally subordinate or missing in the greisen-related ore deposits (Müller et al., 2018; Monnier et al., 2019; Leopardi et al., 2024). Further, in situ measurements of fluid inclusions from the Zinnwald/Cínovec Sn-W-Li deposit suggest that the greisen fluid salinity could be up to ~ 40 wt. % NaCl equivalent (Korges, et al., 2018), which implies that the dominant anion in the greisen fluid is Cl^-. Given that greisen fluids tend to be acidic (Burt, 1981; Štemprok et al., 1987), this also indicates that greisen fluid is enriched in Cl^-. However, although it is known that the concentration of Cl^- is controlled by the activity of HCl_0 and the fluid pH value (Halter et al., 1998), how the Cl^- concentration in the fluid affects the formation of a greisen itself is not well understood.

1.2.3.2. Fluorine in greisen fluid

As described by Webster et al. (2004), the greisen fluid in the Zinnwald region was found to contain F in amounts equal to or larger than those of Cl. During the development of quartz-topaz greisen, large amounts of F are required to allow topaz to precipitate in large quantities. Further, as highlighted by

Marignac and Cuney (1991), for the formation of a W-Sn ore deposit to be attributed to a Cl-rich fluid, a large volume of igneous intrusion would be required, but this contradicts the small size of the granitic intrusions that are associated with W-Sn ore bodies (Webster et al., 2004). These observations suggest that a Cl-rich fluid might not dominate its formation. In addition, greisen has been found to display significant deviations from chondritic values in Zr/Hf and Ho/Y ratios, which, coupled with the fact that fluorine can form different complexes with Zr, Hf, Y, and Ho, suggests that fluoride is an important complex ligand in greisen fluid and, thus, may lead to the fractionation of these geological twin elements (Loges et al., 2013, 2024).

1.2.3.3. pH value of greisen fluid

The fluid that reacts with wall rock to form greisen is always acidic (Burt, 1981; Štemprok, 1987). In nature, the dominant acid species is HCl (Burt, 1981), the dissociation of which controls the pH value change of greisen fluid. A stability study of greisen assemblages showed that quartz-topaz and quartz-mica are stable at pH values <3 under given condition (400 °C and 0.5 Kbar, Govorov, 1977).

In the process of greisenization, feldspar-biotite is replaced by quartz-mica (or topaz, and fluorite), and this process consumes H^+ (Lecumberri-Sanchez et al., 2017; Launay et al., 2021), thus working to neutralize the fluid. However, other processes might increase the fluid acidity, like boiling and cooling (Burt, 1981). Overall, the pH evolution of the greisen fluid is key to the mineralization process during greisenization. For instance, tin is mobilized by chloride complexes at low pH conditions, but the solubility of tin chloride is low in near-neutral solutions (Witt, 1988); therefore, neutralization of greisen fluid would result in the precipitation of cassiterite (Jackson and Helgeson, 1985, Halter et al., 1998).

Clearly, to understand the fluid evolution during the different processes of greisenization, the roles of Cl, F, and pH value during greisenization need further investigation.

1.3. Case study: Zinnwald/Cínovec Sn-W-Li deposit

In this study, Zinnwald/Cínovec Sn-W-Li deposit was selected as an example to investigate how F influences the formation of greisen. The Zinnwald/Cínovec deposit has been mined for 4000 years (Tolksdorf et al., 2019). Wolframite was the main ore mineral mined in 19th century, and lithium (mainly in zinnwaldite) was mainly mined in the late 19th century (Webster et al., 2004). Estimation of ore tonnage is up to 270 Mt, including Li, Sn and W (Müller et al., 2018).

1.3.1. Geological setting

The Zinnwald/Cínovec Sn-W-Li deposit is located in the eastern part of the Erzgebirge (Saxon Ore Mountains). Tectonically, the Erzgebirge region lies within the convergence zone between Gondwana in the north and the amalgamated continent to the south, characterized by complex metamorphic and magmatic events (Tait et al., 1997; Collett et al., 2020). The region develops numerous faults, most of which follow NW-SE and NE-SW trends (Štovíčková, 1973). Erzgebirge is a significant metallogenic province, particularly for W and Sn (Fig. 1.1). Historically, approximately 300,000 tonnes of Sn, 21,400 tonnes of W, and 7,000 tonnes of Mo were extracted from the region. However, mining activities have already ceased (Štemprok and Seltmann, 1994).

The Erzgebirge is a lithostratigraphic complex shaped by numerous metamorphic and magmatic events. Large-scale antiform structures and foliation are prominent throughout the area, with the Ohře (Eger) Rift marking its southern boundary. The core of the Erzgebirge predominantly consists of high- and medium-grade metamorphic rocks, such as gneisses, while low-grade metamorphic rocks, including mica schists and phyllites (Fig. 1.1), surround the core (Lorenz and Hoth, 1990; Rötzler et al., 1998; Wolff et al., 2015). The region experienced significant late Variscan magmatism, traditionally classified into the older intrusive complex (OIC), represented by biotite monogranites, and the younger intrusive complex (YIC), represented by syenogranites and alkali feldspar granites (Lange et al., 1972; Tischendorf, 1989; Breiter, 2012). The YIC granites are more evolved than the OIC. Studies indicate that the magmatism in Erzgebirge occurred over a relatively short period between 330 and 310 Ma (Romer et al., 2007; Förster and Romer, 2010; Romer et al., 2010). These granites are primarily calc-alkaline and peraluminous, with varying degrees of crystallization leading to the formation of both low-F and high-F granitic suites. The latter one is typically associated with greisen-related tin deposits (Tischendorf and Förster, 1994).

In terms of their distribution at the surface, granites in Erzgebirge are divided into three main plutons: eastern, middle, and western (Štemprok and Blecha, 2015). However, they may be connected at depth (Förster et al., 1999). In the western pluton, the Nejdek-Eibenstock (NEJ-EIB) and Karlovy Vary massifs are the primary granitic intrusions, with the Nejdek-Eibenstock being the largest granite body in the western Erzgebirge (Štemprok et al., 2005). The Gottesberg (GOT) granite hosts the region's largest quartz-mica greisen deposit (Wasternack et al., 1995). At Boží Dar, drilling revealed a hidden greisen deposit at the contact zone between granite and metamorphic rocks, primarily mica schists and phyllites. Unlike the Gottesberg deposit, this deposit is characterized by quartz-topaz and quartz-mica greisenization, with wolframite mineralization mainly associated with quartz-topaz greisen (Štemprok et al., 2005). In the middle pluton, most of the granites are hidden, with only small outcrops visible (Hoth et al., 1991). Tungsten and/or tin deposits in this area are predominantly related to these hidden

granites, with mineralization occurring in veins, greisen stringers, and stockworks (Hoth et al., 1991; Förster and Rhede, 2006).

In the eastern Erzgebirge, the dominant geological unit is the 40 × 20 km Teplice caldera (Fig. 1.1 c). Most late Variscan magmas were emplaced within this caldera, and significant tin-tungsten mineralization events were also linked to it (Breiter, 1997). The A-type granites within the caldera are largely covered by Teplice rhyolite, with only small outcrops exposed (Breiter et al., 2017b). These outcrops are closely associated with W-Sn deposits. The Altenberg and Zinnwald/Cínovec Li-mica granites host most of the area's ore-forming activities, some of which extend into the surrounding Teplice rhyolite (Breiter et al., 2017b; Qiao et al., 2024). The Zinnwald/Cínovec Sn-W-Li deposit is a representative example of a greisen and quartz vein deposit linked to late Variscan magmatism.

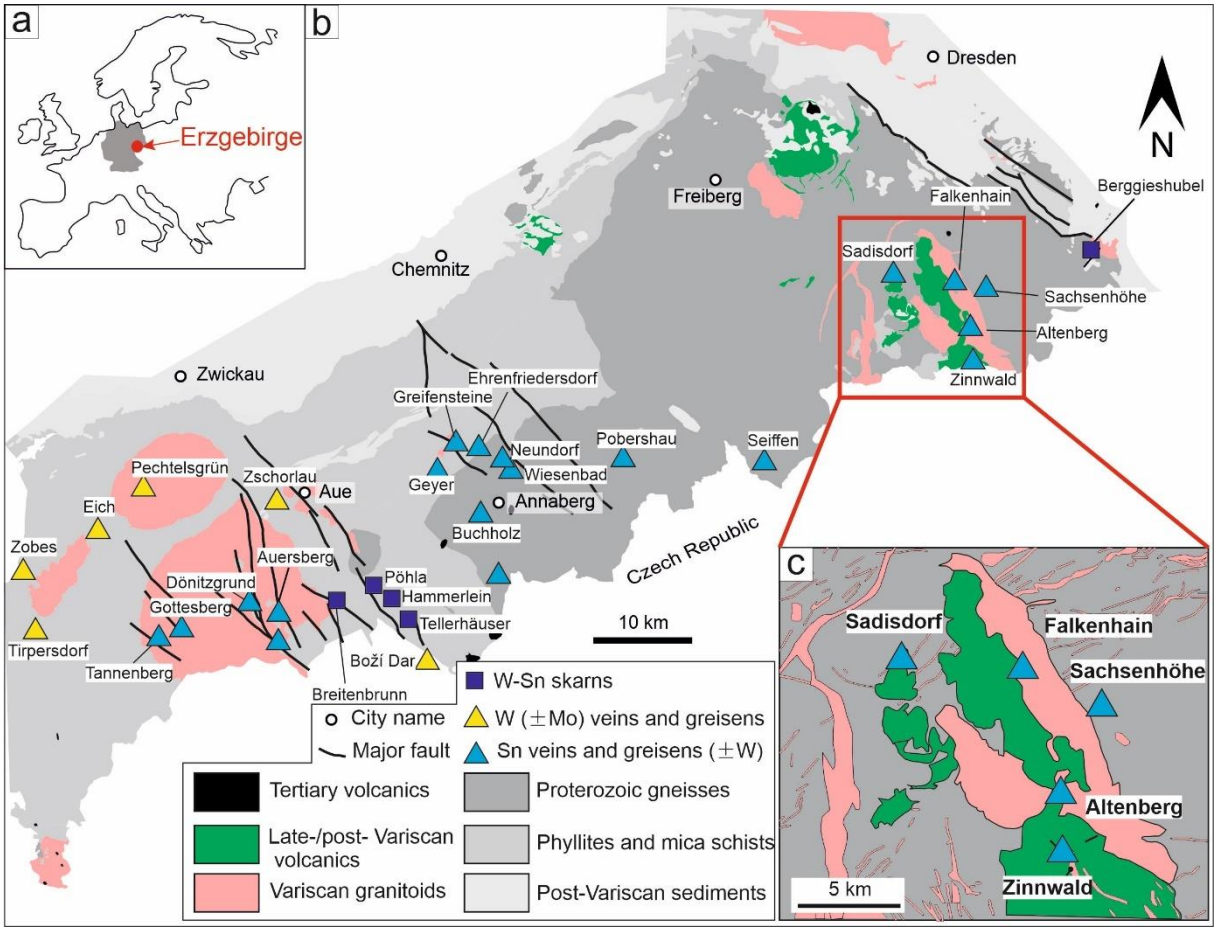

Fig. 1.1 Simplified geological map of the Erzgebirge area. (a) Location of Erzgebirge region; (b) Geological map of the late-Variscan granites and Sn-W deposits in Erzgebirge area (Modified after Sächsisches Landesamt für Umwelt, 1994). (c) Geological map of Teplice caldera (Mlčoch, 1994; Hoth et al., 1995). The locations of ore deposits are according to Štemprok and Blecha, 2015.

1.3.2. Zinnwald/Cínovec Sn-W-Li deposit

The Zinnwald/Cínovec greisen-related Sn-W-Li deposit, located at the border between Germany and the Czech Republic, is one of the largest Sn-W-Li deposits in Europe. Exploration of tin in this district began in the late 13th century (Webster, 2004). The estimated resources of tungsten and tin in this deposit are approximately 270 Mt. In recent years, lithium has gained increasing attention, with Li concentrations in the deposit reaching up to 4000 µg/g (Breiter et al., 2017b; Müller et al., 2018). The Zinnwald/Cínovec deposit is hosted by zinnwaldite granite (Štemprok and Šulcek, 1969; Breiter et al., 2017a, 2017b). Drilling in the district has revealed a biotite granite at depth, which gradually changes to zinnwaldite granite through a narrow 10-meter transition zone (Johan et al., 2012). The biotite granite is relatively homogeneous, within only a few thin microgranite layers, and contains low concentrations of F (0.4-0.5 wt. %) and Li (100-300 µg/g). In contrast, the zinnwaldite granite shows significant variability in texture, mineralogy, and geochemistry. It is a highly differentiated A-type granite, characterized by elevated silicon content, high loss on ignition (LOI) values, and enrichment in F (0.6-1.1 wt.%), Li (up to 4000 µg/g in the greisen), as well as W, Sn, Nb, Ta, and other trace elements (Breiter et al., 2012, 2017a, 2017b, 2017c; Müller et al., 2018).

In the apical zone, fine-grained granite has undergone intense greisenization, leading to mineralization of Sn, W, and Li. Beneath this greisenized granite, a mica-free granite layer was found at depths between 280 and 370 meters. Previous studies suggest that fluid exsolution from this layer led to depletion of F and rare metals (e.g., Li, W, Sn, Nb, Ta). These fluids, enriched in F and rare metals, were subsequently responsible for the greisenization process (Candela, 1997; Breiter et al., 2017b). Mineralization activities mainly occurred in the uppermost part of the cupola, which consists of three main types of ore bodies (Bolduan et al., 1967; Čada and Novák, 1974):

1. **Massive greisen bodies**: These thick, flat zones, tens to hundreds of meters in thickness, are located in the southern part (Czech Republic) and are typically parallel to the contact zone between rhyolite and zinnwaldite granite. The primary minerals in this zone are quartz, zinnwaldite, and topaz. Cassiterite, which hosts the majority of the Sn content, is disseminated throughout the body, while wolframite is rare (Müller et al., 2018).
2. **Flat veins (flöze)**: These veins are characterized by coarse-grained quartz-zinnwaldite bands, often displaying an onion-like structure in the central area. The veins are surrounded by 20-200 cm greisen selvages of quartz-zinnwaldite (± topaz). Wolframite is the dominant ore mineral, with cassiterite playing a subordinate role.
3. **Steep veins (Morgengänge)**: Similar to flat veins, these veins mainly occur on the Saxonian side of the deposit. The main minerals are quartz and zinnwaldite, and the mineralization resembles that of the flat veins.

1.4. Scientific approach

In this project, alongside optical microscopy, electron microprobe analysis (EMPA), cathodoluminescence (CL), back scattered electron (BSE) imaging, and scanning electron mapping (SEM), I also employed Raman spectroscopy to propose a linear correlation between the Raman band shift and F concentration in topaz. This correlation provides a precise constraint on variations in the F concentration of topaz and allows further evaluation of the regarding changes in the F content of the equilibrated fluid. Furthermore, a reactive transport model was utilized to simulate the formation of greisen, reproducing sequences of different greisen types and illustrating changes in fluid composition. Overall, these approaches contribute to a deep understanding of the process of greisenization and the formation of greisen-related ore deposits.

1.4.1. Fluorine concentration determination by Raman spectroscopy

Electron microprobe analysis (EMPA) is routinely used to measure F concentration in topaz (Stormer et al., 1993; Pinheiro et al., 2002; Gatta et al., 2006; Breiter et al., 2013). However, various factors such as inadequate standards, peak shifts, and matrix effects can compromise the accuracy of the results (Solberg, 1982). Secondary ion mass spectrometry (SIMS) can provide accurate fluorine concentration measurements for various minerals (e.g., apatite, mica, Ottolini et al., 2010; Li et al., 2020a, 2020b), but the matrix effect across different minerals significantly impacts SIMS results (Ottolini et al., 2000a). A combination of structure refinement, EMPA, and SIMS can yield accurate F concentrations in topaz (Ottolini et al., 2000a, 2000b, 2006), but this approach requires appropriate calibration standards. In addition to direct measurement techniques, alternative methods exist for determining F concentration in topaz. Ribbe and Rosenberg (1971) proposed a method based on unit cell volume or the b cell parameter from X-ray powder diffraction (XRD) measurements, establishing a regression equation to correlate the unit cell volume or b cell edge with F concentration determined by EMPA. This method circumvents some of the drawbacks of EMPA, but XRD measurements require specific sample sizes, making in situ measurement in earth sciences challenging.

Raman spectroscopy offers a powerful, non-destructive method for mineral identification based on characteristic spectrum (Haskin et al., 1997; Das and Hendry, 2011). It doesn't require complex sample preparation, standards, or large sample sizes, allowing for high-resolution in situ measurements (Di Genova et al., 2015; González-García et al., 2020). In recent years, quantitative studies using Raman spectroscopy have made significant advances across multiple disciplines (Pelletier, 2003; Strachan et al., 2007; Zhong et al., 2021; Loges et al., 2022). However, studies on the correlation of mineral composition and corresponding Raman spectra remain limited (Pinheiro et al., 2002; Muller et al., 2006; Zinin et al., 2011; Di Genova et al., 2015; González-García et al., 2020). In this work, a new equation

was proposed to determine F concentration in topaz using Raman spectroscopy, offering a practical approach for F concentration measurements.

1.4.2. Reactive transport modeling of greisen formation

Petrological, mineralogical, and chemical investigations of natural samples offer insights into processes occurring deeply within and beneath the Earth's surface. However, for the details of these processes, these studies normally can't give good constraints, such as magma ascent rates in volcanic structures (Li et al., 2020a) or dynamic porosity changes (Balashov and Yardley, 1998). In contrast, reactive transport modeling allows for the simulation of natural processes based on observed data such as elemental diffusion, advection, chemical reactions, and even their durations (John et al., 2012; Weis et al., 2012; Dolejš, 2015; Steefel, 2019; Beinlich et al., 2020; Vehling et al., 2021; Li et al., 2022). This type of modeling can reveal how variables of interest evolve, such as exhumation velocities of high-pressure units (Schwarzenbach et al., 2021) or the dehydration behavior of serpentinite at various scales (Huber et al., 2024). For fluorine-specific reactions like greisenization, constraining the evolution of F content is critical to understanding related processes. Fluorine is a unique ion with a high ionization potential (17.42 eV, Quarles et al., 2014) higher than the argon, making it difficult to ionize or excite with lasers. Reactive transport modeling offers an advantage in tracking F evolution, facilitating our understanding of fluorine behavior in fluid-rock interactions and the mobility of fluoride-metal complexes (Halter et al., 1998).

Natural processes are governed by the laws of mass, momentum, energy, and concentration balances between fluid and solid phases (Vrijmoed and Podladchikov, 2022). In reactive transport modeling, these processes are typically treated as equilibrium systems, with the assumption of local thermodynamic equilibrium applied to non-equilibrium processes (Lebon et al., 2008; Borg et al., 2014; Steefel et al., 2015; Plümper et al., 2017). Equilibrium is calculated through Gibbs energy minimization for mineral, gas, fluid, or melt phases, yielding the variables of interest needed for transport simulations. The details can be referred to Chapter 4.

1.5. Funding of the thesis

This thesis was initially funded by China Scholarship Council (No.: 201908110287). Additional financial and scientific support was provided by the Deutsche Forschungsgemeinschaft (DFG, German Research Foundation, project 387284271-SFB 1349, 'Fluorine Specific Interactions'), which is a collaborative research project included Freie Universität Berlin, the Humboldt University Berlin, the

Technical University Berlin, the Federal Institute for Materials Research and Testing and the Leibniz Research Institute for Molecular Pharmacology on fluorochemical issues. The aim of this project is to understand and control the complex interactions that can emanate from fluorinated structural units in chemical systems.

1.6. Aims

This thesis provides a systematic study, which offers new insights to the impact of fluorine on the formation of greisen and the related ore formation. The aim is to give a further understanding of the process of greisenization, especially the process related to fluorine. The thesis attempts to accomplishes the following goals:

1. The case study of Zinnwald/Cínovec quartz-topaz greisen to the reveal the mechanism introducing F-rich fluid. This work includes the bulk-rock investigation on the quartz-topaz greisen, mineralogical study to understand the process of greisenization, mass balance calculation to understand the mass change during the process of greisenization, fluid inclusion study.
2. Develop the method of F determination in topaz by Raman spectroscopy. Firstly, investigate the topaz collected from different localities and clarify the correlation of F concentration in topaz and Raman bands. And then test it by the topaz from Zinnwald/Cínovec greisen.
3. Develop the reactive transport model to simulate the formation of different types of greisen and investigate the fluid evolution during the process of greisenization. The aim of this work is to understand which factor controls the variation of greisen (including quartz-topaz greisen and quartz-mica greisen).

The main aim of this work is to expand the understanding of greisenization, especially F-related process, and further provide insights in the potential ore mineralization.

1.7. Structure of the thesis

The thesis consists of five chapters. Three of them were written as scientific articles. Chapter 2 has been published in the peer-reviewed journal of '***Economic Geology***'. Chapter 3 is still in preparation for the further publication. Chapter 4 has been submitted to the journal of **'*Geochimica et Cosmochimica Acta'***, and now is under review. In addition, Chapter 1 introduces the background of this dissertation, which includes the motivation, the overview of greisen, the introduction of Zinnwald/Cínovec Sn-W-Li deposit, scientific approaches, funding and aims in this study. It outlines the basic structure of my doctoral work. Chapter 5 gives the conclusions and outlook. For each scientific article chapter supplementary material

is given in the supplementary material. Especially, I add the raw data of mineral composition by electron microprobe analysis and Matlab code into the supplementary material.

Chapter 2: Formation of Topaz-Greisen by a Boiling Fluid: A Case Study from the Sn-W-Li Deposit, Zinnwald/Cínovec

Shilei Qiao, Timm John, and Anselm Loges

Published in the journal of '***Economic Geology***' (https://doi.org/10.5382/econgeo.5074)

Chapter 2 presents the petrological, mineralogical and geochemical study on the Zinnwald/Cínovec quartz-topaz greisen. The mineralogical and textural evidences present the details of the replacement of feldspar and biotite by quartz and topaz. Mass balance calculation shows the gain of F, Si and light rare earth elements (LREEs), along with the loss of alkali elements and heavy rare earth elements (HREEs). A two-stage boiling process is proposed to explain these observations. This study highlights that an additional process to induce the F-rich fluid is crucial to the formation of quartz-topaz greisen.

In this work, Anselm Loges and Timm John organized the field work and provided the idea of how to process the samples and data. Timm John, Anselm Loges and I collected the samples from the mine. I was responsible for sample preparation and carried out electron microprobe analyses (including spot analysis and mapping) on albite, K-feldspar, mica, topaz, and monazite. I also captured optical microphotographs and performed cathodoluminescence (CL) and backscattered electron (BSE) imaging. Moritz Liesegang assisted the microprobe measurement. Johannes C. Vrijmoed conducted the SEM mapping of the greisen transect and provided the code to process the SEM data. The major and trace element concentration of the bulk rock were analyzed by *Actlabs*, Canada. Timm John designed the structure of the manuscript, while I processed the data and wrote the initial manuscript, along with preparing the figures. Timm John and Anselm Loges reviewed the manuscript. All authors analyzed and interpreted the data and the key points, which contributed to the final publication.

Chapter 3: **Determination of Fluorine Concentration in Topaz Using Raman Spectroscopy**

Anselm Loges, Shilei Qiao, Xin Zhong and Timm John

In preparation

Chapter 3 presents a method study on topaz, which combined measurements by X-Ray diffraction (XRD) and Raman spectroscopy on the collected topaz grains. A linear correlation is proposed between the distance shift of specific band positions and F concentration in topaz, which was them employed to determine the F concentration in Zinnwald/Cínovec topaz through in situ measurements of Raman spectroscopy. Along with cathodoluminescence (CL) zonation in topaz, two types of topaz were

successfully recognized across the topaz-rich greisen transect. The later-generation topaz exhibits F concentrations that are 0.4 wt. % higher than those of the earlier generation. This approach reveals that topaz is a key mineral sensitive to changes in the F concentration of equilibrated fluids.

Anselm Loges proposed the idea and conducted the measurements using XRD and Raman microscopy on the collected topaz, as well as programmed the code to process the Raman data. Timm John provided guidance throughout the measurements. I performed the Rotation measurements on the standard topazes, conducted cathodoluminescence (CL) imaging, and carried out in situ spot and mapping analysis on the Zinnwald/Cínovec topaz. Anselm Loges and me processed the data, and I also prepared figures related to Zinnwald/Cínovec topaz. Xin Zhong provided help for the Raman measurements. Anselm Loges wrote the initial manuscript. All authors discussed the key points included in this paper.

Chapter 4: Controls of F content and pH on the formation of greisen quantified by reactive transport modeling

Shilei Qiao, Anselm Loges, Johannes C. Vrijmoed, Timm John

Submitted to the journal of '***Geochimica et Cosmochimica Acta***' (under review)

Chapter 4 offers a novel reactive transport model to simulate the formation of greisen, with results that encompass the most common greisen types, such as quartz-mica and quartz-topaz greisen. Simulations conducted with varying F concentrations and pH values of the initial fluid reproduced greisen sequences representative of the most common greisen types observed in nature. Furthermore, the model provides a method for evaluating key parameters, such as F concentration and pH, during the greisenization process, which influence the variation in greisen composition. The study also highlights the importance of fluoride and chloride metal complexes in understanding the formation of greisen-related ore deposits.

Johannes C. Vrijmoed programmed the code and compiled the thermodynamic data of phases required for the calculation. I tested the input parameters for the program, including the initial system composition, fluid and solid phases, and prepared the lookup tables and conducted the final calculations. Timm John and Anselm Loges provided valuable guidance in structuring the manuscript. Finally, I prepared all the figures and wrote the initial manuscript. All the authors discussed and agreed the key points included in the manuscript.

References

Aksyuk, A.M., 2000. Estimation of fluorine concentrations in fluids of mineralized skarn systems. Economic Geology, 95, 1339-1347.

Baksheev, I.A., Vigasina, M.F., Yapaskurt, V.O., Bryzgalov, I.A., Gorelikova, N.V., 2019. Tourmaline from the Solnechnoe tin deposit, Khabarovsk Krai, Russia. Mineralogical Magazine, 84, 245-265.

Balashov, V.N., Yardley, B.W.D., 1998. Modeling metamorphic fluid flow with reaction-compaction-permeability feedbacks. American Journal of Science, 298, 441-470.

Barton, M.D., 1982. The thermodynamic properties of topaz solid solutions and some petrologic applications. American Mineralogist, 67, 956-974.

Beinlich, A., John, T., Vrijmoed, J.C., Tominaga, M., Magna, T., Podladchikov, Y.Y., 2020. Instantaneous rock transformations in the deep crust driven by reactive fluid flow. Nature Geoscience, 13, 307-311.

Borg, S., Liu, W., Pearce, M., Cleverley, J., MacRae, C., 2014. Complex mineral zoning patterns caused by ultra-local equilibrium at reaction interfaces. Geology, 42, 415-418.

Breiter, K., 1997. Teplice rhyolite (Krušné horyMts., Czech Republic) chemical evidence of a multiply exhausted stratified magma chamber. Bull. Czech Geological Survey, 72, 205–213.

Breiter, K., 2012. Nearly contemporaneous evolution of the A- and S-type fractionated granites in the Krušné hory/Erzgebirge Mts., Central Europe. Lithos, 151, 105-121.

Breiter, K., Ďurišová, J., Dosbaba, M., 2017a. Quartz chemistry – A step to understanding magmatic-hydrothermal processes in ore-bearing granites: Cínovec/Zinnwald Sn-W-Li deposit, Central Europe. Ore Geology Reviews, 90, 25-35.

Breiter, K., Ďurišová, J., Hrstka, T., Korbelová, Z., Hložková Vaňková, M., Vašinová Galiová, M., Kanický, V., Rambousek, P., Knésl, I., Dobeš, P., Dosbaba, M., 2017b. Assessment of magmatic vs. metasomatic processes in rare-metal granites: A case study of the Cínovec/Zinnwald Sn–W–Li deposit, Central Europe. Lithos, 292-293, 198-217.

Breiter, K., Korbelová, Z., Chládek, Š., Uher, P., Knesl, I., Rambousek, P., Honig, S., Šešulka, V., 2017c. Diversity of Ti–Sn–W–Nb–Ta oxide minerals in the classic granite-related magmatic–hydrothermal Cínovec/Zinnwald Sn–W–Li deposit (Czech Republic). European Journal of Mineralogy, 29, 727-738.

Breiter, K., Förster, H.J., Seltmann, R., 1999. Variscan silicic magmatism and related tin-tungsten mineralization in the Erzgebirge-Slavkovsky les metallogenic province. Mineralium Deposita, 34, 505-521.

Breiter, K., Galiová, M.V., Hložková, M., Korbelová, Z., Kynický, J., Costi, H.T., 2023. Trace element composition of micas from rare-metal granites of different geochemical affiliations. Lithos, 446-447.

Breiter, K., Gardenová, N., Vaculovič, T., Kanický, V., 2013. Topaz as an important host for Ge in granites and greisens. Mineralogical Magazine, 77, 403-417.

Breiter, K., Hložková, M., Korbelová, Z., Galiová, M.V., 2019. Diversity of lithium mica compositions in mineralized granite–greisen system: Cínovec Li-Sn-W deposit, Erzgebirge. Ore Geology Reviews, 106, 12-27.

Breiter, K., Müller, A., Leichmann, J., Gabašová, A., 2005. Textural and chemical evolution of a fractionated granitic system: the Podlesí stock, Czech Republic. Lithos, 80, 323-345.

Breiter, K., Svojtka, M., Ackerman, L., Švecová, K., 2012. Trace element composition of quartz from the Variscan Altenberg–Teplice caldera (Krušné hory/Erzgebirge Mts, Czech Republic/Germany): Insights into the volcano-plutonic complex evolution. Chemical Geology, 326-327, 36-50.

Burt, D.M., 1981. Acidity-salinity diagrams-application to greisen and porphyry deposits. Economic Geology, 76, 832-843.

Bolduan, H., Lächelt, A., and Malásek, F., 1967, Zur geologie und mineralisation der Lagerstätte Zinnwald (Cínovec): Freiberger Forschungshefte C, 218, 35-52.

Candela, P.A., 1997. A review of shallow, ore-related granites: textures, volatiles, and ore metals. Journal of Petrology, 38, 1619-16936.

Čada, M., and Novák, J.K., 1974, Spatial distribution of greisen types at the Cínovec-South tin deposit, in Štemprok, M., ed., Metallization associated with acid magmatism: Prague, Czech Geological Survey, 1, 383–388.

Chen, B., Ma, X., Wang, Z., 2014. Origin of the fluorine-rich highly differentiated granites from the Qianlishan composite plutons (South China) and implications for polymetallic mineralization. Journal of Asian Earth Sciences, 93, 301-314.

Collett, S., Schulmann, K., Štípská, P., Míková, J., 2020. Chronological and geochemical constraints on the pre-variscan tectonic history of the Erzgebirge, Saxothuringian Zone. Gondwana Research, 79, 27-48.

Cuney, M., Marignac, C., Weisbrod, A., 1992. The beauvoir topaz-lepidolite albite granite (Massif Central, France): The disseminated magmatic Sn-Li-Ta-Nb-Be mineralization. Economic Geology, 87, 1766-1794.

Di Genova, D., Morgavi, D., Hess, K.U., Neuville, D.R., Borovkov, N., Perugini, D., Dingwell, D.B., 2015. Approximate chemical analysis of volcanic glasses using Raman spectroscopy. J Raman Spectrosc, 46, 1235-1244.

Dolejš, D., 2015. Quantitative characterization of hydrothermal systems and reconstruction of fluid fluxes: the significance of advection, disequilibrium, and dispersion. SGA Proceedings 13th SGA biennial meeting, Nancy, France.

Förster, H.J., Rhede, D., 2006. The Be–Ta-rich granite of Seiffen (eastern Erzgebirge, Germany): accessory-mineral chemistry, composition, and age of a late-Variscan Li–F granite of A-type affinity. Journal of Mineralogy and Geochemistry, 182, 307-321.

Förster, H.-J., Romer, R.L., 2010. Carboniferous magmatism. In: Linnemann, U., Romer, R.L. (Eds.), Pre-Mesozoic Geology of Saxo-Thuringia — From the Cadomian Active Margin to the Variscan Orogen. Schweizerbart, sche Verlagsbuchhandlung, Stuttgart, pp. 287-308.

Förster, H.J., Tischendorf, R.B., Trumbull, R.B., Gottesmann, B., 1999. Late-Collisional granite in the Variscan Erzgebirge, Germany. Journal of Petrology, 40, 1613-1645.

Gatta, G.D., Nestola, F., Bromiley, G.D., Loose, A., 2006. New insight into crystal chemistry of topaz: A multi-methodological study. American Mineralogist, 91, 1839-1846.

González-García, D., Giordano, D., Russell, J.K., Dingwell, D.B., 2020. A Raman spectroscopic tool to estimate chemical composition of natural volcanic glasses. Chemical Geology, 556, 119819.

Govorov, I.N., 1977. Thermodynamics of ionic mineral equilibria and mineralogy of hydrothermal deposits. -Izd. Nauka, Moskva.

Halter, W.E., Williams-Jones, A. E., Kontak, D.J., 1995. Origin and evolution of the greisenizing fluid at the East Kemptville tin deposit, Nova Scotia, Canada. Economic Geology, 93, 1026-1051.

Halter, W.E., Williams-Jones, A.E., Kontak, D.J., 1996. The role of greisenization in cassiterite precipitation at the East Kemptville tin deposit, Nova Scotia. Economic Geology, 91, 368-385.

Halter, W.E., Williams-Jones, A. E., Kontak, D. J., 1998. Modeling fluid-rock interaction during greisenization at the East Kemptville tin deposit: implications for mineralization. Chemical Geology, 150, 1-17.

Haskin, L.A., Wang, A., Rockow, K.M., Jolliff, B.L., Korotev, R.L., Viskupic, K.M., 1997. Raman spectroscopy for mineral identification and quantification for in situ planetary surface analysis: A point count method. Journal of Geophysical Research: Planets, 102, 19293-19306.

Heinrich, C.A., 1990. The chemistry of hydrothermal Tin(-tungsten) ore deposition. Economic Geology, 85, 457-481.

Hoth, K., Berger, H.J., Breiter, K., Mlčoch, B., and Schovánek, P., 1995. Geological map of the Erzgebirge/Vogtland 1:100000: Sächsisches Landesamt für Umwelt und Geologie, Freiberg (in German).

Hoth, K., Ossenkopf, W., Hösel, G., Zernke, B., Eisenschmidt, K., Kühne, R., 1991. Die Granite im Westteil desMittelerzgebirgischen Teilplutons und ihr Rahmen. Geoprofil 3, 3-13.

Huber, K., John, T., Vrijmoed, J.C., Pleuger, J., Zhong, X., 2024. Pulsed fluid release from subducting slabs caused by a scale-invariant dehydration process. Earth and Planetary Science Letters, 644, 118924.

Jackson, K.J., Helgeson, H.C., 1985. Chemical and thermodynamic constraints on the hydrothermal transport and deposition of tin: II. Interpretation of phase relations in the southeast Asian tin belt. Economic Geology, 80, 1365-1378.

Johan, Z., Strnad, L., Johan, V., 2012. Evolution of the Cinovec (zinnwald) Granite Cupola, Czech Republic: Composition of Feldspars and Micas, a Clue to the Origin of W, Sn Mineralization. The Canadian Mineralogist, 50, 1131-1148.

John, T., Scherer, E.E., Haase, K., Schenk, V., 2004. Trace element fractionation during fluid-induced eclogitization in a subducting slab: trace element and Lu–Hf–Sm–Nd isotope systematics. Earth and Planetary Science Letters, 227, 441-456.

Keppler, H., Wyllie, P.J., 1991. Partitioning of Cu, Sn, Mo, W, U, and Th between melt and aqueous fluid in the systems haplogranite-H_2O-HCl and haplogranite-H_2O-HF. Contributions to Mineralogy and Petrology, 109, 139-150.

Korges, M., Weis, P., Lüders, V., Laurent, O., 2018. Depressurization and boiling of a single magmatic fluid as a mechanism for tin-tungsten deposit formation. Geology, 46, 75-78.

Lange, H., Tischendorf, G., Pälchen, W., Klemm, I., Ossenkopf, W., 1972. Zur Petrographie und Geochemie der Granite des Erz gebirges. Geologie, 21, 457-492.

Launay, G., Sizaret, S., Guillou-Frottier, L., Fauguerolles, C., Champallier, R., Gloaguen, E., 2019. Dynamic Permeability Related to Greisenization Reactions in Sn-W Ore Deposits: Quantitative Petrophysical and Experimental Evidence. Geofluids, 2019, 1-23.

Launay, G., Sizaret, S., Lach, P., Melleton, J., Gloaguen, E., Poujol, M., 2021. Genetic relationship between greisenization and Sn–W mineralization in vein and greisen deposits: Insights from the Panasqueira deposit (Portugal). BSGF - Earth Sciences Bulletin, 192, 2-29.

Lebon, G., Jou, D., Casas-Vázquez, J., 2008. Understanding non-equilibrium thermodynamics: Foundations, applications, frontiers. Springer.

Lecumberri-Sanchez, P., Vieira, R., Heinrich, C.A., Pinto, F., Wälle, M., 2017. Fluid-rock interaction is decisive for the formation of tungsten deposits. Geology, 45, 579-582.

Leopardi, D., Gutzmer, J., Lehmann, B., Burisch, M., 2024. The Spatial and Temporal Evolution of the Sadisdorf Li-Sn-(W-Cu) Magmatic-Hydrothermal Greisen and Vein System, Eastern Erzgebirge, Germany. Economic Geology, 119, 771-803.

Li, W., Chakraborty, S., Nagashima, K., Costa, F., 2020a. Multicomponent diffusion of F, Cl and OH in apatite with application to magma ascent rates. Earth and Planetary Science Letters, 550, 116545.

Li, W., Costa, F., 2020b. A thermodynamic model for F-Cl-OH partitioning between silicate melts and apatite including non-ideal mixing with application to constraining melt volatile budgets. Geochimica et Cosmochimica Acta, 269, 203-222.

Li, Y., Allen, M.B., Li, X.-H., 2022. Millennial pulses of ore formation and an extra-high Tibetan Plateau. Geology, 50, 665-669.

Loges, A., Manni, M., Louvel, M., Wilke, M., Jahn, S., Welter, E., Borchert, M., Qiao, S., Klemme, S., Keller, B.G., John, T., 2024. Complexation of Zr and Hf in fluoride-rich hydrothermal aqueous fluids and its significance for high field strength element fractionation. Geochimica et Cosmochimica Acta, 366, 167-181.

Loges, A., Migdisov, A.A., Wagner, T., Williams-Jones, A.E., Markl, G., 2013. An experimental study of the aqueous solubility and speciation of Y(III) fluoride at temperatures up to 250 °C. Geochimica et Cosmochimica Acta, 123, 403-415.

Lorenz, W. and Hoth, K., 1990. Lithostratigraphie im Erzgebirge— Konzeption, Entwicklung, Probleme und Perspektiven. Abhandlungen des Sächsischen Museums für Mineralogie und Geologie, 37, 7-35.

Marignac, C., Cuney, M., 1991. What is the meaning of granite specialization for Sn, W deposit genesis? In Pagel, M., Leroy, J.L. (Eds.), Source, transport and deposition of metals. Balkema, Rotterdam, 771-774.

Mei, Y., Liu, W., Guan, Q., Brugger, J., Etschmann, B., Siegel, C., Wykes, J., Ram, R., 2024. Tungsten speciation in hydrothermal fluids. Geochimica et Cosmochimica Acta (in press).

Migdisov, A.A., Williams-Jones, A.E., 2014. Hydrothermal transport and deposition of the rare earth elements by fluorine-bearing aqueous liquids. Mineralium Deposita, 49, 987-997.

Migdisov, A.A., Williams-Jones, A.E., Brugger, J., Caporuscio, F.A., 2016. Hydrothermal transport, deposition, and fractionation of the REE: Experimental data and thermodynamic calculations. Chemical Geology, 439, 13-42.

Migdisov, A.A., Williams-Jones, A.E., van Hinsberg, V., Salvi, S., 2011. An experimental study of the solubility of baddeleyite (ZrO_2) in fluoride-bearing solutions at elevated temperature. Geochimica et Cosmochimica Acta, 75, 7426-7434.

Migdisov, A.A., Williams-Jones, A.E., Wagner, T., 2009. An experimental study of the solubility and speciation of the Rare Earth Elements (III) in fluoride- and chloride-bearing aqueous solutions at temperatures up to 300 °C. Geochimica et Cosmochimica Acta, 73, 7087-7109.

Mikucki, E.J., 1998. Hydrothermal transport and depositional processes in Archean lode-gold systems: A review. Ore Geology Reviews, 13, 307-321.

Mlčoch, B., 1994. The geological structure of the crystalline basement below the North Bohemian brown coal basin. In: Hirschmann, G., Harms, U. (Eds.), KTB Report 93/4: Niedersächsisches Landesamt für Bodenforschung, Hannover, 39-46.

Monnier, L., Lach, P., Salvi, S., Melleton, J., Bailly, L., Béziat, D., Monnier, Y., Gouy, S., 2018. Quartz trace-element composition by LA-ICP-MS as proxy for granite differentiation, hydrothermal episodes, and related mineralization: The Beauvoir Granite (Echassières district), France. Lithos, 320-321, 355-377.

Monnier, L., Salvi, S., Jourdan, V., Sall, S., Bailly, L., Melleton, J., Béziat, D., 2020. Contrasting fluid behavior during two styles of greisen alteration leading to distinct wolframite mineralizations: The Echassières district (Massif Central, France). Ore Geology Reviews, 124, 103648.

Monnier, L., Salvi, S., Melleton, J., Bailly, L., Béziat, D., de Parseval, P., Gouy, S., Lach, P., 2019. Multiple Generations of Wolframite Mineralization in the Echassieres District (Massif Central, France). Minerals, 9, 637-663.

Monnier, L., Salvi, S., Melleton, J., Lach, P., Pochon, A., Bailly, L., Béziat, D., De Parseval, P., 2022. Mica trace-element signatures: Highlighting superimposed W-Sn mineralizations and fluid sources. Chemical Geology, 600, 120866.

Müller, A., Herklotz, G., Giegling, H., 2018. Chemistry of quartz related to the Zinnwald/Cínovec Sn-W-Li greisen-type deposit, Eastern Erzgebirge, Germany. Journal of Geochemical Exploration, 190, 357-373.

Oreskes, N., Einaudi, M.T., 1990. Origin of rare earth element enriched hematite breccias at the Olympic dam Cu–U–Au–Ag deposit, Roxby Downs, South Australia. Economic Geology, 85, 1-28.

Ottolini, L., Cámara, F., Hawthorne, F.C., 2006. Strategies for Quantification of Light Elements in Minerals by SIMS: H, B and F. Microchimica Acta, 155, 229-233.

Ottolini, L., Camara, F., Simona, B., 2000a. An investigation of matrix effects in the analysis of fluorine in humite-group minerals by EMPA, SIMS and SREF. American Mineralogist, 85, 89-102.

Ottolini, L., Oberti, R., 2000b. accurate quantification of H, Li, Be, B, F, Ba, REE, Y, Th, and U in complex matrixes: a combined approach based on SIMS and single-crystal structure refinement. Analytical Chemistry, 72, 3731-3738.

Ottolini, L.P., Schingaro, E., Scordari, F., Mesto, E., Lacalamita, M., 2010. The role of SIMS in the investigation of the complex crystal chemistry of mica minerals. IOP Conference Series: Materials Science and Engineering, 7.

Pan, Y., Fleet, Michael E., 1996. Rare earth element mobility during prograde granulite facies metamorphism: significance of fluorine. Contributions to Mineralogy and Petrology, 123, 251-262.

Pearson, R.G., 1997. Chemical Hardness. John Wiley and Sons, New York. P. 210.

Peterková, T., Dolejš, D., 2019. Magmatic-hydrothermal transition of Mo-W-mineralized granite-pegmatite-greisen system recorded by trace elements in quartz: Krupka district, Eastern Krušné hory/Erzgebirge. Chemical Geology, 523, 179-202.

Pinheiro, M.V.B., Fantini, C., Krambrock, K., Persiano, A.I.C., Dantas, M.S.S., Pimenta, M.A., 2002. OH/F substitution in topaz studied by Raman spectroscopy. Physical Review B, 65, 104301.

Plümper, O., John, T., Podladchikov, Y.Y., Vrijmoed, J.C., Scambelluri, M., 2017. Fluid escape from subduction zones controlled by channel-forming reactive porosity. Nature Geoscience, 10, 150-156.

Qiao, S., John, T., Loges, A., 2024. Formation of Topaz-Greisen by a Boiling Fluid: A Case Study from the Sn-W-Li Deposit, Zinnwald/Cínovec. Economic Geology, 119, 805-828.

Quarles, C.D., Gonzalez, J.J., East, L.J., Yoo, J.H., Morey, M., Russo, R.E., 2014. Fluorine analysis using Laser Induced Breakdown Spectroscopy (LIBS). Journal of Analytical Atomic Spectrometry, 29. 1238.

Ribbe, P.H., Rosenberg, P.E., 1971. Optical and X-ray determinative methods for fluorine in topaz. The American Mineralogist, 56, 1812-1821.

Rickers, K., Thomas, R., Heinrich, W., 2006. The behavior of trace elements during the chemical evolution of the H_2O-, B-, and F-rich granite–pegmatite–hydrothermal system at Ehrenfriedersdorf, Germany: a SXRF study of melt and fluid inclusions. Mineralium Deposita, 41, 229-245.

Romer, R.L., Förster, H.-J., Štemprok, M., 2010. Age constraints for the late-Variscan magmatism in the Altenberg-Teplice Caldera (Eastern Erzgebirge/Krusne hory). Neues Jahrbuch für Mineralogie - Abhandlungen, 187, 289-305.

Romer, R.L., Thomas, R., Stein, H.J., Rhede, D., 2007. Dating multiply overprinted Sn-mineralized granites—examples from the Erzgebirge, Germany. Mineralium Deposita, 42, 337-359.

Rötzler, K., Schumacher, R., Maresch, W.V., Willner, A.P., 1998. Characterization and geodynamic implications of contrasting metamorphic evolution in juxtaposed high-pressure units of the Western Erzgebirge (Saxony, Germany). European Journal of Mineralogy, 10, 261-280.

Sächsisches Landesamt für Umwelt, L. u. G., 1994, Geologische Übersichtskarte 1:400.000: Freiberg.

Schwarzenbach, E.M., Zhong, X., Caddick, M.J., Schmalholz, S.M., Menneken, M., Hecht, L., John, T., 2021. On exhumation velocities of high-pressure units based on insights from chemical zoning in garnet (Tianshan, NW China). Earth and Planetary Science Letters, 570, 117065.

Shapovalov, Y.B., Setkova, T.V., 2012. Experimental study of mineral equilibria in the system $K_2O(Li_2O)$-Al_2O_3-SiO_2-H_2O-HF at 300 to 600 °C and 100 MPa with application to natural greisen systems. American Mineralogist, 97, 1452-1459.

Shcherba, G.N., 1970. Greisens. International Geology Review, 12, 114-150.

Sillitoe, R.H., 2010. Porphyry copper systems. Economic Geology, 105, 3-41.

Solberg, T.N., 1982. Fluorine electron microprobe analysis: variations of X-ray peak shape. In K.F.J. Heinrich, Ed., Microbeam Analysis, 148–150. San Francisco Press, Inc., San Francisco, California.

Soloviev, S.G., Kryazhev, S., Dvurechenskaya, S., 2020. Geology, igneous geochemistry, mineralization, and fluid inclusion characteristics of the Kougarok tin-tantalum-lithium prospect, Seward Peninsula, Alaska, USA. Mineralium Deposita, 55, 79-106.

Soufi, M., 2021. Origin and physical-chemical control of topaz crystallization in felsic igneous rocks: Contrasted effect of temperature on its OH–F substitution. Earth-Science Reviews, 213, 103467.

Steefel, C.I., 2019. Reactive Transport at the Crossroads. Reviews in Mineralogy and Geochemistry, 85, 1-26.

Steefel, C.I., Appelo, C.A.J., Arora, B., Jacques, D., Kalbacher, T., Kolditz, O., Lagneau, V., Lichtner, P.C., Mayer, K.U., Meeussen, J.C.L., Molins, S., Moulton, D., Shao, H., Šimůnek, J., Spycher, N., Yabusaki, S.B., Yeh, G.T., 2015. Reactive transport codes for subsurface environmental simulation. Computational Geosciences, 19, 445-478.

Štemprok, M., Šulcek, Z., 1969. Geochemical profile through an ore-bearing lithium granite. Economic Geology, 64, 392-404.

Štemprok, M., 1987. Greisenization (a review). Geologische Rundschau, 76, 169-175.

Štemprok, M., Blecha, V., 2015. Variscan Sn–W–Mo metallogeny in the gravity picture of the Krušné hory/Erzgebirge granite batholith (Central Europe). Ore Geology Reviews, 69, 285-300.

Štemprok, M., Dolejš, D., 2010. Fluid focusing, mass transfer and origin of fracture-controlled greisens in the Western Krusne hory granite pluton, Central Europe. Zeitschrift fur Geologische Wissenschaften, 38, 207-234.

Štemprok, M., Pivec, E., Langrová, A., 2005. The petrogenesis of a wolframite-bearing greisen in the Vykmanov granite stock, Western Krušné hory pluton (Czech Republic). Bulletin of Geosciences, 80, 163-184.

Štemprok, M., Seltmann, R., 1994. The metallogeny of the Erzgebirge/Krušné hory. In: Seltmann, R., Kämpf, H., Möller, P. (Eds.), Metallogeny of Collisional Orogens. Czech Geological Survey, Prague, pp. 61–69.

Štovíčková, N., 1973. Deep Fault Tectonics and its relation to endogenous geological processes. Academia, Praha (in Czech).

Stormer, J.C., Pierson, M.L., Tacker, R.C., 1993. Variation of F and Cl X-ray internsity due to anisotropic diffusion in apatite during eletron microprobe analysis. American Mineralogist, 78, 641-648.

Tait, J.A., Bachtadse, V., Franke, W., Soffel, H.C., 1997. Geodynamic evolution of the European Variscan fold belt: paleomagnetic and geological constraints. Geologische Rundschau, 86, 585-598.

Tillberg, M., Maskenskaya, O.M., Drake, H., Hogmalm, J.K., Broman, C., Fallick, A.E., Åström, M.E., 2019. Fractionation of Rare Earth Elements in Greisen and Hydrothermal Veins Related to A-Type Magmatism. Geofluids, 2019, 1-20.

Tischendorf, G., 1989. Silicic magmatism and metalogenesis of the Erzgebirge, 107. Veröffentlichungen Zentralinstitut für Physik der Erde, Potsdam.

Tischendorf, G., Forster, H.J., 1994. Hercynian granite magmatism and related metallogenesis in the Erzgebirge: A status report. Monograph Series on Mineral Deposits, 31, 5-23.

Tolksdorf, J.F., Schröder, F., Petr, L., Herbig, C., Kaiser, K., Kočár, P., Fülling, A., Heinrich, S., Hönig, H., Hemker, C., 2019. Evidence for Bronze Age and Medieval tin placer mining in the Erzgebirge mountains, Saxony (Germany). Geoarchaeology, 35, 198-216.

Tropper, P., Manning, C.E., Harlov, D.E., 2013. Experimental determination of $CePO_4$ and YPO_4 solubilities in H_2O-NaF at 800 °C and 1 GPa: implications for rare earth element transport in high-grade metamorphic fluids. Geofluids, 13, 372-380.

Vehling, F., Hasenclever, J., Rüpke, L., 2020. Brine Formation and Mobilization in Submarine Hydrothermal Systems: Insights from a Novel Multiphase Hydrothermal Flow Model in the System H_2O–NaCl. Transport in Porous Media, 136, 65-102.

Vigneresse, J.L., 2009. Evaluation of the chemical reactivity of the fluid phase through hard–soft acid–base concepts in magmatic intrusions with applications to ore generation. Chemical Geology, 263, 69-81.

Vrijmoed, J.C., Podladchikov, Y.Y., 2022. Thermolab: A Thermodynamics Laboratory for Nonlinear Transport Processes in Open Systems. Geochemistry, Geophysics, Geosystems, 23, e2021GC010303.

Wang, X.-S., Williams-Jones, A.E., Hu, R.-Z., Shang, L.-B., Bi, X.-W., 2021. The role of fluorine in granite-related hydrothermal tungsten ore genesis: Results of experiments and modeling. Geochimica et Cosmochimica Acta, 292, 170-187.

Wasternack, J., Tischendorf, G., Hösel, G., Kuschka, E., Breiter, K., Chrt, J., Komínek, J., Štemprok, M., 1995. Mineral resources Erzgebirge -Vogtland/Krušné hory, Map. 2: Metals, Fluorite/Barite-occurrences and environmental impact. Sächsisches Landesamt für Umwelt und Geologie, Bereich Boden und Gelogie, Freiberg, Czech Geological Survey, Prague.

Webster, J., Thomas, R., Förster, H.-J., Seltmann, R., Tappen, C., 2004. Geochemical evolution of halogen-enriched granite magmas and mineralizing fluids of the Zinnwald tin-tungsten mining district, Erzgebirge, Germany. Mineralium Deposita, 39, 452-472.

Weis, P., Driesnerand, T., Heinrich, C.A., 2012. Porphyry-Copper Ore Shells Form at Stable Pressure-Temperature Fronts Within Dynamic Fluid Plumes. Science, 338, 1613-1616.

Williams-Jones, A.E., Migdisov, A.A., Samson, I.M., 2012. Hydrothermal Mobilisation of the Rare Earth Elements - a Tale of "Ceria" and "Yttria". Elements, 8, 355-360.

Witt, W.K., 1988. Evolution of high-temperature hydrothermal fluids associated with greisenization and feldspathic alteration of a tin-mineralized granite, northeast Queensland. Economic Geology, 83, 310-334.

Wolff, R., Dunkl, I., Lange, J.M., Tonk, C., Voigt, T., von Eynatten, H., 2015. Superposition of burial and hydrothermal events: post-Variscan thermal evolution of the Erzgebirge, Germany. Terra Nova, 27, 292-299.

Wright, J.H., Kwak, T.A.P., 1989. Tin-bearing greisens Mount Bischoff, Northwestern Tasmania, Australia. Economic Geology, 84, 551-574.

Wunder, B., Andrut, Michael, Wirth, Richard, 1999. High-pressure synthesis and properties of OH-rich topaz. European Journal of Mineralogy, 11, 803-813.

Zajacz, Z., Halter, W.E., Pettke, T., Guillong, M., 2008. Determination of fluid/melt partition coefficients by LA-ICPMS analysis of co-existing fluid and silicate melt inclusions: Controls on element partitioning. Geochimica et Cosmochimica Acta, 72, 2169-2197.

Zhang, R.Y., Liou, J.G., Shu, J.F., 2002. Hydroxyl-rich topaz in high-pressure and ultrahigh-pressure kyanite quartzites, with retrograde woodhouseite, from the Sulu terrane, eastern China. American Mineralogist, 87, 445-453.

Zhong, X., Petley-Ragan, A.J., Incel, S.H.M., Dabrowski, M., Andersen, N.H., Jamtveit, B., 2021. Lower crustal earthquake associated with highly pressurized frictional melts. Nature Geoscience, 14, 519-525.

Chapter 2. Formation of topaz-greisen by a boiling fluid: a case study from the Sn-W-Li deposit, Zinnwald/Cínovec

Shilei Qiao[1], Timm John[1,*], Anselm Loges[1]

[1]Institut für Geologische Wissenschaften, Freie Universität Berlin, Malteserstr. 74-100, 12249 Berlin, Germany

Key Points

- Fluid boiling can introduce the F-rich fluid, which reacts with the wall rock resulting in the formation of quartz-topaz greisen.
- Reactions of feldspars with HF-rich vapor lead to the formation of topaz and quartz, creating porosity that is later clogged by subsequent mineral precipitation.

Published as:

Qiao, S., John, T., Loges, A., 2024. Formation of Topaz-Greisen by a Boiling Fluid: A Case Study from the Sn-W-Li Deposit, Zinnwald/Cínovec. Economic Geology, 119, 805-828.

https://doi.org/10.5382/econgeo.5074

Chapter 3. Determination of fluorine concentration in topaz using Raman spectroscopy

Anselm Loges, Shilei Qiao, Xin Zhong, Timm John

Institut für Geologische Wissenschaften, Freie Universität Berlin, Malteserstr. 74–100, 12249 Berlin, Germany

Abstract

Fluorine concentration in topaz is difficult to measure precisely and accurately with most methods regularly applied in mineralogy. We present a new protocol for determining F in topaz using Raman band positions. The method is based on the observation that several Raman band positions are near linear functions of F concentration in wt. % over a range covering most naturally occurring topaz. A similar correlation between F concentration and lattice constants has been used for decades to determine F in topaz based on diffraction data. Compared to most diffraction techniques, Raman spectroscopy has the advantage of being non-destructive and spatially resolved. We present four correlation equations that allow to measure F in topaz between 16 and 20.5 wt. % with an accuracy of 0.5 wt. % and a precision of 0.1 wt. %. We recommend the use of the equation F [wt. %] = -113.6 + 0.329 × ($\tilde{\nu}_{562}$ – $\tilde{\nu}_{155}$), where $\tilde{\nu}_{562}$ and $\tilde{\nu}_{155}$ are the fitted positions of two Raman bands in cm^{-1}. Alternatively, the equations F [wt. %] = 181.8 – 1.043 × $\tilde{\nu}_{155}$ or F [wt. %] = 308.0 – 1.074 × $\tilde{\nu}_{268}$ can be used. The method is applied to obtain F distribution with Raman mapping on a natural greisen sample from Zinnwald/Cínovec and its capability to resolve micrometer sized F-heterogeneity is demonstrated.

Keywords: Topaz; Fluorine; Raman spectroscopy; Chemical analysis; Method development

3.1. Introduction

The combination of a wide range of analytical techniques is a central characteristic of modern mineralogy. Despite the large variety of analytical techniques available today, some elements remain difficult to analyze in certain minerals, thus requiring the establishment of new methodological approaches. One important example for such a situation is fluorine in topaz.

Topaz ($Al_2SiO_4F_x(OH)_{2-x}$) contains up to 20.5 wt. % F (x = 1.4 – 2.0 for most natural samples, e.g., Barton, 1982), and is the main fluorine carrying phase in granitoid magmatic rocks and pegmatites as well as hydrothermal veins and greisen alterations around such veins, which are associated with the magmatic-hydrothermal transition of cooling granitoids (e.g., Breiter et al., 2013; Alberico et al., 2003). Near endmember hydroxy topaz is rare in nature and has been reported only from high or ultrahigh

pressure rocks (e.g., Zhang et al., 2002). Due to its simple and well constrained composition with essentially no major element variability apart from the monovalent anion site, the F/OH ratio in topaz potentially provides a relatively straightforward record of certain aspects of the rock formation conditions provided that: (1) we can interpret this ratio in the relevant geodynamic context and (2) we can measure it accurately.

Experimental studies have demonstrated that the F/OH ratio in topaz is controlled by pressure (p), temperature (T), and fluid composition (e.g., Barton, 1982; Wunder et al., 1999). If any two of these three variables are known in a sample, the F/OH ratio in topaz could, therefore, be used to deduce the third. While p and T can be constrained using a plethora of geothermobarometry and phase equilibria techniques, the value of topaz lies in the fact that it is one of relatively few F-rich minerals that can help to determine the fluoride concentration in geofluids, which is important for better understanding fluid-rock interaction but remains difficult to quantify. Other minerals, such as apatite, have been used extensively for this purpose in the past (e.g., Kusebauch et al., 2015a, 2015b), but topaz has not, in part due to analytical difficulties. Analyzing element concentrations in fluid inclusions using laser ablation-inductively coupled plasma-mass spectrometry (LA-ICP-MS) has become a wide-spread technique over the past decade but is not applicable to fluorine because the first ionization energy of fluorine is higher than that of the argon, which is used as the ionizing plasma in commercially available ICP-MS machines (Kramida and Ralchenko, 1999). Crushing samples and leaching the soluble content of the thus opened fluid inclusions in ultrapure water for analysis with ion chromatography (IC) is possible but does not offer the necessary spatial resolution for many research questions, which limits the usefulness of this method for some purposes (Ladenburger et al., 2020). Therefore, topaz is often a more useful recorder of F in geofluids than the fluid inclusions themselves.

Analyzing the F/OH ratio in topaz is, however, not trivial. Secondary ion mass spectrometry (SIMS) is a suitable technique to analyze F as well as H in topaz (e.g., Ottolini et al., 2000), but expensive and not as widely available. Methods based on the X-rays emission, such as electron micro probe analysis (EMPA) or micro X-ray fluorescence (μXRF) are less favorable for lighter elements because of the lower fluorescence yields and higher absorption that leads to the lower emitted X-ray intensity (Raudsepp, 1995; Thompson et al., 2009), thus introducing a larger uncertainty through the necessary absorption correction compared to heavier elements. An even bigger problem is that the absorption of X-rays in anisotropic media, such as minerals, is a three-dimensional function of the orientation of the sample to the detector (Ottolini et al., 2000). This effect is particularly strong for F in topaz because topaz contains densely packed layers of oxygen oriented in [010]. Oxygen, as the next lighter elemental neighbor, absorbs the 1s emission of F particularly strongly because the F 1s emission line lies above but close to the O Kα absorption edge (Thompson et al., 2009); for a more detailed discussion of the structure with figures see Loges et al. (2022). Therefore, Ottolini et al. (2000) concluded in their

comprehensive study on matrix effects on F analyses in F-rich minerals that EMPA is not suitable for analyzing F in topaz unless the same orientation of sample and reference material to the detector can be ensured, which is generally not practical in geological samples.

Due to these limitations, F in topaz is currently mostly analyzed using X-ray diffraction (XRD). This method relies on the observation that the *b*-lattice constant and the unit cell volume of topaz scale almost linearly with the weight percentage of F in the sample over the compositional range relevant for the vast majority of naturally occurring topaz. The equation "F [wt. %] = 892.5 – 99.2 × *b*" (where *b* is the lattice parameter *b* in Å) by Ribbe and Rosenberg (1971) is most frequently applied. The main issue with this method is that it requires powder XRD, which cannot be performed non-destructively or *in-situ* on thin sections. While electron back scatter diffraction (EBSD) can be used to determine lattice constants in thin sections directly (e.g., Saowadee et al., 2017), this technique requires relatively time-consuming sample preparation and is not as widely available in mineralogical institutes as many others. It must be noted that, in theory, the lattice parameters of topaz scale linearly with the molar proportion of F, not the weight proportion. However, because of the small relative mass difference between F and OH of ca. 5 %, the nonlinearity of the correlation by weight is insignificant compared to the involved analytical uncertainties. More importantly, the near linearity only applies to $Al_2SiO_4F_x(OH)_{2-x}$ with x>1 (or F/OH > 1), which covers most but not all naturally occurring topaz. At higher OH concentrations the *Pbnm* symmetry of F-rich topaz breaks down to *Pbn2* due to displacement of neighboring protons by their mutual repulsion (Northrup et al., 1994). This structural change also affects the correlation between lattice parameters and composition, particularly for *b* (see Fig. 3.3 in Alberico et al., 2003). If the entire range of possible topaz compositions is to be covered, the *a* lattice constant should be used instead of *b* (Alberico et al., 2003), despite the higher uncertainty for the F-rich compositional region.

Raman spectroscopy is a commonly applied method with a maximum spatial resolution better than 1 μm that requires minimal sample preparation. Raman as well as infrared (IR) spectroscopy can be used to analyze the OH bands of topaz in order to measure the F/OH ratio (e.g., Pinheiro et al., 2002; Watenphul et al., 2010; Loges et al., 2022). However, Raman spectroscopy suffers from the problem that many natural topaz specimens emit strong fluorescence in a wide region, which may obscure the OH bands (around 3650 cm^{-1}) for all commonly available laser wavelengths. Quantification of OH concentrations using either Raman or IR spectroscopy based on relative or absolute band intensities requires prior determination of the relationship between OH concentration and absorption intensity, which is currently not available. In addition, methods relying on detection of OH rather than the complementary F are inherently less precise near the F endmember composition, which is where most natural topaz lies (e.g., Barton, 1982; Ribbe and Rosenberg, 1971).

Raman spectroscopy can, however, be used to indirectly measure the composition of minerals because several aspects of Raman bands change systematically with composition. While band intensity

and width are also influenced by composition but also by other factors, particularly laser polarization and sample orientation (e.g., Beny and Piriou, 1987), Raman band positions are a direct expression of phonon energy of vibrational modes in a crystal (e.g. Ferraro et al. 2003). The vibrational energy (or frequency) can change if either the mass of the atoms involved in the vibration changes or if the elastic constants of the lattice change. The former is typical for isostructural substitution (e.g., in Mg-Fe silicates) and the latter is related to bond length and, therefore, often occurs if substitution mechanisms influence lattice parameters of a mineral. Many minerals have at least some vibrational modes that show a shift in the naturally occurring range of compositions that is large enough to be easy to measure precisely. After identifying the corresponding Raman bands and determining correlation equations between Raman band positions and chemical composition, Raman spectroscopy can thus be used to measure composition. This technique has been applied previously, e.g. to olivine (Kuebler et al., 2006), feldspar (Freeman et al., 2008), and garnet (Bersani et al., 2009), as well as silicate glass (Robinet et al., 2008), and relies on the same basic idea as the determination of pressure from Raman band positions in quartz (e.g., Schmidt and Ziemann, 2000). In this study, we investigate the potential of this methodology for determining F concentration in topaz and discuss which Raman bands are best suited for this purpose. We present analytical protocols and recommendations to calculate the F concentration in topaz from measured Raman spectra, based on analyses on different large topaz crystals with a range of typical F/OH ratios. We then demonstrate the application of the method on a sample from a typical greisen zone in single point analyses as well as mapping.

3.2. Methods and Samples

3.2.1. X-ray powder diffraction

The X-ray diffractometry (XRD) data were obtained at the Institute of Geological Sciences, Free University Berlin, using a PANalytical Empyrean diffractometer, equipped with a PIXcel1D-Medipix3 detector. Copper Kα radiation at λ = 1.54060 Å was used with 40 kV acceleration voltage and 40 mA tube current. A 10 mm beam mask, 0.04 rad soller slits, and a fixed 1/8° divergence slit were used on the incident beam, and 7.5 mm anti-scatter slit, 0.04 rad soller slit, and a 20 μm thick Ni Kβ filter on the diffracted beam. The powders were placed on a rotating Si single crystal and scanned from 15 to 80°2θ in 4950 steps of 0.013°2θ with a total counting time of 118 s.

Rietveld refinement of the XRD data was performed with the GSAS-II software package (Toby and Von Dreele, 2013). The instrument parameter file was produced from lanthanum hexaboride (LaB_6) powder as reference material, using the same measurement conditions as for the samples. The lattice parameters, atom positions, and orientation were refined but the symmetry of the structure was kept

fixed at *Pbnm*. A published topaz structure file (Gatta et al., 2006) was used as a starting point for the Rietveld refinement but was converted to end-member F-topaz. The samples were then fitted as if they were end-member F-topaz. This does not change the outcome of the lattice parameters but merely the relative intensities of the individual reflections. This improves repeatability of the fitting results because it avoids over-fitting, which often occurs in such cases when attempting to refine the F/OH ratio, due to the similar X-ray absorption cross sections of F and O. Because only the lattice parameters are of interest for this study, the F/OH ratios were not adjusted.

The uncertainty of F/OH fraction determined from the lattice parameters stems predominantly from the error of the fluorine-determination in the input data of the correlation equation by Ribbe and Rosenberg (1971). This absolute error of approximately ±0.2 wt. % F translates to 0.02 on the F-site occupancy or 0.01 on the F/OH fraction, based on then individual errors of the 13 samples reported by these authors. However, based on the excellent correlation of r=-0.967 between F content and *b*-parameter in the data from n=13 samples of Ribbe and Rosenberg (1971), the relative error between any two topaz specimens is estimated to be less than ±0.1 wt. % F.

3.2.2. Raman spectroscopy

All Raman spectra were recorded in reflection geometry on a WiTec alpha 300 R Raman microscope with a Nd:YAG laser, frequency doubled to 532 nm, a UHTS300 VIS spectrometer with a 1800 mm^{-1} grating, and a 1650 line CCD area detector. Three different settings were used for:

1) The spectra used for the band position fits of the seven samples with different compositions were taken with a Zeiss EC Epiplan 10x / 0.25 objective and 20 mW laser power on the sample for 30 accumulations of 10 s each. Measurements were taken on the cleavage plane (001) and on well developed (110) crystal faces, respectively. The incident laser was circular polarized with a quartz λ/4 plate. No analyzer or other filter was applied to the signal. Calibration of the spectrometer was performed immediately before the measurements and verified afterwards, using the integrated Hg(Ar)-lamp calibration routine of the instrument. This provides an excellent calibration of the spectrometer scaling but has a residual uncertainty on the absolute band positions of ca. 0.5 cm^{-1} between different spectral center settings of the spectrometer. This was corrected using the 520.7 cm^{-1} band of a silicon wafer. This band was fitted using a Pseudo-Voigt profile and the deviation from 520.7 cm^{-1} was applied to the topaz spectra as a one-point calibration. The spectrometer was not moved between the measurements of the Si wafer and the topaz samples. The Si wafer was measured again after the measurements and the fitted peak position of the main band was reproducible within less than 0.0001 cm^{-1}. Cosmic ray events were filtered out by removing all single spectrum pixels that deviated by more than 5σ from the average for

the same pixel over the course of all accumulations. All spectra were subsequently corrected for the read-out and dark-current background of the detector, which were recorded as 1200 accumulations of 0.001 s and 360 accumulations of 10 s, respectively, with no signal on the detector. Fitting of the bands was performed with a custom Python 3 script utilizing the NumPy and SciPy libraries.

2) The orientation dependent polarized measurements of sample Tho were taken with a Zeiss LD EC Epiplan-NEOFLUAR 20x / 0.22 objective and 10 mW laser power on the sample for 30 accumulations of 20 s each. The incident laser and the recorded Raman signal both passed through a linear polarizer (LPVISA050 from Thorlabs with extinction ratio of ca. 10^7) mounted directly above the objective in left-right polarization orientation. Measurements were taken on the cleavage plane (001) and on well developed (100) and (010) crystal faces, respectively. One crystal was used for the (001) measurements and a second one for both (100) and (010). For each of these three principal orientations the sample was rotated using a manually rotatable sample stage, with measurements taken every 10° from 0° to 360°. The center of rotation was calibrated beforehand to coincide with the measurement spot to ensure that all spectra originate from the same place on the sample. Each of the three series with one full rotation took one day to perform. At the beginning of each day, the spectrometer was calibrated using the integrated Hg(Ar)-lamp of the instrument. No additional calibration to the 520.7 cm^{-1} band of silicon was applied for these measurements.

3) The single spectra of sample Zin were recorded with circular polarized laser light through a Zeiss EC Epiplan 10x / 0.25 objective at 20 mW laser power on the sample for 30 accumulations of 20 s each. The Raman mapping used the same conditions except with 6 accumulations instead of 30. The spectrometer was calibrated using the integrated Hg(Ar)-lamp before the measurements (no additional calibration to the 520.7 cm^{-1} band of silicon). The single spot analyses were background-processed and fitted the same way as the seven samples used for determination of the correlation equations.

The Raman bands are fitted individually with a semi-automated fitting routine as the sum of an arbitrary number of symmetric pseudo-Voigt peaks. For each peak, four parameters were fitted: Position, amplitude, width, and Lorentzian fraction. The background was also fitted as a series of pseudo-Voigt peaks, simultaneously with the Raman bands. The advantage of this way of background fitting is that it is mostly independent of human input and thus more reproducible than methods relying on (semi-)manual background definition before the actual fitting. A fit was deemed good, once the residual was around 1% of the maximum intensity of the highest peak or less and no obvious Raman bands were left unfitted.

Table 3.1. Sample information and literature recommendations.

Sample	Locality	Appearance	Comments
Alt	Altenberg, Saxony, Germany	Milky, yellow	Variety pycnite from stockscheider pegmatite (Breiter et al., 2013)
Pak	Pakistan	Clear, colorless	Exact provenance unknown (Loges et al., 2022)
Sch	Schneckenstein, Saxony, Germany	Fairly clear, yellowish	Greisen topaz breccia (Zeug et al., 2022)
Spi	Klein Spitzkoppe, Damaraland, Namibia	Clear, colorless	Pegmatite (Cairncross et al, 1998)
Tep	El Tepetate, San Luis Potosí, Mexico	Clear with inclusions, orange	Tepetate rhyolite (Leroy et al., 2002)
Tho	Thomas Range, Utah, USA	Clear, colorless	Topaz mountain rhyolite, (Holfert et al., 1996)
Vil	Ouro Preto, Minas Gerais, Brazil	Fairly clear, orange	"Imperial topaz", near town formerly called Vila Rica (Gauzzi et al., 2018)
Zin	Zinnwald/Cínovec	Clear with inclusions, colorless	Not used for correlation equation (Qiao et al., 2024)

3.2.3. Samples

A total of seven different topaz samples were used for the investigation of the correlation between Raman spectra and F concentration. These were all 0.5 to 3 cm large single crystals, from which small pieces (ca. 1 mm^3) were broken off. Of these pieces, three Raman spectra were recorded in evenly spaced locations on the (001) cleavage plane. Afterwards, these same pieces were ground in an agate hand mortar and used for XRD analysis. All but one of these samples come from well-known topaz localities and are commercially available in (near-)gem quality and described in published literature (Table 3.1). Sample Pak was purchased from a mineral trader with no provenance information available other than the country of origin (Pakistan). The series of oriented measurements were taken on two crystals from Topaz Mountain, Thomas Range, Utah, USA (sample Tho). This locality is known for gem-quality topaz crystals very close to F end-member composition hosted in light-gray rhyolite (Patton, 1908; Ribbe and Rosenberg, 1971). Topaz is associated in this locality with other minerals typical of pneumatolytic

alteration in highly evolved rhyolite (Holfert et al., 1996). Samples Pak and Tho have previously been investigated and described in Loges et al. (2022).

The sample used for testing the *in-situ* application of Raman spectroscopy for determination of F concentration in topaz (sample Zin) was a thin section of a greisen halo around a fissure (or vein) in rhyolite from Zinnwald/Cínovec and has been described in detail in Qiao et al. (2024a). We chose a transect containing greisen and some host rhyolite, from which 19 topaz grains were studied using cathodoluminescence (CL), optical microscopy and Raman spectroscopy (Fig. 3.1).

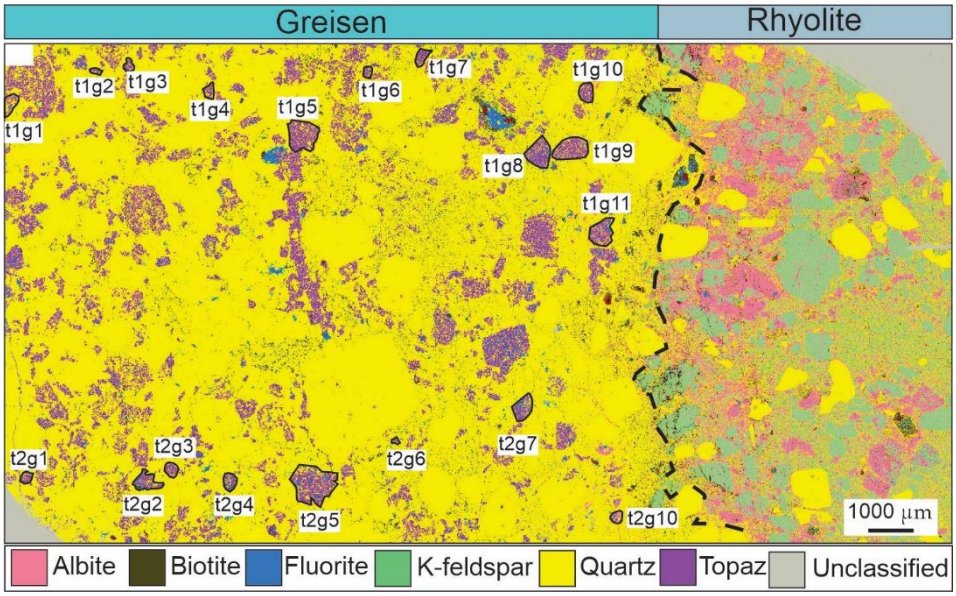

Fig. 3.1**.** SEM-EDS mineral mapping of sample Zin, a topaz-rich greisen transect (modified after Qiao et al., 2024). The labeled topaz grains are the grains measured by Raman spectroscopy. The black dashed line marks the boundary between greisen and rhyolite zone.

Table 3.2. Results of XRD measurements (in Å) and fitted positions of select Raman bands (in cm^{-1}). The precision and uncertainties of the XRD results are reported as given by the GSAS-II software. The F concentration was calculated from the b lattice parameter (Ribbe and Rosenberg, 1971). For associated uncertainty see Methods. Raman bands of the three individual measurements on the (001) plane of all seven correlation equation samples as well as the three total analyses on the (110) faces. Estimated uncertainty on the Raman band position fit is ±0.05 cm^{-1}. Columns are labeled with the "nominal positions" of the respective bands in the F endmember sample Tho.

Sample	*a* [Å]	*b* [Å]	*c* [Å]	F [wt. %]	*155* [cm^{-1}]	*240* [cm^{-1}]	*268* [cm^{-1}]	*286* [cm^{-1}]	*332* [cm^{-1}]	*521* [cm^{-1}]	*562* [cm^{-1}]
Alt_(001)-1	4.65029(6)	8.79830(11)	8.39098(9)	19.71	155.34	240.27	268.23	286.45	332.74	520.46	560.78
Alt_(001)-2	”	”	”	”	155.38	240.37	268.46	286.50	332.69	520.12	560.03
Alt_(001)-3	”	”	”	”	155.28	240.27	268.25	286.42	332.74	520.47	560.81
Pak_(001)-1	4.65120(6)	8.80105(12)	8.38961(9)	19.44	155.86	240.79	268.90	286.82	333.07	520.26	560.08
Pak_(001)-2	”	”	”	”	155.83	240.77	268.90	286.87	333.09	520.30	560.09
Pak_(001)-3	”	”	”	”	155.84	240.77	268.89	286.81	333.08	520.30	560.14
Sch_(001)-1	4.65250(6)	8.80412(12)	8.38936(10)	19.13	156.10	240.90	269.14	287.01	333.15	519.95	559.35
Sch_(001)-2	”	”	”	”	155.89	240.76	268.89	286.83	333.00	520.06	559.97
Sch_(001)-3	”	”	”	”	155.86	240.74	268.86	286.80	332.98	520.15	559.99
Sch_(110)	”	”	”	”	156.19	240.99	269.22	287.04	333.33	520.03	559.22
Spi_(001)-1	4.65274(6)	8.80499(11)	8.38902(9)	19.04	156.19	241.00	269.26	287.28	333.26	519.91	558.54
Spi_(001)-2	”	”	”	”	156.17	241.01	269.22	287.21	333.22	519.95	558.65
Spi_(001)-3	”	”	”	”	156.24	241.10	269.28	287.27	333.28	519.97	559.27
Tep_(001)-1	4.66299(6)	8.83455(12)	8.38623(9)	16.11	158.73	242.07	271.69	289.71	336.09	518.25	553.06
Tep_(001)-2	”	”	”	”	158.34	241.65	271.34	289.28	335.41	518.45	553.28
Tep_(001)-3	”	”	”	”	159.07	242.31	272.04	290.07	336.57	517.72	553.40
Tep_(110)	”	”	”	”	158.80	241.67	271.64	289.40	336.42	519.65	552.81
Tho_(001)-1	4.64804(6)	8.79093(13)	8.39246(9)	20.44	154.60	239.89	267.65	285.99	332.30	520.60	562.05
Tho_(001)-2	”	”	”	”	154.50	239.81	267.67	286.06	332.35	520.66	562.09
Tho_(001)-3	”	”	”	”	154.59	239.87	267.66	286.09	332.37	520.72	562.22
Tho_(110)	”	”	”	”	154.59	239.87	267.67	286.03	332.38	520.75	561.88
Vil_(001)-1	4.65258(7)	8.80472(14)	8.38889(11)	19.07	156.10	240.89	269.12	286.99	333.16	519.99	559.65
Vil_(001)-2	”	”	”	”	156.13	240.95	269.18	287.07	333.18	519.94	559.47
Vil_(001)-3	”	”	”	”	156.06	240.89	269.11	286.93	333.10	519.91	558.65

3.3. Results and Discussion

3.3.1. X-ray diffraction

The results of the Rietveld analyses are summarized in Table 3.2, along with the F concentration calculated from the *b* lattice parameter using the relation F [wt. %] = 892.5 – 99.2 × *b* [Å] (Ribbe and Rosenberg, 1971). The corresponding raw data and figures of merit are found in the electronic appendix. Six of the seven samples clustered closely together (19.04 – 20.44 wt. % F), whereas sample Tep had a significantly lower F concentration (16.11 wt. %). The total range of compositions closely matches that of Ribbe and Rosenberg (1971).

3.3.2. Orientation dependent Raman measurements

Raman spectra of oriented sample in 10° rotation increments around the three principal crystallographic axes of gem-quality crystals from Thomas Range (sample Tho) are shown in Fig. 3.2. Most Raman bands either disappear completely in some orientations or vary strongly in intensity. The three main bands between 200 and 300 cm^{-1} are always present but have additional shoulders in some orientations. The bands at 155 and 562 cm^{-1} are the most stable of the sharp bands with respect to sample orientation.

3.3.3. Raman spectral features of topaz

Three spectra were recorded on the (001) plane for each of the seven samples used for investigation of the correlation between Raman spectrum and F concentration in topaz. The three spectra of each sample are too similar to each other to be distinguished in a plot. The averages of each set of three are shown in Fig. 3.3. The bands below 700 cm^{-1} are sharp with typical FWHM values of 2 – 10 cm^{-1}, whereas those above 800 cm^{-1} are broader with FWHM up to 30 cm^{-1}. The FWHM of the bands also depends on the F concentration with F-richer samples having sharper bands, with higher F corresponding on sharper band. Several bands that are distinct in the F-rich samples merge together as the F concentration decreases. One band, between 1155 and 1160 cm^{-1} becomes weaker with increasing F concentration and is entirely absent in the F endmember sample Tho.

A comparison of Raman spectra recorded in different orientations, perpendicular to (001) and to (110), is shown for three samples (Tho, Sch, and Tep) in Fig. 3.4. The three main bands between 200 and 300 cm^{-1} as well as the bands above 800 cm^{-1} all consist of several sub-bands, whose relative intensities vary with orientation and are difficult to separate. A small additional band at 165 cm^{-1} can be

seen in the (110) spectra, which does not appear in the (001) spectra. This band is, however always clearly separated from the neighboring band at about 155 cm^{-1}, due to the sharpness of these bands.

Some of the major band positions are listed in Table 3.3. We will, in the following, refer to bands by their position in the F endmember sample from Thomas Range, rounded to the nearest full wave number, e.g., "155 band" for the band that occurs at 155.5 to 155.6 cm^{-1} in sample Tho. The reproducibility of band position fits within each set of three spectra for the individual samples is about ±0.1 cm^{-1} for most bands, with some outliers of up to ±0.5 cm^{-1}. The band positions in Table 3.3 all vary with composition but the correlation between F concentration and band position can be negative (155, 240, 268, 286, and 322 band) or positive (521 and 562 band). The 521 band shows the least variation (ca. 2 cm^{-1} difference between the most extreme samples), whereas the 562 band has the largest (> 11 cm^{-1}).

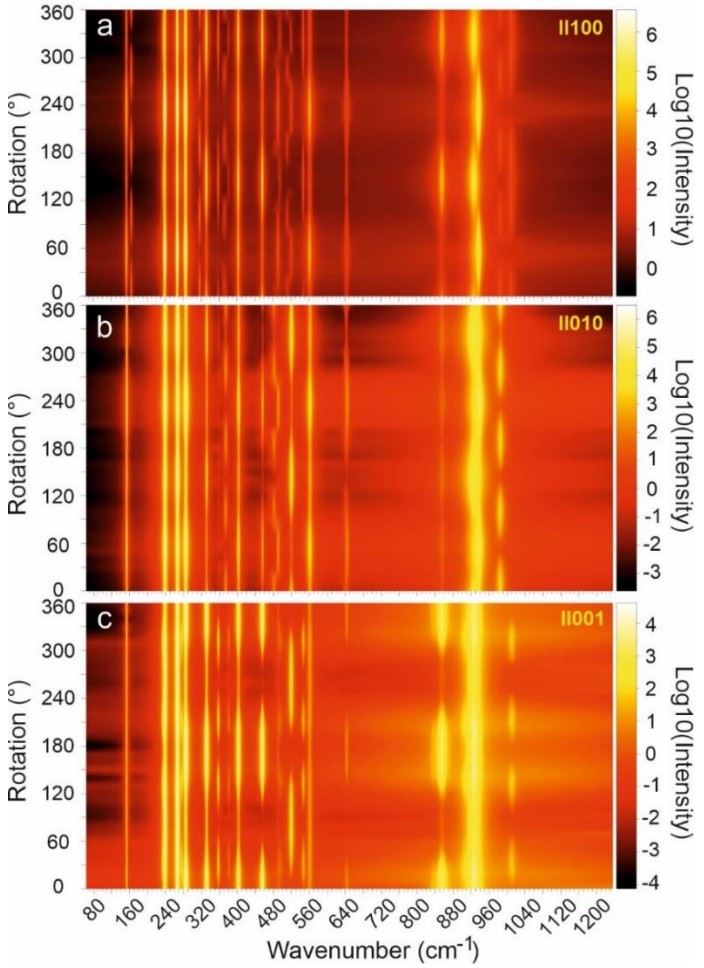

Fig. 3.2. Oriented Raman measurements of sample Tho. Shown are the raw spectra without background correction as intensity maps.

3.3.4. Determination of F concentration with Raman spectroscopy

For a maximally useful correlation equation linking parameters extracted from Raman spectra with the F concentration in topaz, we need to identify Raman bands whose (1) position shows a simple (preferably linear) and strong correlation with the F concentration in topaz, that (2) are present in all orientations and (3) can be reliably fitted. The third condition requires that the bands are not too close to another band because different bands can change relative intensity with orientation, which may impact the reproducibility and precision of band position fitting, depending on the quality and resolution of the spectrum. The three most intense bands between 200 and 300 cm^{-1} and the high-energy bands above 800 cm^{-1} are not ideal for our purposes because they are each composed of several sub-bands, whose relative intensity to one another changes with orientation (Fig. 3.2, 3.3, 3.4). This makes the exact band position potentially subject to data quality and fit strategy, which reduces reproducibility between different operators. Most other bands disappear in some orientations (Fig. 3.2). Only the 155 band fully satisfies all conditions set above. Plotting the position of this band against the F concentration determined by XRD using the correlation equation of the *b*-parameter (Ribbe and Rosenberg, 1971), yields a strong, linear, negative correlation (R = -0.9911) with the band position changing from ca. 159 cm^{-1} at 16 wt. % F to 155 cm^{-1} at 20.5 wt. % F (Fig. 3.5). The 562 band also has a strong but positive correlation (R = 0.9927) with the F concentration in wt. % and also appears in all orientations but is close to the 547 band. These two are well resolved in the sample Tho but move closer together in more OH-rich samples, fully merging at 553 cm^{-1} in sample Tep with 16 wt. % F (Fig. 3.3). Among the three most intense Raman bands of topaz, the 268 band shows the best correlation (R = -0.9895) with F concentration and can be most reliably fitted in various orientations if the shoulders affecting this peak are also fitted properly. Linearly fitting the F concentrations derived from the XRD measurements to the positions of the three bands discussed above yields the following functions (where "$\tilde{\nu}_{xxx}$": stands for the energy of the xxx band in cm^{-1}):

$$F\ [wt.\ \%] = 181.8(4.6) - 1.043(30) \times \tilde{\nu}_{155} \qquad \text{(Eq. 1)}$$

$$F\ [wt.\ \%] = 308.0(9.0) - 1.074(33) \times \tilde{\nu}_{268} \qquad \text{(Eq. 2)}$$

$$F\ [wt.\ \%] = -247.5(6.9) + 0.477(12) \times \tilde{\nu}_{562} \qquad \text{(Eq. 3)}$$

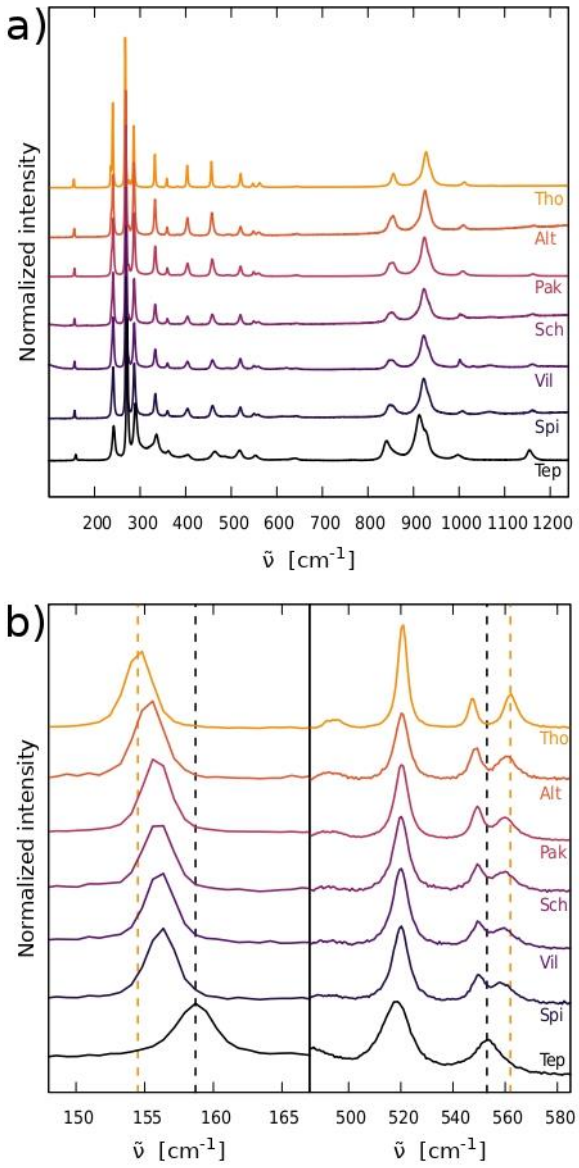

Fig. 3.3. (a) Raman spectra of the seven different topaz samples ordered from lowest (Tep) to highest (Tho) F concentration (compare Table 3.2). Each spectrum shown here is the average of the three raw spectra collected for each spectrum on the (001) pane without background subtraction. (b) Details around the 155 and 562 bands of the same spectra.

Any one of these can in principle be used to determine F concentration from Raman spectra. However, doing so relies on the accuracy of the absolute calibration of the spectrometer, as well as the spectrometer scaling. In our experience with various Raman spectrometers by different manufacturers, the scaling calibration tends to be much more stable and reproducible than the calibration of the absolute position of the spectrometer. To account for this, a known standard, such as single crystalline silicon should always be measured along with the samples and the known band position (e.g., 520.7 cm^{-1} in

silicon) should be fitted the same way as the samples. The offset observed in the standard should then be used to apply a one-point correction to the samples. The standard should be measured regularly throughout a measurement session to monitor possible spectrometer drift.

Use of a one-point calibration is unnecessary if, instead of a single band, the distance between to bands is used to determine F concentration. Using the distance between the 155 and 562 bands has the added benefit of increased resolution and decreased uncertainty because the positions of these two bands show opposing trends with F concentration in topaz (Fig. 3.5). The corresponding fitted correlation equation is:

$$F\ [\text{wt. \%}] = -113.6(2.8) + 0.329(7) \times (\tilde{\nu}_{562} - \tilde{\nu}_{155}) \qquad \text{(Eq. 4)}$$

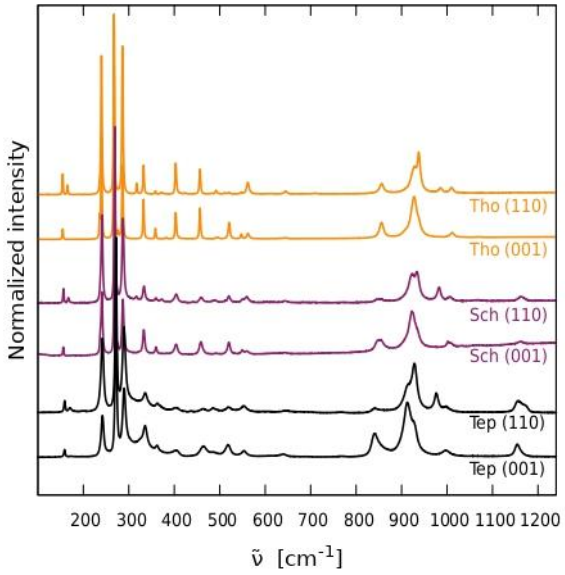

Fig. 3.4. Comparison of spectra in different orientations, (001) and (110), for three of the samples.

The total uncertainty of the determination of F concentration from Raman spectra consists of several contributions. The fitting uncertainties (1σ) of the calibrations undertaken here are given in parentheses in equations 1-4. However, because F concentrations used to derive these equations were calculated from XRD using the method of Ribbe and Rosenberg (1971), the uncertainties of their method also carry over (ca. ±0.2 wt. % F, see Methods). The uncertainties of the Rietveld refinement (Table 3.2) are negligible by comparison. Finally, the quality of the Raman spectra and band fits also impart an uncertainty on the thus calculated F concentration. This factor obviously depends on the instrument calibration and quality of individual measurements on topaz samples, for which the user of the above calibrations may wish to calculate the F concentration and can thus not be included here. Assuming

proper spectrometer calibration, good spectrum quality and correct band position fitting, we estimate the total uncertainty on accuracy of the method proposed here, including all systematic offsets, to be better than ±0.5 wt. % F. The relative uncertainty between samples measured on the same machine with consistent analytical conditions and identical peak fitting procedures is estimated to be around ±0.1 wt. % F (uncertainty on precision or reproducibility).

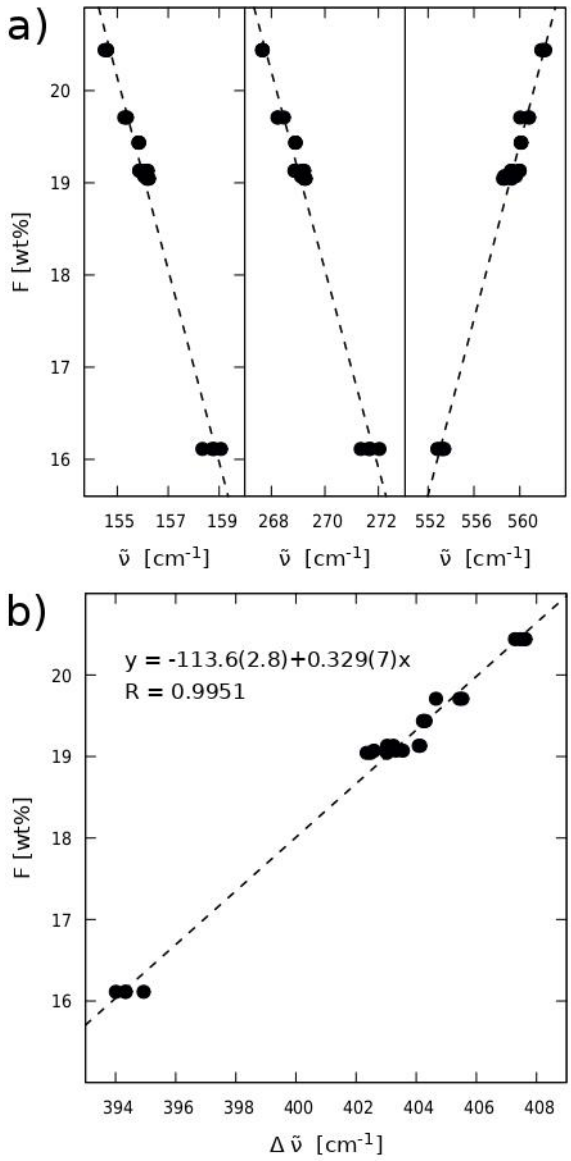

Fig. 3.5. (a) Correlation of the F concentration in topaz with the positions of the 155, 268, and 562. Fitted band positions from Table 3.3. (b) Correlation fit and equation for determination of F [wt. %] in topaz based on the distance between the 155 and 562 Raman bands.

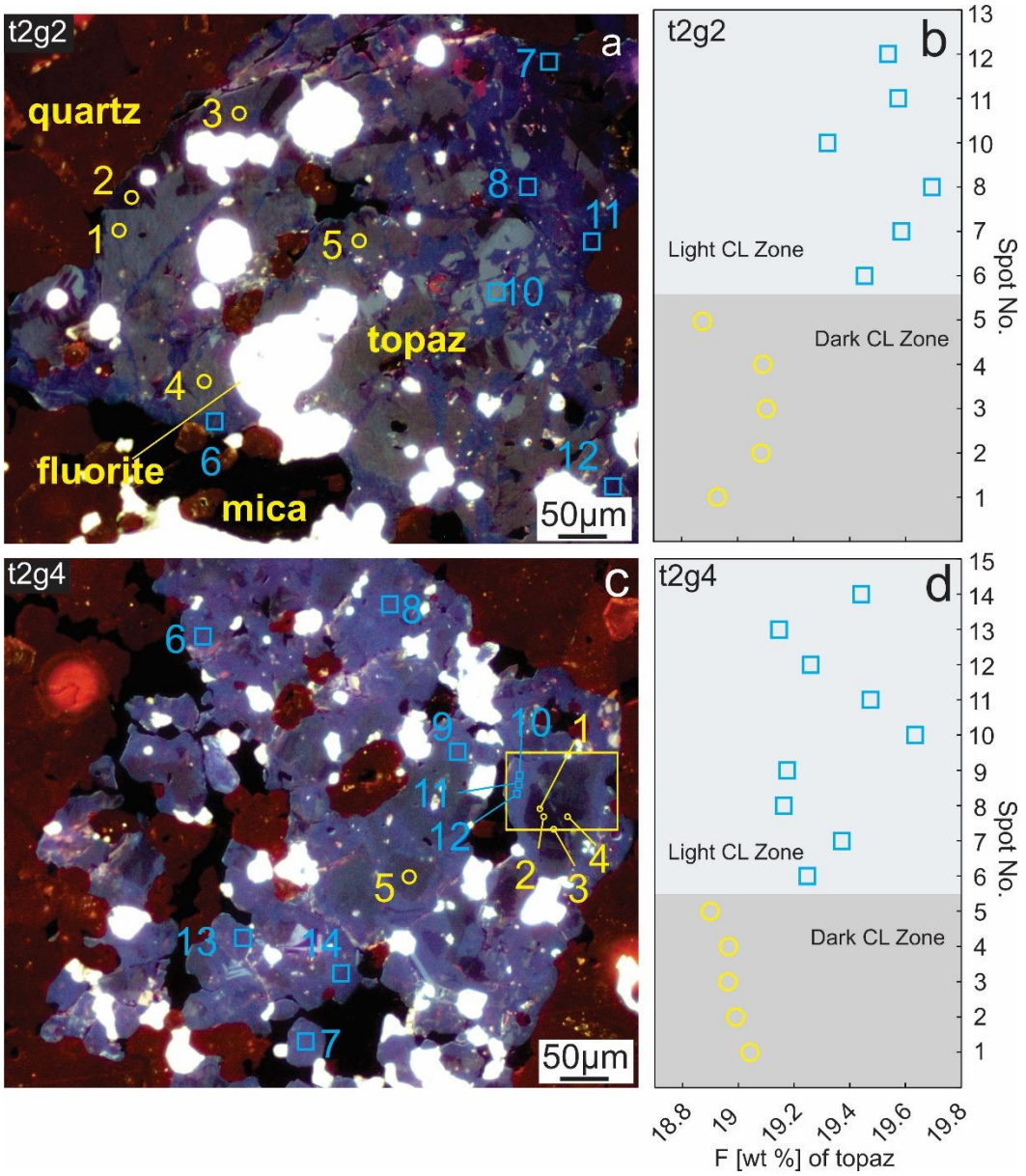

Fig. 3.6. Raman analysis of representative topaz grains in thin section sample Zin. (a) and (c) CL images with the spots of measurement spots; (b) and (d) F concentration in topaz calculated using the distance between the 155 and 562 bands. The blue square and yellow circle represent the spots in the light and dark CL zones, respectively. The light CL zone has a higher F concentration than the dark zone.

3.3.5. Application example: thin section Zin

Cathodoluminescence images show that the topaz grains in sample Zin are zoned (Fig. 3.6). The darker CL zones are surrounded by brighter zones in some grains. No difference is found in crystallographic orientation between the two zones with cross polarized optical microscopy. A total of 203 Raman spot measurements were taken on all the topaz grains marked in Fig. 3.1, including 94 spots from the lighter

CL zones and 109 spots from the darker CL zones. As an example, F concentration from two representative topaz grains are shown in Fig. 3.6. The F concentrations calculated from the distance between the 155 and 562 bands (Eq. 4) of the darker CL zones are systematically lower than those of the lighter CL zones. Across the transect, a clear difference is observed between the two zones (Fig. 3.6 and 3.7). Most spots in the lighter CL zones exhibited higher F concentrations (mean value: 19.4 ± 0.2 wt. %), whereas spots in the darker CL zone generally have lower F concentrations (mean value: 19.0 ± 0.2 wt. %). Within a single grain, F concentration varies by 0.5 wt. % in lighter CL zones and 0.3 wt. % in darker zones. In Fig. 3.7, the F concentrations of the two types of zones in individual grains are separately averaged and visualized with square symbols. Both types of topaz show a slight decrease in F concentration by ca. 0.1 wt. % towards the wall rock across the transect.

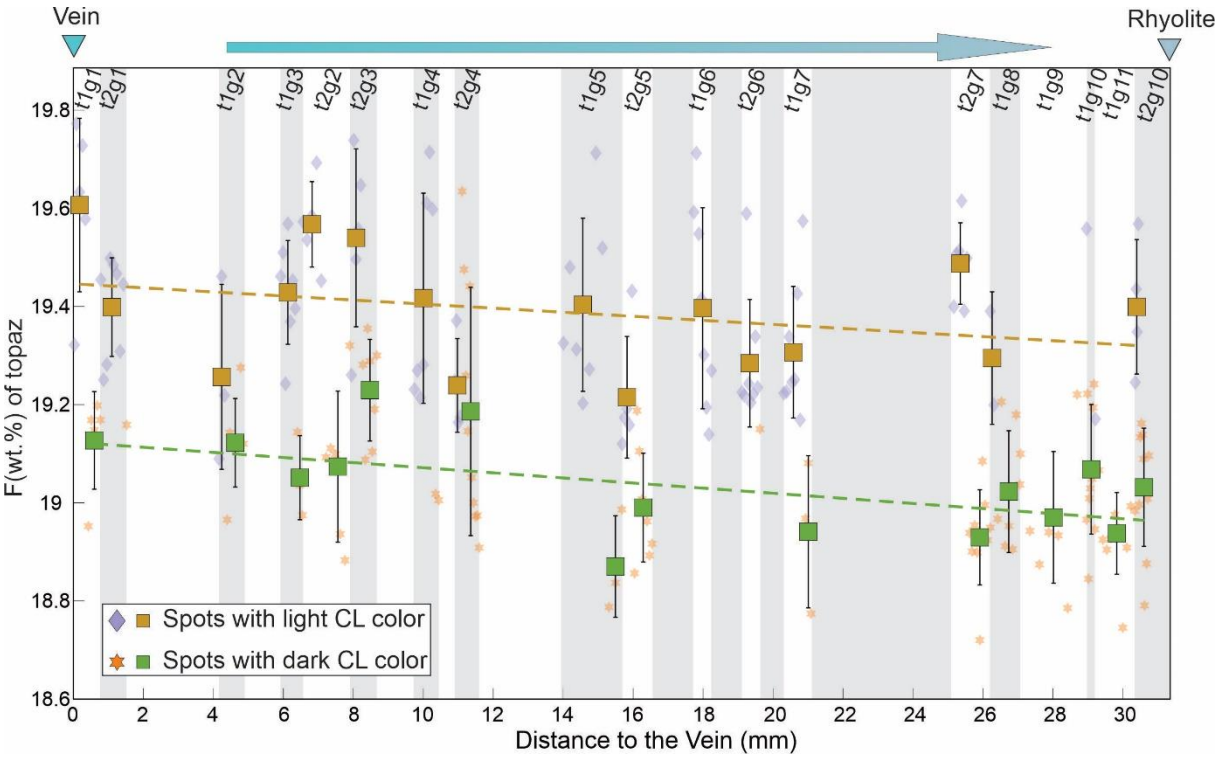

Fig. 3.7. Fluorine concentration in topaz from the Zinnwald/Cínovec quartz-topaz greisen transect (Zin) obtained with Raman spectroscopy. Labels (top) correspond to Fig. 3.1. Squares indicate the mean F concentration in the light (light brown symbol) and dark (green symbol) CL zones within single topaz grains, with error bars showing 1 sigma of each zone in each grain.

A Raman map was recorded to test if the difference in F concentration between the two CL zones can be quantified in such a map (Fig. 3.8). The area mapped is homogeneous in crossed polarized transmission light microscope images. The sharp boundary between the dark inner and light outer zones

of topaz in the CL image is marked by a ca. 1 wt. % difference in F concentrations. A fracture cutting through the topaz grain characterized by a higher F concentration can be clearly visualized in the mapping (Fig. 3.8). The zoning in CL images is well reproduced with the Raman F concentration map but there are additional details visible, especially in the light zone, highlighting the potential utility of this method, especially for topaz samples with complex zoning. Plotting the F concentration of all pixels from a small, apparently homogeneous area in a histogram, provides a good estimate of the random uncertainty imparted by the data quality (Fig. 3.8 d). In the case of the data shown in Fig. 3.8, the 1σ uncertainty is 0.1 wt. % F. This procedure can serve as a tool for optimizing spectrum acquisition conditions and times for a given purpose.

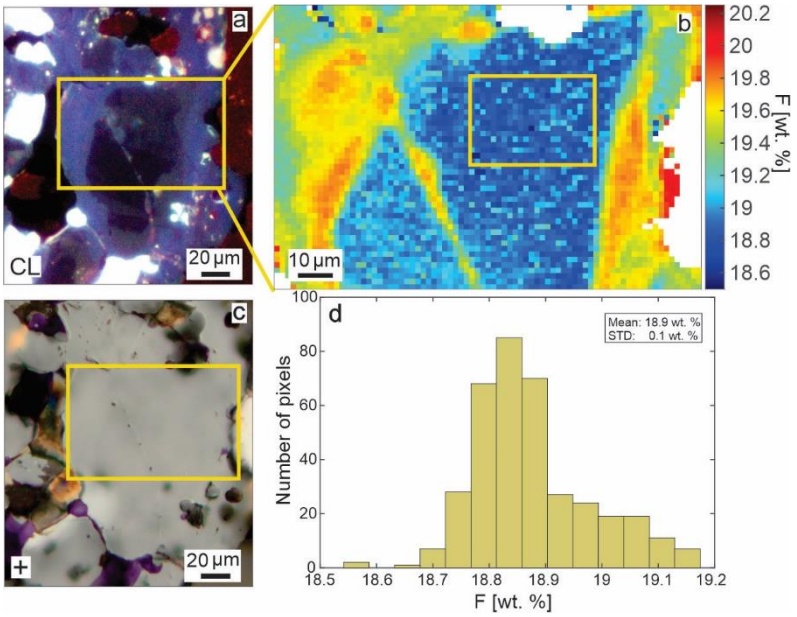

Fig. 3.8. (a) CL image and (b) Raman mapping from sample Zin. a) optical microphotograph for comparison. The Raman mapped area is marked by the yellow box in a and c and Fig. 3.6 c. High F concentrations correspond to the lighter CL zones in a. Fluorine concentration is calculated from the distance between the 155 and 562 bands (Eq 1). (d) Histogram of F concentration per pixel inside the yellow box in b).

3.3.6. Recommended procedures

To obtain the most reliable F concentrations from Raman spectra of topaz, different strategies may be needed, depending on the achievable spectral quality in a given sample. In all cases, proper calibration of the spectrometer is critical. We recommend that the spectrometer be calibrated using a suitable fluorescent light source. These are built into many modern Raman spectrometers but small external

lamps are also available, which can be measured in place of a sample and used for instrument calibration. In addition, a one-point calibration on a substance with a well-defined strong Raman band should be carried out, e.g., with the 520.7 cm^{-1} band of a silicon single crystal. All samples that shall be compared should ideally be measured in a single session with the same calibration. At the end of the session, the calibration should be checked to verify that the spectrometer did not drift. Laser polarization is not critical. Cathodoluminescence imaging is a powerful tool for discerning zonation patterns and other sources of heterogeneity in topaz (as well as many other minerals) and has proven useful for picking the interesting areas and spots to then measure with Raman.

For the measurements and data treatment, we recommend the following procedure:

1. Obtain high-quality Raman spectra of topaz covering at least 100 – 600 cm^{-1}. If different lasers are available, use the one that produces the lowest fluorescence on your samples.

2. Remove cosmic ray interference and detector artifacts from the spectra if present.

3. Fit pseudo-Voigt functions to all Raman bands. Ideally, the background should be fitted simultaneously with the bands but can also be subtracted prior to band fitting.

4a. If the 155 and 562 bands can be fitted well, calculate the F concentration as:
$F\ [wt.\ \%] = -113.6 + 0.329 \times (\tilde{\nu}_{562} - \tilde{\nu}_{155})$

4b. If only the 155 band can be fitted well but not the 562 band, calculate the F concentration as:
$F\ [wt.\ \%] = 181.8 - 1.043 \times \tilde{\nu}_{155}$

4c. If none of the weaker bands can be fitted reliably but the main bands can, then calculate the F concentration using the 268 band (remembering to also fit any shoulders that may influence the fitted position) as:

$F\ [wt.\ \%] = 308.0 - 1.074 \times \tilde{\nu}_{268}$

3.4. Implications

Raman spectroscopy can be used to accurately, precisely, and rapidly determine F concentration in topaz, using the obtained correlation equations (Eq. 1-4). Because the method is easy to use, widely available, and requires minimal sample preparation (especially if the samples are already in the form of thin or thick sections for use with other analytical methods), it is suitable for quickly producing data sets of statistically relevant size, which is particularly important if the results are to be used as input data for thermodynamic equilibrium calculations. Fluorine concentrations in fluids and melts and their influence on the chemical and mineralogical development of the system are still not well understood, partly due to difficulties with analyzing fluorine outlined in the Introduction. Because topaz is a common mineral

in granitoid magmatic rocks, pegmatites, and hydrothermal veins, and often the main F carrier phase (at least in the absence of fluorite or large amounts of F-rich mica), the method presented here may be ideal to help expand our knowledge of the influence of fluorine in exactly the type of geological systems, where its influence is largest.

Recent studies have shown that F, together with pH, critically controls the formation of transient porosity and thus permeability via topaz formation from metasomatized feldspar in greisen systems, which host economically important W-Sn-Li deposits (Qiao et al., 2024a, 2024b). Being able to quantitatively model such reactions requires precise knowledge of F concentrations in the fluid and is crucial because porosity and permeability are among the main controlling factors for the development of large ore deposits (e.g., Weis, 2015). Systematic studies on F in topaz from host granite through greisen formation to late hydrothermal stage will thus help better understand the development of F-rich granitic systems during and after the magmatic-hydrothermal transition as well as the often associated ore formation.

Acknowledgements

The authors thank Jeremy Fuller for the samples and documentation of the Thomas Range samples, as well as R. Johannes Giebel (Technische Universität Berlin) and Moritz Liesegang (Freie Universität Berlin) for the remaining samples. This project was funded by the German Research Foundation (gefördert durch die Deutsche Forschungsgemeinschaft (DFG) – Projektnummer 387284271 – SFB 1349) and the China Scholarship Council (201908110287).

References

Alberico, A., Ferrando, S., Ivaldi, G., and Ferraris, G., 2003. X-ray single-crystal structure refinement of an OH-rich topaz from Sulu UHP terrane (Eastern China) Structural foundation of the correlation between cell parameters and fluorine content. European Journal of Mineralogy, 15, 875-881.

Barton, M.D., 1982. The thermodynamic properties of topaz solid solutions and some petrologic applications. American Mineralogist, 67, 956-974.

Beny, J.M., and Piriou, B., 1987. Vibrational spectra of single-crystal topaz. Physics and Chemistry of Minerals, 15, 148-159.

Bersani, D., Andò, S., Vignola, P., Moltifiori, G., Marino, I.-G., Lottici, P.P., and Diella, V., 2009. Micro-Raman spectroscopy as a routine tool for garnet analysis. Spectrochimica Acta Part A: Molecular and Biomolecular Spectroscopy, 73, 484-491.

Breiter, K., Gardenová, N., Vaculovič, T., and Kanický, V., 2013. Topaz as an important host for Ge in granites and greisens. Mineralogical Magazine, 77, 403-417.

Ferraro, J.R., Nakamoto, K., and Brown, C.W., 2003. Introductory Raman spectroscopy, 2nd ed., 434 p. Academic Press, Amsterdam, Boston.

Freeman, J.J., Wang, A., Kuebler, K.E., Jolliff, B.L., and Haskin, L.A., 2008. Characterization of natural feldspars by Raman spectroscopy for future planetary exploration. The Canadian Mineralogist, 46, 1477-1500.

Gatta, G.D., Nestola, F., Bromiley, G.D., and Loose, A., 2006. New insight into crystal chemistry of topaz: A multi-methodological study. American Mineralogist, 91, 1839-1846.

Gauzzi, T., Graça, L.M., Lagoeiro, L., de Castro Mendes, I., and Queiroga, G.N., 2018. The fingerprint of imperial topaz from Ouro Preto region (Minas Gerais state, Brazil) based on cathodoluminescence properties and composition. Mineralogical Magazine, 82, 943-960.

Holfert, J., Mroch, W., and Fuller, J., 1996. A Field Guide to Topaz and Associated Minerals of the Thomas Range, Utah, 103 p. Vol. 1. HM Publishing.

Kramida, A., and Ralchenko, Y., 1999. NIST Atomic Spectra Database, NIST Standard Reference Database 78. National Institute of Standards and Technology.

Kuebler, K.E., Jolliff, B.L., Wang, A., and Haskin, L.A., 2006. Extracting olivine (Fo–Fa) compositions from Raman spectral peak positions. Geochimica et Cosmochimica Acta, 70, 6201-6222.

Kusebauch, C., John, T., Whitehouse, M.J., and Engvik, A.K., 2015a. Apatite as probe for the halogen composition of metamorphic fluids (Bamble Sector, SE Norway). Contributions to Mineralogy and Petrology, 170, 34.

Kusebauch, C., John, T., Whitehouse, M.J., Klemme, S., and Putnis, A., 2015b. Distribution of halogens between fluid and apatite during fluid-mediated replacement processes. Geochimica et Cosmochimica Acta, 170, 225-246.

Ladenburger, S., Walter, B.F., Marks, M.A.W., and Markl, G., 2020. Combining Ion Chromatography and Total Reflection X-ray Fluorescence for Detection of Major, Minor and Trace Elements in Quartz-Hosted Fluid Inclusions. Journal of Analytical Chemistry, 75, 1477-1485.

Leroy, J.L., Rodriguez-Rios, R., and Dewonck, S., 2002. The topaz-bearing rhyolites from the San Luis Potosi area (Mexico): characteristics of the lava and growth conditions of topaz. Bulletin de la Société Géologique de France, 173, 579-588.

Loges, A., Scholz, G., de Sousa Amadeu, N., Shao, J., Schultze, D., Fuller, J., Paulus, B., Emmerling, F., Braun, T., and John, T., 2022. Studies on the local structure of the F/OH site in topaz by magic angle spinning nuclear magnetic resonance and Raman spectroscopy. European Journal of Mineralogy, 34, 507-521.

Northrup, P.A., Leinenweber, K., and Parise, J.B., 1994. The location of H in the high-pressure synthetic $Al_2SiO_4(OH)_2$ topaz analogue. American Mineralogist, 79, 401-404.

Ottolini, L., Cámara, F., and Bigi, S., 2000. An investigation of matrix effects in the analysis of fluorine in humite-group minerals by EMPA, SIMS, and SREF. American Mineralogist, 85, 89-102.

Patton, H.B., 1908. Topaz-bearing rhyolite of the Thomas range, Utah. Geological Society of America Bulletin, 19, 177-192.

Pinheiro, M.V.B., Fantini, C., Krambrock, K., Persiano, A.I.C., Dantas, M.S.S., and Pimenta, M.A., 2002. OH/F substitution in topaz studied by Raman spectroscopy. Physical Review B, 65, 104301.

Qiao, S., John, T., and Loges, A., 2024a. Formation of Topaz-Greisen by a Boiling Fluid: A Case Study from the Sn-W-Li Deposit, Zinnwald/Cínovec. Economic Geology, 119, 805-828.

Qiao, S., Loges, A., Vrijmoed, J.C., and John, T., 2024b. Controls of F content and pH on the formation of greisen quantified by reactive transport modeling. Geochimica et Cosmochimica Acta (under review).

Raudsepp, M., 1995. Recent advances in the electron-probe micro-analysis of minerals for the light elements. The Canadian Mineralogist, 33, 203-218.

Ribbe, P.H., and Rosenberg, P.E., 1971. Optical and X-ray determinative methods for fluorine in topaz. American Mineralogist, 56, 1812-1821.

Robinet, L., Bouquillon, A., and Hartwig, J., 2008. Correlations between Raman parameters and elemental composition in lead and lead alkali silicate glasses. Journal of Raman Spectroscopy, 39, 618-626.

Saowadee, N., Agersted, K., and Bowen, J.R., 2017. Lattice constant measurement from electron backscatter diffraction patterns. Journal of Microscopy, 266, 200-210.

Schmidt, C., and Ziemann, M.A., 2000. In-situ Raman spectroscopy of quartz: A pressure sensor for hydrothermal diamond-anvil cell experiments at elevated temperatures. American Mineralogist, 85, 1725–1734.

Thompson, A., Lindau, I., Attwood, D., Liu, Y., Gullikson, E., Pianetta, P., Howells, M., Robinson, A., Kim, K.-J., Scofield, J., and others, 2009. X-Ray Data Booklet, 3rd ed. Center for X-Ray Optics and Advanced Light Source, Lawrence Berkeley National Laboratory, UC Berkeley.

Toby, B.H., and Von Dreele, R.B., 2013. GSAS-II: the genesis of a modern open-source all purpose crystallography software package. Journal of Applied Crystallography, 46, 544-549.

Watenphul, A., Libowitzky, E., Wunder, B., and Gottschalk, M.: The OH site in topaz: an IR spectroscopic investigation, Phys. Chem. Miner., 37, 653–664.

Weis, P., 2015. The dynamic interplay between saline fluid flow and rock permeability in magmatic-hydrothermal systems. Geofluids, 15, 350-371.

Wunder, B., Andrut, M., and Wirth, R., 1999. High-pressure synthesis and properties of OH-rich topaz. European Journal of Mineralogy, 11, 803-814.

Zeug, M., Nasdala, L., Chanmuang N., C., and Hauzenberger, C., 2022. Gem Topaz from the Schneckenstein Crag, Saxony, Germany: Mineralogical Characterization and Luminescence. Gems & Gemology, 58, 2-17.

Zhang, R.Y., Liou, J.G., and Shu, J.F., 2002. Hydroxyl-rich topaz in high-pressure and ultrahigh-pressure kyanite quartzites, with retrograde woodhouseite, from the Sulu terrane, eastern China. American Mineralogist, 87, 445-453.

Chapter 4. Controls of F content and pH on the formation of greisen quantified by reactive transport modeling

Shilei Qiao [a,*], Anselm Loges [a], Johannes C. Vrijmoed [a], Timm John [a]

[a] Institut für Geologische Wissenschaften, Freie Universität Berlin, Malteserstr. 74-100, 12249 Berlin, Germany

Abstract

Greisenization is a fluid-driven alteration process of felsic rocks that is responsible for the formation of some major ore deposits. Normally, greisen variations include mainly quartz-topaz and quartz-mica assemblages, suggesting different formation conditions. The controlling factor for this variation, however, is not well known. To investigate this, we applied reactive transport modeling to simulate the greisenization process. Our one-dimensional (1D) numerical model with different initial fluid compositions was able to recreate the formation sequences of known natural greisen types and provides insights into the corresponding evolution in fluid chemistry and porosity.

Specifically, modeling results show that the relative change of topaz and mica abundances constitute a petrogenetically relevant difference between different types of greisen. The stability field of mica-free quartz-topaz greisen suggests that mica is not a universally present phase in greisenization, and the formation of quartz-topaz greisen corresponds to a higher transient porosity (14 %) than is found in quartz-mica greisen (8 %) during greisenization. Further, the modeling of quartz-mica and quartz-topaz greisen formation indicates that both the pH value and the F content of the infiltrating fluid controls the mineralogical variation of greisen. Mica is stable at moderately low pH values (>3.2), but it becomes unstable in fluids with high F concentrations (>0.0001 mol/kg). Topaz formation is supported by fluids with low pH values (<5.8) and variable F concentrations (>2.9×10^{-6} mol/kg). To form greisen that has a sequence of quartz-topaz and quartz-mica, the infiltrating fluid should have a low pH value (<3.2) and a low F concentration (<0.015 mol/kg). However, if the infiltrating fluid is acidic (pH <5.8) and enriched in F (>0.015 mol/kg), mica-free greisen will form. For sequential quartz-mica and quartz-topaz greisen formation, a Cl-dominated fluid is likely, whereas for the formation of quartz-topaz greisen alone, F likely dominates the fluid. Since chlorine and fluorine tend to form different metal complexes in aqueous fluids, the variable fluid compositions during greisenization may be important for the development of different mineralization processes that occur during quartz-topaz and quartz-mica greisenization.

Key Words: Quartz-Topaz greisen; Quartz-Mica greisen; F; pH; Porosity

4.1. Introduction

Fluid-rock interaction is an important process for many petrophysical and geochemical changes in the Earth's crust. In this context, metasomatic processes are the most important factor leading to chemical changes in crustal rocks due to the composition and amount of aqueous fluids interacting with the respective rocks, and these interacting fluids often have magmatic origins. One specific type of hydrothermal alteration on typically felsic rock such as granitic or rhyolitic rock, thus resulting in metasomatism, is called greisenization. Greisenization is economically interesting due to its relation to important Sn-W deposits (Table 4.1), like the Zinnwald/Cínovec Li-Sn-W deposit, Sadisdorf Li-Sn-(W-Cu) deposit, the Maoping W-Sn-polymetallic deposit, the Beauvoir W-polymetallic deposit, and the Panasqueira W-Sn deposit (e.g., Breiter et al., 2017a; Korges et a., 2018; Monnier et al., 2019; Launay et al., 2021; Ni et al., 2023; Leopardi et al., 2024). Greisen can be classified by major mineral composition, with quartz-mica, quartz-topaz, and quartz-mica-topaz greisen (Fig. 4.1 a) being the most common types (e.g., Štemprok, 1987).

Greisen-type alteration is characterized by the breakdown of feldspars and biotite, mostly to Al-rich mica, topaz, and quartz, with the concomitant changes in whole rock chemical composition (e.g., Shcherba, 1970; Štemprok, 1987). The diversity in greisen mineralogy, e.g., quartz-mica greisen or quartz-topaz greisen, may reflect differences in formation conditions. Massive quartz-mica greisen formations are typically reported in connection with W-Sn ore deposits (e.g., Breiter et al., 2017b; Korges et al., 2018; Launay et al., 2019; Monnier et al., 2019). Compared with quartz-mica greisen, quartz-topaz greisen is less commonly described, but it contains large proportions of topaz (Soloviev et al., 2020; Qiao et al., 2024). Quartz-topaz greisen often occurs in the inner part of greisen complexes and is often separated from the wall rock by quartz-mica greisen (Halter et al., 1998; Shapovalov and Setkova, 2012), but quartz-topaz greisen veins may also occur in distal parts of a greisen complex (Qiao et al., 2024). Yet, in Kougarok, quartz-topaz greisen is in immediate contact with chlorite schist and is not separated by quartz-mica greisen (Soloviev et al., 2020). P-T conditions generally play an important role in most hydrothermal interactions (Mikucki, 1998; Sillitoe, 2010). Greisen formation takes place in the apical contact zone or the envelope of acidic (leuco) granitic intrusions at shallow levels (< ~4 km) and at ~200–450 °C during the post-magmatic hydrothermal stage (Fig. 4.1 b). For example, an investigation of the fluid inclusions in Beauvoir greisen showed that the greisen fluid originated from a very shallow magmatic source (Monnier et al., 2020). In that the East Kemptville tin deposit, single greisenization event was able to form both quartz-topaz greisen and quartz-mica greisen at ~450 °C (Halter et al., 1995). Overall, the depths and temperatures found in earlier studies suggest that quartz-topaz greisen and quartz-mica greisen form at similar rather low P-T conditions.

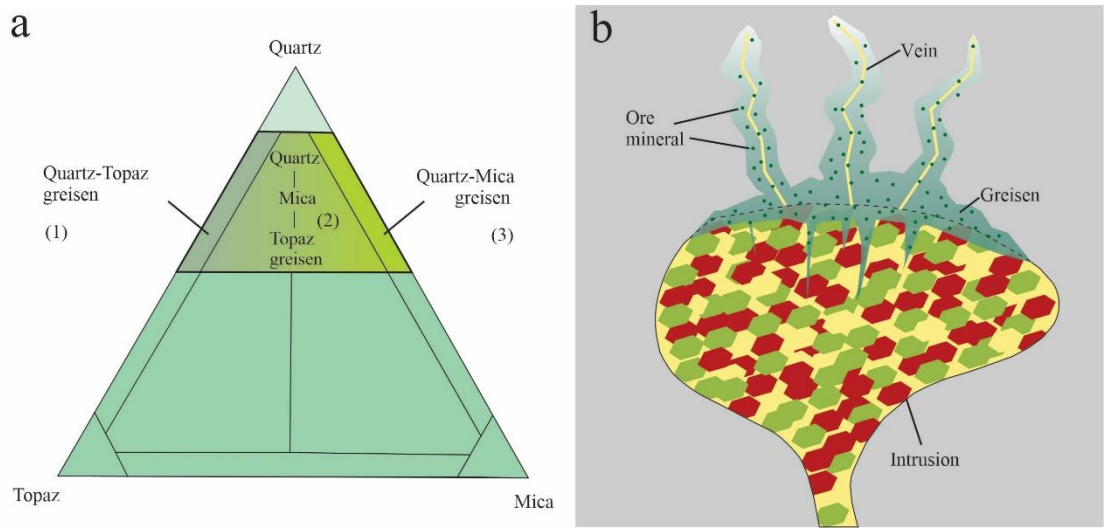

Fig. 4.1. (a) Diagram of greisen classification by mineral abundance ratios of topaz, mica, and quartz (modified after Kühne et al., 1972) and (b) schematic illustration of a greisen-forming system. In nature, quartz-topaz (1) and quartz-mica (3) greisen predominate. Greisenization normally takes place along the contact zone between the intrusion and wall rock as well as the area along the fractures. The grey background represents the wall rock, and the intrusion here typically refers to granitic rocks. The dashed line represents the boundary of intrusion and wall rock.

In all of these cases, the host rocks are felsic without significant difference in bulk chemistry. Therefore, the greisen fluids may be responsible for the diversity of greisen mineralogy. Greisen fluids derived from highly differentiated granitic systems are enriched in volatiles including Cl, F, etc. (Webster et al., 2004; Breiter et al., 2019; Launay et al., 2021; Leopardi et al., 2024). Numerous studies have proposed that Cl^- is an important component of the greisenization process, because chloride complexes are known to mobilize some metals, including W, Sn, REEs, etc. (Heinrich, 1990; Halter et al., 1996; Zajacz et al., 2008; Migdisov et al., 2016; Korges et al., 2018). A daughter mineral study of fluid inclusions found large proportions of halite, sylvite, calcium chloride, and other chloride minerals, suggesting that many cations in greisen fluids transported as chloride complexes (Witt, 1988; Leopardi et al., 2024). Notably, the fluid that reacts with wall rock to form greisen is always acidic (Burt, 1981; Štemprok, 1987). In nature, the dominant acid species is HCl (Burt, 1981), the dissociation of which controls the pH value change of greisen fluid. In the process of greisenization, feldspar and biotite are replaced by quartz-mica-others, and this process consumes H^+ (Lecumberri-Sanchez et al., 2017; Launay et al., 2021), thus working to neutralize the fluid. However, other processes might increase fluid acidity, like boiling and cooling (Burt, 1981). Overall, the pH evolution of the greisen fluid as well as the chlorine content is key to the mineralization process during greisenization.

Table 4.1. Different greisen types and their related ore deposits

Type	Example	Mineralogy	Host rock	Ores	Reference
Quartz Topaz (1)	East Kemptville (Canada)	quartz+topaz+ fluorite ±muscovite	leucogranite	pyrrhotite sphalerite chalcopyritecassiterite	Halter et al., 1995
	Kougarok (USA)	quartz+topaz +fluorite	zinnwaldite granite schist	cassiterite wolframite Ta-Nb- mineral	Soloviev et al., 2020
Quartz Mica Topaz (2)	East Kemptville (Canada)	quartz+sericite +topaz+fluorite	leucogranite	Sphalerite pyrrhotite chalcopyrite	Halter et al., 1995
	Maoping (China)	quartz+mica +topaz+fluorite	mica granite sandstone	cassiterite wolframite	Chen et al., 2019
Quartz Mica (3)	Kougarok (USA)	quartz+ muscovite +tourmaline	zinnwaldite granite schist	cassiterite wolframite Ta-Nb- mineral	Soloviev et al., 2020
	Panasqueira (Portugal)	quartz+ muscovite	two-mica granite	cassiterite wolframite columbo-tantalite sulfides	Launay et al., 2021
	Zinnwald/Cínovec (Germany, Czech Republic)	quartz+ zinnwaldite ±topaz	zinnwaldite granite	wolframite cassiterite zinnwaldite	Breiter et al. 2017a
	Beauvoir (France)	quartz+ muscovite ±apatite	granite	wolframite cassiterite	Monnier et al., 2019

As described by Webster et al. (2004), the greisen fluid in the Zinnwald region was found to contain F in amounts equal to or larger than those of Cl. During the development of quartz-topaz greisen, large amounts of F are required to allow topaz to precipitate in large quantity. Further, as highlighted by Marignac and Cuney (1991), for the formation of a W-Sn ore deposit to be attributed to a Cl-rich fluid, a large volume of igneous intrusion would be required, but this contradicts the small size of the granitic intrusions that are associated with W-Sn ore bodies (Webster et al., 2004). These observations suggest that a Cl-rich fluid might not dominate its formation. In addition, greisen has been found to display significant deviations from chondritic values in Zr/Hf and Ho/Y ratios, which, coupled with the fact that fluorine can form different complexes with Zr, Hf, Y, and Ho, suggests that fluorine is an important complex ligand in greisen fluid and, thus, may lead to the fractionation of these geological twin elements (Loges et al., 2013, 2024). Therefore, the initial fluid composition including Cl, F content and pH value and the processes at play in greisenization influence the fluid's acidity and complexation potential,

which are critical for the mobilization and demobilization of ore metals (e.g., Heinrich, 1990; Wang et al., 2021).

Although numerous studies on greisen exist, we still do not entirely understand the chemical and mineralogical development of the fluid-rock system during greisenization. Further, we only poorly understand quantitatively how the resulting greisen is influenced by various parameters of the original fluid, such as pH value and fluoride content. In addition, although that understanding porosity is key to quantitatively describing ore formation processes (e.g., Weis, 2015; Launay et al., 2019), this aspect of greisen formation has been insufficiently studied (e.g., Qiao et al., 2024). Thus, to investigate how the initial F concentration and pH value of the infiltrating fluid influence the emergence of porosity and the mineralogical development during formation of a range of common greisen types and zonation patterns, in this study we developed a reactive transport model to simulate the process of greisenization.

4.2. Methods

4.2.1. Equations and solution strategy

The reactive transport model is based on continuity equations describing balance of mass, momentum, and concentrations of HF and HCl in the fluid. A numerical solution can be obtained using an explicit finite difference scheme (Beinlich et al. 2020; Vrijmoed and Podladchikov, 2022). As we focused on the chemical changes due to reaction in a multicomponent system, we assumed for simplicity a constant Darcy flux and no solid deformation by setting the velocity of a solid to zero. The following partial differential equations describe the reactive transport in the model:

$$\frac{\partial C_{tot}^{HF}}{\partial t} = \nabla \cdot \left(\rho_f \phi D_f^{HF} \nabla C_f^{HF}\right) - \nabla \cdot \left(\rho_f C_f^{HF} q_D\right)$$

$$\frac{\partial C_{tot}^{HCl}}{\partial t} = \nabla \cdot \left(\rho_f \phi D_f^{HCl} \nabla C_f^{HCl}\right) - \nabla \cdot \left(\rho_f C_f^{HCl} q_D\right)$$

Where:

$$C_{tot}^{HF} = \rho_f \phi C_f^{HF} + (1-\phi)\rho_s C_s^{HF}$$

Porosity evolution is obtained from the time-integrated mass balance of an immobile component (e.g., Malvoisin et al. 2015):

$$\emptyset = 1 - \frac{(1-\varphi^0)\rho_s^0 C_s^{\Im 0}}{\rho_s C_s^{\Im}}$$

These three equations are solved for the total mass of HF and HCl (C_{tot}^{HF} and C_{tot}^{HCl}) and porosity (ø). We obtained the density of fluid and solid (ρ_f and ρ_s), the HF and HCl content of fluid (C_f^{HF} and C_f^{HCl}), and immobile element content of the solid (C_s^{im}) from interpolation of precomputed equilibrium thermodynamic lookup tables based on the assumption of local equilibrium. The diffusivity of the mobile phase and Darcy flux, namely D_f, and q_D, respectively, are held constant in the simulation. The superscript 0 indicates the initial value of the variables.

Given that quartz occurs in all mineral assemblages, we did not include aqueous silica (SiO_2) in the calculation. In addition to the reactive transport species, we consider other aqueous species in the Gibbs minimization, including HF, HCl, NaCl, KCl, H^+, F^-, Cl^-, Na^+, and K^+, with additional Al- and Si- species calculated retrospectively for monitoring during the simulations. These aqueous species were selected based on equilibrium thermodynamic calculations that showed the dominant species in the fluid (Fig. 4.2). We concluded that Al species were negligible in the fluid system considered here, such that this element was considered immobile. This conclusion is consistent with mass balance calculations from Qiao et al., (2024).

4.2.2. Equilibrium thermodynamics

The transport equations are coupled to reactions by using a local equilibrium approach in which thermodynamic calculations are precomputed and stored in lookup tables. This approach has been used successfully in the past, as it conveniently handles multicomponent systems with complex solution models (e.g., Malvoisin et al, 2015, Plümper et al. 2017, Beinlich et al. 2020; Huber et al., 2022). We formulated the reactive transport model in MATLAB and used Thermolab (Vrijmoed and Podladchikov, 2022) to calculate thermodynamic equilibrium to prepare the lookup tables. The calculations were done in the system Si-Al-K-Na-F-Cl-H-O, and the pure phases quartz, microcline, albite, muscovite, andalusite, sylvite, halite, and corundum from the Holland and Powell (1998) dataset (version tc-ds55) were combined with a fluid phase. The fluid system was treated as a non-ideal dilute electrolyte solution containing the species (e.g. Dolejš and Wagner, 2008), HCl, NaCl, KCl, Na^+, K^+, Cl^-, H^+, and OH^- using the dataset from Miron et al. (2016), with the exception of HF and F^-, which were taken from the SUPCRT dataset (Johnson et al., 1992). As topaz does not occur in any of the mentioned datasets, we used the topaz and hydroxyl-topaz endmembers from Barton (1982) to the dataset in Thermolab. Additionally, we tested the modifications of the Barton (1982) topaz enthalpy as studied by Dolejš and Baker (2004) for our equilibrium calculations. Topaz was considered to be a solid solution of fluorine-

and hydroxyl-topaz (Barton, 1982), which is consistent with natural topaz (Pinheiro et al., 2002; Loges et al., 2022). A P-T benchmark diagram was made to ensure consistency of the added topaz solid solution with experiments (Fig. 4 A1).

Here we investigated a ternary subsystem, where we varied the bulk composition of HCl, HF, and H_2O while keeping all other elements constant. Equilibrium was obtained by Gibbs minimization using a linear programming approach, as has been proven useful (e.g., Vrijmoed and Podladchikov, 2022; Connolly, 2005, 2009). By studying the effect of adding different amounts of the system components, we found a suitable corner of composition space in which most of the observed mineral reactions were found.

In the ternary system, only two independent bulk compositions were varied between 0 and 1 mol, namely the components HCl and HF, whereas H_2O was determined such that the sum of the components added up to 1. These varying molar amounts were added on top of a fixed amount of the components NaCl, KCl, K_2O, Na_2O, microcline, albite, quartz, and water. Based on the minimization of Gibbs energy of different phases in the system under 320 °C and 10^8 Pa, we obtained phase diagrams that show the stable mineral assemblage and the corresponding fluid in equilibrium. The Gibbs minimization result was taken as a first guess for the stable phase assemblage and fluid composition, which was then further refined using the method by Crerar (1975) to solve for speciation in the fluid in equilibrium with a solid phase assemblage, as is commonly done in aqueous geochemistry (Bethke, 2005).

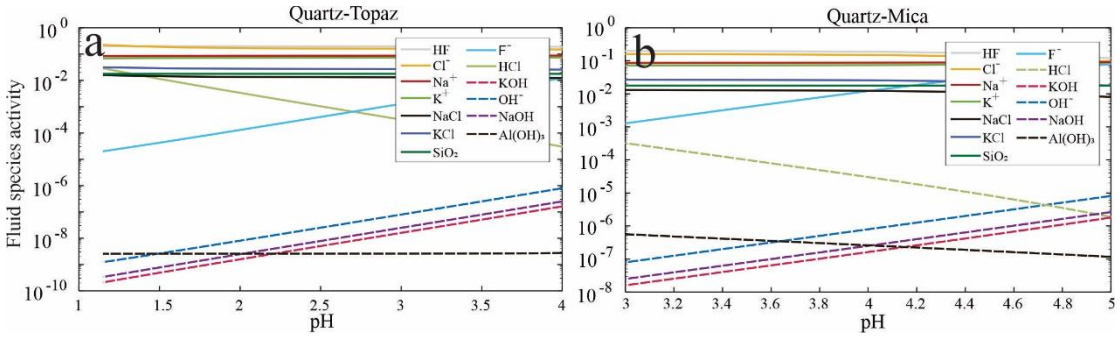

Fig. 4.2. The dominant fluid species in equilibrium with (a) quartz-topaz and (b) quartz-mica assemblage. The diagram shows which main fluid species are most important to take into account for the discretization of the fluid compositions used in linear programming for the stable phase calculation (e.g. the Gibbs energy minimization).

4.2.3. Model setup

The petrological and mineralogic work on the Zinnwald/Cínovec Sn-W-Li deposit has shown that next to the well-studied massive quartz-mica greisen (Breiter et al., 2017a), there exists in the distal part of the zinnwaldite granite a topaz-rich but mica-poor greisenization sequence (Qiao et al., 2024). Comparing these two distinctive greisen types may suggest that the formation conditions of quartz-mica greisen and quartz-topaz greisen are different but likely linked.

To study the formation of different greisenization types, we set up a one-dimensional (1D) numerical simulation to investigate how the main components HF and HCl influence the interaction between F-bearing fluid and granitic rocks. The modeling domain is initialized with a fixed starting rock consisting of 32 vol.% albite, 31 vol.% K-feldspar, 31 vol.% quartz, and 6 vol.% mica, representing a wall rock rhyolite (Qiao et al., 2024). The left boundary of the domain represents a vein or fracture from which a fluid with a fixed composition flows into the rhyolite, producing reaction fronts from left to right (Table 4.2). The simulations revealed that the interplay between F content and pH during the reactive fluid flow control the formation of different greisen types. Additionally, we also investigated the effect of K and Na on the process of greisenization. Our calculations show that Na and K modify the size of the stability fields of albite and K-feldspar but the topology of the phase diagrams remains similar. High Na concentration in the fluid will promote the stability of albite, while high K concentrations are supportive to the formation of K-feldspar. Furthermore, the higher K concentrations that were used did not alter the stability field of strongly, but the more Na contents in the system decreased the size of the topaz-quartz stability field significantly (Fig. 4 A2). As the topology of the diagrams remain similar, we kept our focus in this study on the influence of pH value and F content for the greisenization.

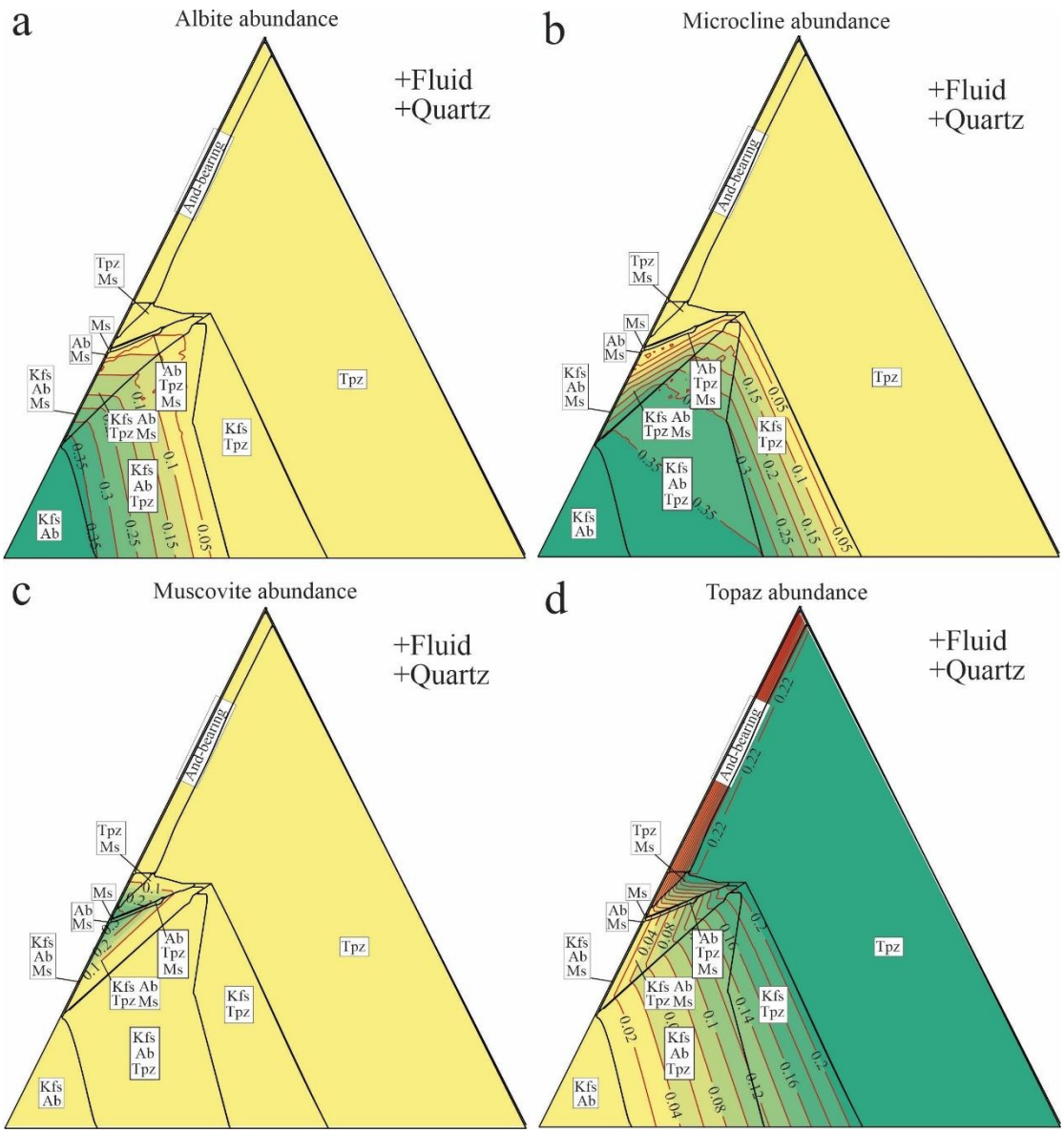

Fig. 4.3. Mineral abundance diagram of (a) albite, (b) microcline, (c) muscovite, and (d) topaz. The red contour line and the number represent the volume fraction. Mineral abundance ranges from low to high, represented by yellow to dark green, with intermediate colors indicating moderate levels. Ab: albite; And: andalusite; Kfs: K-feldspar; Ms: mica; Tpz: topaz.

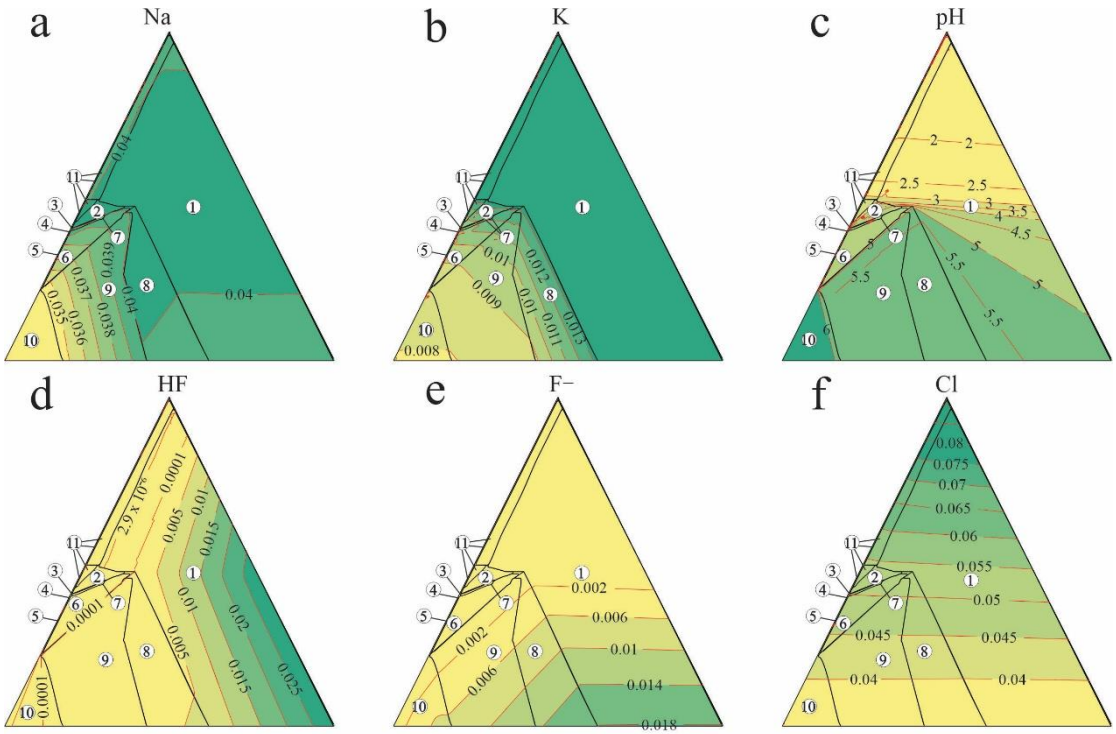

Fig. 4.4. Concentration of fluid components (mol/kg) equilibrated with the stable mineral assemblages. Na, K, and Cl represent the total concentration of the corresponding elements. The number represents the stable mineral assemblages. Values range from low to high, indicated by yellow to dark green, representing species concentration or pH levels. Ab: albite; And: andalusite; Kfs: K-feldspar; Ms: mica; Qtz: quartz; Tpz: topaz.

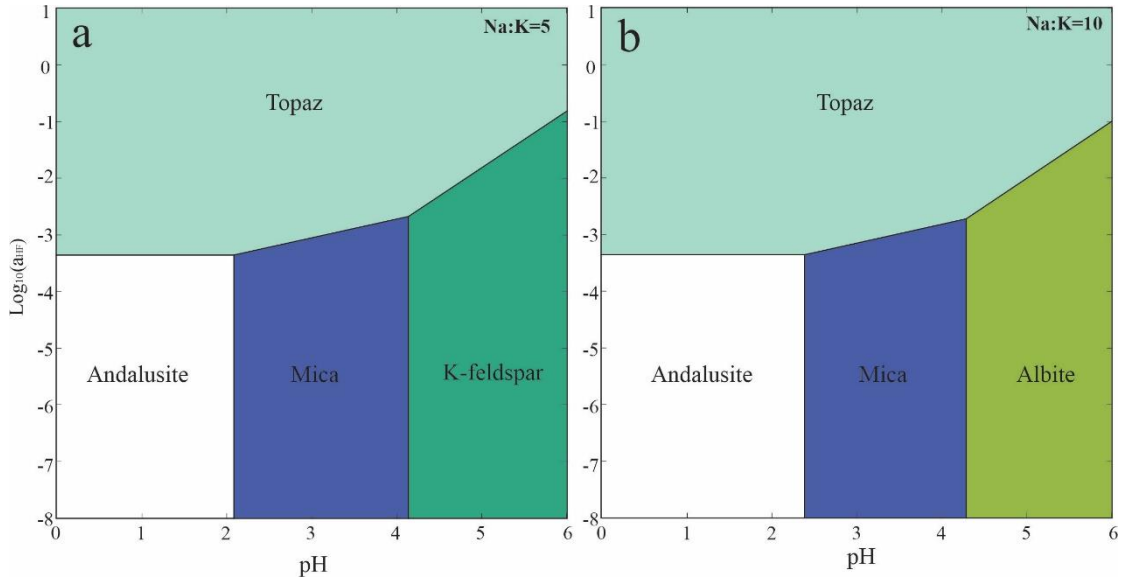

Fig. 4.5. Activity-pH diagrams showing the mineral stability fields at variable activity of HF and pH values calculated using chemical reactions and the equilibrium constant. Topaz is stable at high HF activity and a broad range of pH values, which indicates the high HF activity promotes the feldspar and mica replacement by topaz. Mica will replace felspar at low pH values. Additionally, andalusite is stable at low HF activity and pH values, andalusite will be replaced by other minerals by increasing activity of HF or pH values. Quartz is stable in all diagrams.

Table 4.2. Fluid composition setup

Run	Initial composition of infiltrating fluid			Initial composition of fluid in unaffected wall rock		
	pH	F (mol/kg)	Porosity (%)	pH	F (mol/kg)	Porosity (%)
a	3.3	5×10^{-5}	14.3	5.0	3.4×10^{-6}	0.5
b	3.3	4×10^{-4}	14.4	5.0	3.4×10^{-6}	0.5
c	2.0	0.012	14.5	5.0	3.4×10^{-6}	0.5
d	4.4	0.024	14.5	5.0	3.4×10^{-6}	0.5

4.3. Results

4.3.1. Dependence of mineral stabilities on the fluid composition

The phase diagrams (Fig. 4.3 and 4.4) show the stable phases at a given bulk composition. Each point in the phase diagram has a corresponding fluid composition in equilibrium with the solid (Fig. 4.3 and 4.4). In the stability field of feldspar, the concentration of alkaline elements (Na and K) in the corresponding fluid has an opposite trend compared to the abundance of albite and microcline in the

rock, with the fluid being richer in Na than K (Fig. 4.4). Interestingly, feldspar is not stable at pH values <4.8. The stability of muscovite is controlled by both the pH value and the HF concentration of the fluid. Muscovite is only stable under low HF concentration (< ~10^{-4} mol/kg), but it is not stable when the pH value is lower than 3.2 (Fig. 4.4 c, 4.4 d, 4.4 e and 4.5). Compared with muscovite, topaz is stable under a broader range of F concentrations ($HF+F^-$) and pH values. Quartz is always supersaturated. A narrow stability field of andalusite is found to occur in this system at low pH value (<3.4) and low HF concentrations (<2.9×10^{-6} mol/kg, Fig. 4.4 d). As andalusite is not a common mineral in naturally occurring greisen, this observation provides another constraint on the fluid compositions because it restricts the fluid composition to reasonably high HF concentrations (<2.9×10^{-6} mol/kg). Feldspars + quartz ± muscovite are always stable under less acidic conditions (pH >4.8). The stable muscovite-bearing assemblage is limited to a low F content (<10^{-4} mol/kg) and higher pH value (>3.2). compared to topaz-bearing assemblages (Fig. 4.3, 4.4 and 4.5), which are stable under a broad range of fluid conditions (F >2.9×10^{-6} mol/kg, pH <5.8).

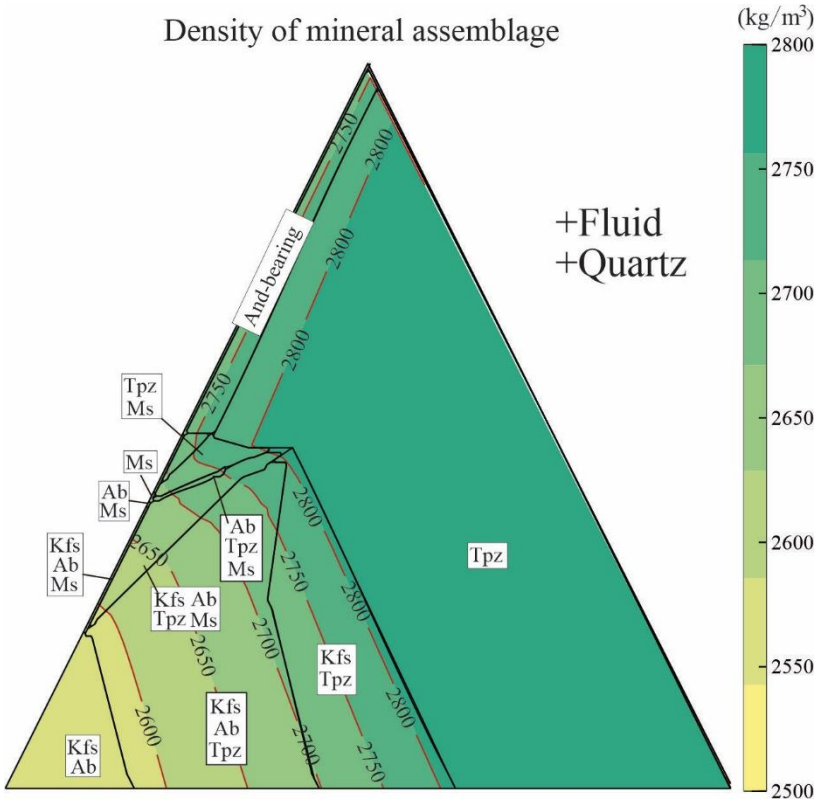

Fig. 4.6. Density (kg/m^3) diagram of bulk mineral assemblage. The topaz-bearing assemblage possesses a higher bulk density, whereas the feldspar-bearing assemblage has a lower density. The dashed line and the number represent the density of the corresponding bulk mineral assemblage. Ab: albite; And: andalusite; Kfs: K-feldspar; Ms: mica; Tpz: topaz.

4.3.2. Development of mineral assemblage, porosity, fluid composition under different initial conditions

During greisenization, the density of the developing mineral assemblage changes (excluding the fluid for simplicity) (Fig. 4.6). Our simulations reveal how the density increases while the different types of greisen develop. As textural observations on natural greisen show, greisenization is basically a replacement process during which the overall rock texture is preserved (e.g., Launay et al., 2019; Qiao et al., 2024). This indicates that the observed densification of the bulk solid can be attributed to the formation of pores, because rock deformation (volume strain) such as compaction can be neglected (e.g., Plümper et al., 2017; Beinlich et al., 2020). The matrix has a very low initial porosity set to 0.5 %, which reflects typical values for dense magmatic rocks such as granites and rhyolites (Launay et al., 2019, and references therein), whereas the porosities for quartz-topaz greisen and quartz-mica greisen are 14 % and 8 % (Fig. 4.7), respectively. At the beginning, the fluid in the pores of the matrix has a low concentration of F (3.4×10^{-6} mol/kg) and a high pH value (pH = 5), but the incoming fluid has a higher F content and a lower pH value (Table 4.2); this agrees with the conceptual view of the greisen-forming fluid (Burt, 1981; Halter et al., 1998). In the simulation, we made several runs with different initial compositions of the incoming fluid but the same starting wall rock composition (Fig. 4.8). These runs with different F concentrations and pH values developed quite distinctive sequences of greisen (Fig. 4.9).

Runs with similar pH values of 3.3 but different initial F concentrations lead to sequences with different ratios of the width of quartz-topaz greisen vs. quartz-mica greisen (Table 4.2, Fig. 4.9). Fluids with a lower F content (5×10^{-5} mol/kg) lead to a narrow quartz-topaz greisen zone but a large quartz-mica greisen zone, whereby the ratio of their respective widths is 0.1 (Fig. 4.9 a). By contrast, fluids with high F content (4×10^{-4} mol/kg) result in a wider quartz-topaz greisen but a narrow quartz-mica greisen, with a corresponding width ratio of 1.3 (Fig. 4.9 b). For an incoming fluid characterized by high F content (≥0.01 mol/kg), almost no mica forms, but a wide quartz-topaz greisen zone develops (Fig. 4.9 c and d). This observation differs from what is mostly described as being the general sequence of greisen (Štemprok, 1987), which tends to include a zone of mica-bearing assemblage. Due to the local equilibrium in the solid-fluid system, the quartz-topaz greisen always has a higher F content than all other zones; the quartz-mica greisen and the initial wall rock have similar low F concentrations (Fig. 4.9 a and b).

4.4. Discussion

4.4.1. Influence of the fluid composition on greisen formation

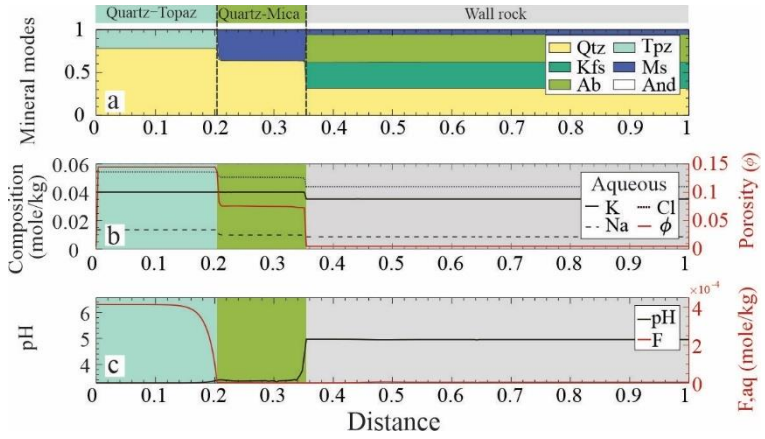

Fig. 4.7. Simulation (run b) for chemical evolution of the fluid during greisenization. (a) Profile of mineral modes, (b) Aqueous species concentration and porosity, (c) pH and F content of fluid. On the x-axis, *Distance* refers to the distance to the fracture. Ab: albite; And: andalusite; Kfs: K-feldspar; Ms: mica; Qtz: quartz; Tpz: topaz.

4.4.1.1 Fluid evolution during greisenization

Fluid evolution during the fluid-rock interaction is an important factor in the understanding of greisen formation. Here we take a closer look at the case with quartz-topaz and quartz-mica greisen as an example (Fig. 4.7 a). The quartz-topaz greisen zone, the quartz-mica greisen zone, and the wall rock have quite different equilibrium fluid compositions (Fig. 4.7 b). During the initial stage, the fluid that reacts with the wall rock forms a quartz-topaz greisen. The fluid in equilibrium with such a quartz-topaz assemblage has a relatively high F concentration (4×10^{-4} mol/kg, Fig. 4.7 b). During this stage of greisenization, feldspar and mica are replaced by topaz and quartz (equation 1–3) and Na and K are released into the fluid. This results in a fluid enriched in alkali element cations (Fig. 4.7 b).

$$2\ KAl_3Si_3O_{10}(OH)_2 + 6\ HF + 2\ H^+ = 3\ Al_2SiO_4F_2 + 2\ K^+ + 3\ SiO_2 + 6\ H_2O \quad (1)$$

$$2\ KAlSi_3O_8 + 2\ HF + 2\ H^+ = Al_2SiO_4F_2 + 5\ SiO_2 + 2H_2O + 2\ K^+ \quad (2)$$

$$2\ NaAlSi_3O_8 + 2\ HF + 2\ H^+ = Al_2SiO_4F_2 + 5\ SiO_2 + 2H_2O + 2\ Na^+ \quad (3)$$

$$3\ NaAlSi_3O_8 + K^+ + 2H^+ = KAlSi_3O_{10}(OH)_2 + 6SiO_2 + 3Na^+ \quad (4)$$

$$3\ KAlSi_3O_8 + H^+ = KAlSi_3O_{10}(OH)_2 + 6SiO_2 + 2\ K^+ \quad (5)$$

Compared to the quartz-topaz greisen zone, the fluid in equilibrium with the quartz-mica greisen is characterized by a lower F content (10^{-6} mol/kg, Fig. 4.7 c). In this zone, feldspar is also replaced by mica and quartz (equation 4–5). The pH value in the quartz-mica zone (pH = 3.3–3.7) is similar to that of the quartz-topaz zone (pH = 3.3). Therefore, fluid in equilibrium with greisen may generally be characterized by low pH values (and relatively high F concentrations in the quartz-topaz greisen zone of 4×10^{-4} mol/kg), matching the findings in natural greisen (Štemprok, 1987; Halter et al., 1996, 1998; Monnier et al., 2019; Launay et al., 2021; Qiao et al., 2024). Thus, the main difference between quartz-topaz greisen and quartz-mica greisen is the F concentration of the infiltrating fluid.

4.4.1.2 The effect of F concentrations and pH values on the greisen assemblage.

Although greisenization is generally an alteration of felsic rocks with similar mineral composition, like granites, rhyolite, gneiss, and schist (Breiter et al., 2017b; Peterková and Dolejš, 2019; Launay et al., 2019, 2021; Monnier et al., 2019, 2022; Qiao et al., 2024), the resulting greisen may have significantly different proportions of mica and topaz. Because the composition of the starting material is very similar, the potential differences in the composition of the greisen-forming fluid is likely the cause of the variability that is observed in natural greisen (e.g., Halter et al., 1998). The 1D numerical simulations in this study show that the initial F concentration of the incoming fluid has a large influence on the mineral assemblages and reaction zone sequences that develop, especially regarding the relative widths of the quartz-mica and quartz-topaz zones (Fig. 4.9). At similar pH values (pH = 3.3), F-rich fluid ($\geq 4\times10^{-4}$ mol/kg) supports a wider topaz-rich zone (Fig. 4.9 b), whereas lower F concentrations ($\leq 5\times10^{-5}$ mol/kg) lead to mica-rich greisen (Fig. 4.9 a). In these two cases, NaCl is the dominant species in the fluid, and pH values (3.3 and 3.4, respectively) remain almost constant in the greisen.

Comparing these two simulations (Fig. 4.9 a and b), we see that although their F concentrations are both very low (5×10^{-5} and 4×10^{-4} mol/kg, respectively), the simulation with higher F concentration (4×10^{-4} mol/kg) still results in a larger width of the quartz-topaz greisen zone (Fig. 4.9 b). Burt (1981) suggested that at increasing μ_{HF}, topaz should replace muscovite. Halter et al. (1998) also experimentally produced a profile of quartz-topaz greisen by increasing HF concentration in aqueous fluid by titration. These examples suggest that F may depress the formation of mica during greisenization. In the profiles of our simulations (Fig. 4.9 a and b), quartz-topaz and quartz-mica zone both have lower pH values (3.3–3.4) than the fluid in equilibrium with the original rock (pH = 5). However, the large zone of quartz-mica greisen in Fig. 4.9 a corresponds to low HF concentration (5×10^{-5} mol/kg), whereas the large quartz-topaz zone in Fig. 4.9 b requires a higher influx of fluorine (4×10^{-4} mol/kg).

For cases of pH < ~3.4, it turns out that if the F concentration is too low (<2.9×10^{-6} mol/kg), the fluid-rock interaction would result in the formation of andalusite (Fig. 4.4 d and 4.5), which is not described as a stable phase in the greisen literature. It is rather a typical contact metamorphic phase. We therefore conclude that fluids forming greisen under conditions similar to the ones simulated here typically have F concentrations above 2.9×10^{-6} mol/kg. These observations show that different F concentrations in greisen-forming fluids may be the most important contributor to the mineralogical variation of greisen observed in nature.

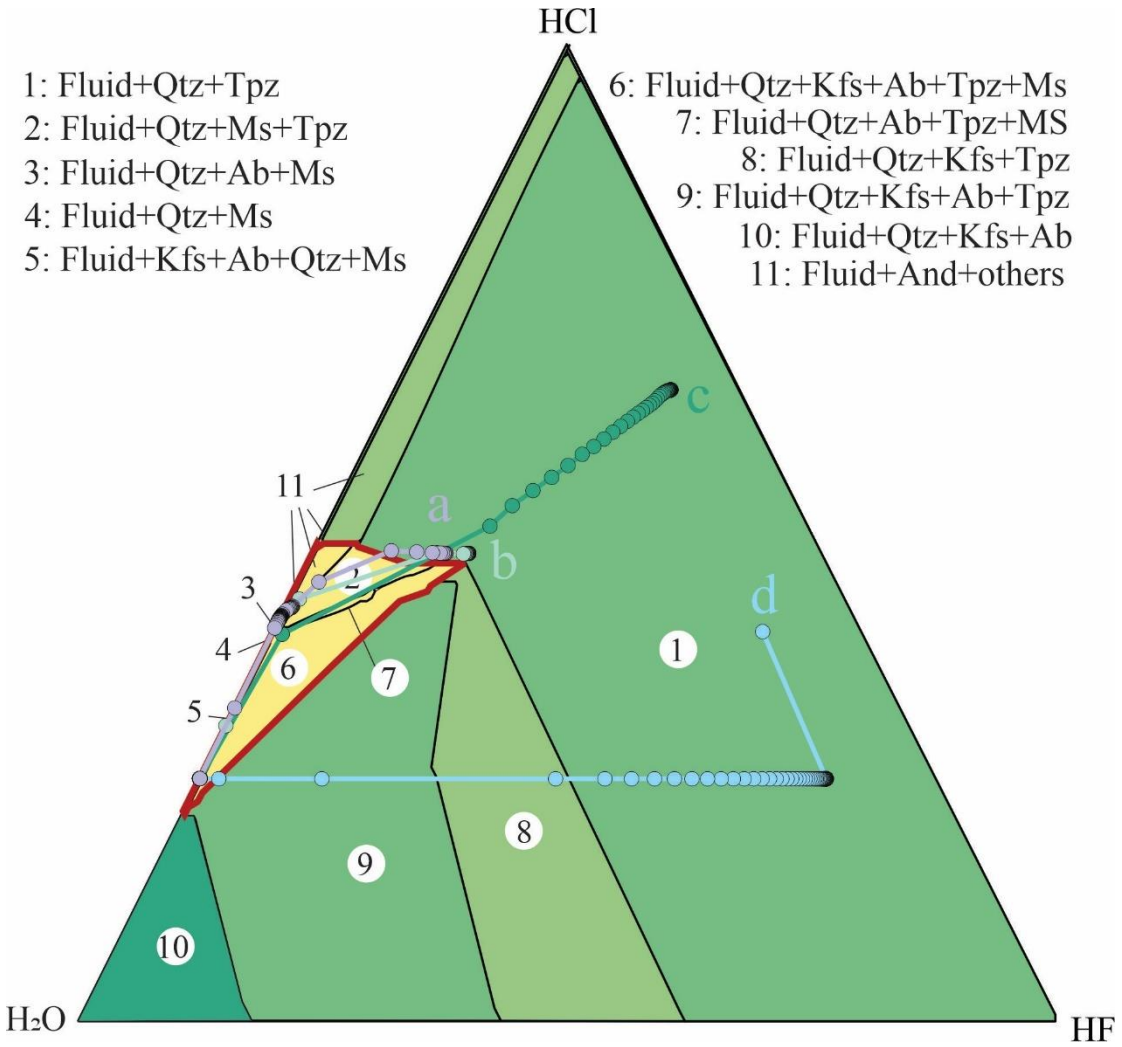

Fig. 4.8. Phase diagram with variable system composition of H_2O, HF, and HCl in addition to a fixed content of Si, Al, K, Na, Cl, and H_2O. Labeled areas correspond to different stable mineral phase assemblages. The colored paths are retrieved from the reactive transport model and show the bulk composition variation along an infiltrating fluid into a rhyolitic wall rock at a fixed point in time during the process. Different color paths are assigned to different incoming fluid compositions (a-d), whereas all paths share the same background (or initial) rock mineral compositions (host rock). This

demonstrates that subtle variations in incoming fluid composition give rise to distinctly different metasomatic zoning sequences. The reddish bold frame marks the mica-bearing field. Ab: albite; And: andalusite; Kfs: K-feldspar; Ms: mica; Qtz: quartz; Tpz: topaz.

In these simulations (Fig. 4.9 a and b), the F content in the fluids varies but at a low concentration (10^{-5}–10^{-4} mol/kg). These small variations still result in different patterns of greisen, with both patterns representing the entire "normal greisen sequence" as described in Štemprok. (1987). We previously investigated a greisen profile in the distal part of the Zinnwald/Cínovec Li-Sn-W deposit that contains a substantial quartz-topaz zone (Qiao et al., 2024). In this example, a narrow quartz-mica zone is present between the quartz-topaz zone and the host rock, and considerable feldspar is still left in this zone (Fig. 4.10 a). Given that this narrow quartz-mica zone developed in this distal region, while the greater Zinnwald/Cínovec deposit also contains a massive quartz-mica greisen, the question arises what conditions are necessary to form quartz-mica greisen. Simulations in Fig. 4.9 c and d present the interactions of the host rock with an incoming fluid having a high aqueous HF concentration (Table 4.2). The simulation in Fig. 4.9 c creates a profile very similar to that observed in natural rhyolite-hosted greisen veins from Zinnwald/Cínovec (Qiao et al., 2024), in that it shows only a small and restrictively developed quartz-mica zone (Fig. 4.10). This suggests that the formation of quartz-mica could be depressed by a high F concentration. Furthermore, in the simulation with 0.024 mol/kg of F in the fluid, a mica-free greisen demonstrates that mica is not a universally present phase in greisen (Fig. 4.9 d). These cases highlight that the F content of the aqueous fluid is the key factor controlling the relative extent of quartz-mica and quartz-topaz greisenization.

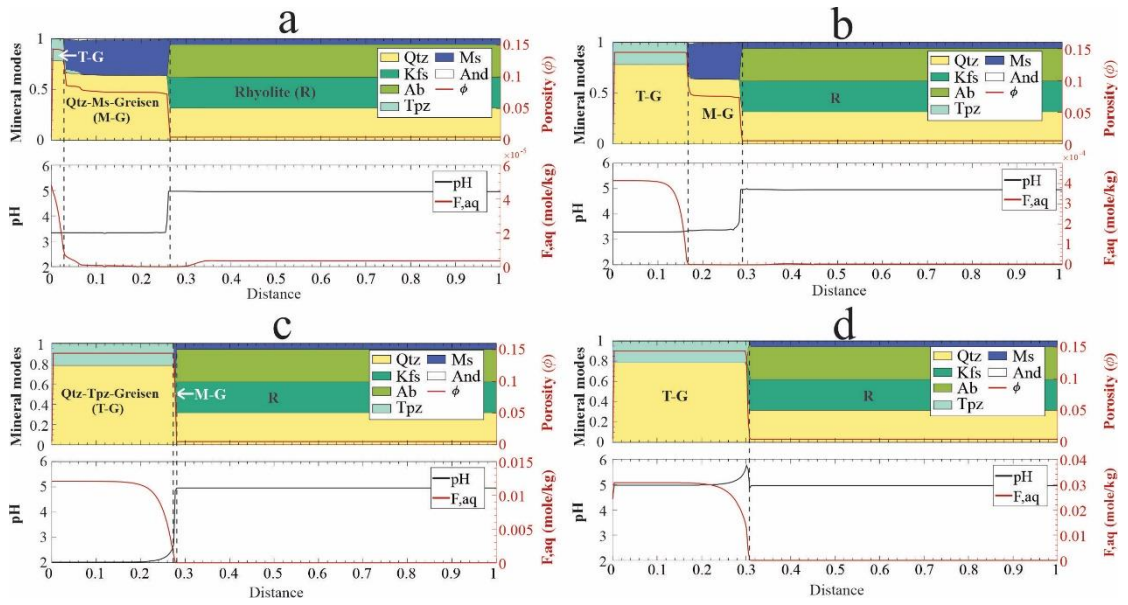

Fig. 4.9. Results of numerical simulations of greisen formation from the reactive transport model. Mineral area colored plots display mineral mode abundances along a 1D transect after some time of fluid infiltration from the left boundary toward the wall rock on the right. The blue and red curves in the plots show fluid composition (pH and F concentration) along the 1D profile during the simulations. The bulk system evolution paths of these interactions are presented in Fig. 4.8. Runs ***a*** and ***b*** show differences in the width of mica and topaz greisen zones. Runs ***c*** and ***d*** show the different modes of quartz-mica greisen and quartz-topaz greisen with different F contents and pH values of the incoming fluid. Ab: albite; And: andalusite; Kfs: K-feldspar; Ms: mica; Qtz: quartz; Tpz: topaz.

Another important factor controlling the variability in greisenization is the pH value of the related aqueous fluid. Comparing quartz-topaz greisen with quartz-mica greisen, higher pH values (in this case, pH >3.2) promote the formation of wider quartz-mica greisen (Fig. 4.11). The quartz-topaz assemblage equilibrates with an aqueous fluid of a pH value lower than 5.8, and the mica-bearing assemblage equilibrates with an aqueous fluid characterized by a smaller pH values range of 3.2–4.9, indicating that the pH value is also a key variable influencing whether quartz-topaz and quartz-mica greisen form (Fig. 4.11a).

In summary, together the F concentration and pH value of the infiltrating fluid control the variation (and its extent) observed in greisen. From our study, we can conclude the following: (i) The formation of quartz-topaz greisen requires a pH value below 5.8 but allows F concentrations above ~2.9×10^{-6} mol/kg. A high concentration of F (under the bold black line in the topaz-quartz field of Fig. 4.11) will cause the formation of mica-free greisen. (ii) An infiltrating fluid with an F concentration as low as ~2.9×10^{-6} mol/kg (above the bold black line in the topaz-quartz field of Fig. 4.11) will result in a quartz-topaz greisen zone as well as a quartz-mica zone having variable widths. However, at a pH value below 3.4, too low of F concentrations (< ~2.9×10^{-6} mol/kg) introduce andalusite as a stable phase, suggesting that fluid-rich contact metamorphism rather than greisenization will take place.

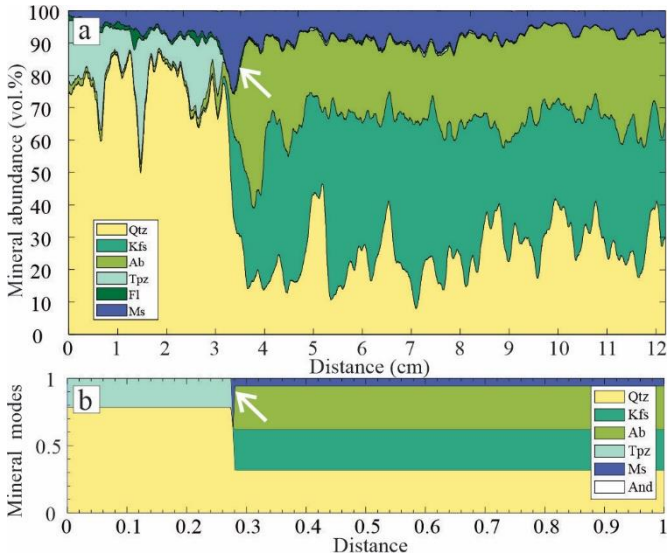

Fig. 4.10. Mineral mode profiles of greisen with a narrow quartz-mica zone. (a) Natural profile from the Zinnwald/Cínovec district (modified after Qiao et al., 2024), (b) Modeling profile similar to Fig. 4.9 c. For simplification, we do not consider fluorite in the modeling. Panels a and b are comparable given their large quartz-topaz zones and narrow quartz-mica zones, which suggests high aqueous F concentration in the fluid. The small quartz-mica zone is labeled by the white arrow on both panels. Ab: albite; And: andalusite; Kfs: K-feldspar; Ms: mica; Qtz: quartz; Tpz: topaz.

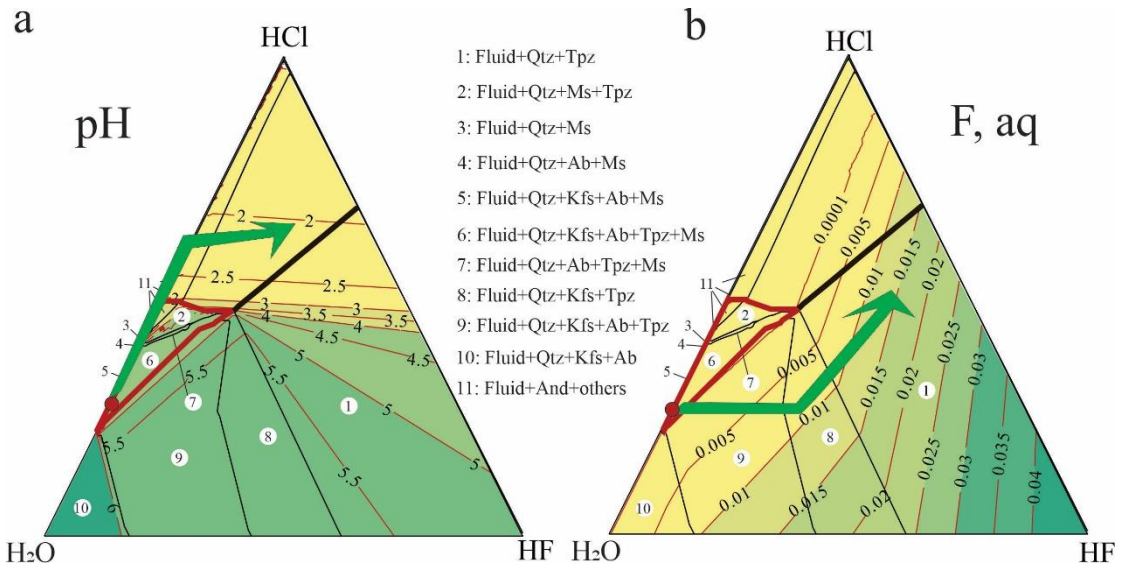

Fig. 4.11. Phase diagram with corresponding pH value (a) and total F content (b) of the equilibrium fluid. The arrow shows that the incoming fluid plays a different role in greisenization, depending on its pH and F concentration Above the bold line in the quartz-topaz field, the fluid's pH plays a dominant role that may control the formation of mica, whereas below the bold line, the F content of the incoming fluid depresses the formation of mica. The reddish bold frame marks the mica-bearing field. Values

range from low to high, indicated by yellow to dark green, representing pH or species concentration levels. Ab: albite; And: andalusite; Kfs: K-feldspar; Ms: mica; Qtz: quartz; Tpz: topaz.

4.4.1.3 The porosity evolution during greisenization

The porosity of the rock is crucial to allow fluid propagation into the wall rock. In our model, the host rock has a very low initial porosity (set to 0.5 %, see chapter 4.4.2). We found that greisenization significantly increases the porosity of the host rock to about 14 % for quartz-topaz greisen and to about 8 % for quartz-mica greisen (Fig. 4.9 a and b). In a petrophysical investigation, Launay et al. (2019) determined that the formation of muscovite greisen corresponds with a volume decrease of about 8.5 %, which is essentially identical to the results of our simulations. As this porosity is not permanent and will close during the metallization or final greisen formation process (e.g., Qiao et al., 2024), it must be considered a transient feature. The increase in dynamic porosity of more than one order of magnitude during fluid-rock interaction that we calculated is similar to slightly higher than of what other studies have suggested for the production of such transient porosity (John et al. 2012; Taetz et al., 2018; Beinlich et al., 2020).

Our finding of an almost twice as large porosity increase during quartz-topaz greisen formation compared to that during quartz-mica greisen formation indicates that quartz-topaz greisen is more efficient in allowing pervasive fluid-rock interaction (Fig. 4.9 a and 4.8 b). While the formation of both quartz-topaz greisen and quartz-mica greisen transiently increase the permeability of the host rock, the higher porosity in quartz-topaz greisen ensures that a large volume of fluid infiltrates the adjacent rock, such that the large volume of fluid from the quartz-topaz greisen zone may promote the formation of massive greisen bodies. Overall, the enhanced permeability conferred by this type of fluid-rock interaction contributes to the formation of large greisen-related deposits (Launay et al., 2019).

4.4.1.4 Influence of mica composition

In nature, the composition of white mica is more complex than that described in our model. For example, F is also a component of white mica. In the modeling, due to a lack of reliable consistent thermodynamic data on fluorine- and hydroxyl-muscovite solutions ($KAl_3Si_3O_{10}(F,OH)_2$), we simply employed the hydroxyl endmember ($KAl_3Si_3O_{10}(OH)_2$) to represent natural white mica (Holland and Powell, 1998). This could have influenced our finding that muscovite is not stable (and andalusite forms instead) if the pH value is too low (Fig. 4.5 and 4.11), since Govorov (1977) indicated that an assemblage of muscovite and quartz could be stable at pH <3. With a more complex mixing model for naturally occurring white mica, one might expect a larger stability field for mica, and andalusite would likely no longer form under

the given conditions. However, how exactly a more realistic mica solution model would influence the simulation of greisenization still needs to be investigated.

4.4.2. Comparison with natural greisen

With our modeling, we were able to reproduce the major greisen types, including Zinnwald/Cínovec greisen, Beauvoir greisen, and Kougarok Sn-Ta-Li prospect (Breiter et al., 2017a; Monnier et al., 2019; Soloviev et al., 2020; Leopardi et al., 2024). The spatial relationship of the greisen and related intrusions suggests that no obvious genetic relationship exists between greisenization and the affected host rock (Štemprok and Dolejš, 2010, and references therein). Natural greisen fluids always stem from an intrusion, and greisenization always occurs in the contact zone between the intrusion and the wall rock (Fig. 4.1 b). Thus, it is evident that the fractures in the apical part of the host rock control the spatial distribution of greisen (Breiter et al., 2017b; Štemprok and Dolejš, 2010; Leopardi et al., 2024).

The simulations (Fig. 4.9 a and b) with low F content in the fluid represent the complete sequence of potential greisen with a quartz-topaz and a quartz-mica zone, and, furthermore, our simulations show quartz-topaz greisen is spatially closer to the fluid source, whereas quartz-mica greisen is in immediately contact with the host rock. However, many reported greisen locations contain no known quartz-topaz zones (Breiter et al., 2017b; Launay et al., 2019, 2021; Monnier et al., 2019, 2022). According to our findings, possible reasons could include the following: (i) Spatially, the topaz-rich greisen is supposed to form narrow zones close to the vein or other fluid pathways around the contact zone between the intrusion and wall rock; therefore, the distribution of the topaz-rich greisen is always in the inner zone of the greisen system (Shapovalov and Setkova, 2012 and Fig. 4.1 b). By contrast, quartz-mica greisen is mostly observed in the outer part of this contact zone. Due to the relative spatial relationship, the quartz-mica is more frequently exposed at/near the surface or at a shallower depth than quartz-topaz greisen. (ii) Chemically, F-poor fluid reacting with the wall rock produces a very narrow topaz-rich zone and only a small amount of topaz (Fig. 4.9 a); thus, the distribution of a developing topaz-rich zone would be relatively localized and small in size. Our modeling reveals that these two reasons may explain why quartz-topaz zones in greisen are less typically found or even do not exist at all in some greisen complexes.

From the perspective of the metasomatic fluid's fluorine content, the most likely fluid source is highly evolved granitic magma (Dolejš and Baker, 2007; Leopardi et al., 2024, and references therein). These magmatic systems are known to exsolve volatile-rich (including Cl, F, CO_2, etc.) aqueous fluids during the late magmatic to hydrothermal transition. Even though the wall rock situation is often very similar, with almost the same bulk chemistry and mineral assemblage being affected by the fluid-rock

interaction, the development of different kinds of greisen indicates that the fluorine concentrations or the pH values of the initial fluid may show some variations during greisenization (Fig. 4.9).

To achieve the prerequisite F concentration that can result in the formation of quartz-topaz greisen, a process is needed that can increase the fluorine content as the greisen-forming fluid evolves. One option might be desiccation processes, during which the formation of hydrous minerals leads to an increase of the salinity of a fluid (Kusebauch et al., 2015; Scharrer et al., 2023); but, greisenization is not related to long-distance fluid flow required for this process to work efficiently. Boiling, however, frequently occurs during the late magmatic-hydrothermal phase of granitic intrusion emplacement (Burt, 1981; Nardi et al., 2012; Qiao et al., 2024), and during boiling HF preferentially fractionates into the vapor phase. In case of orthomagmatic fluids, this is always decompression boiling caused by rapid adiabatic ascent of the fluid through cracks or other preexisting pathways. Combining the insights from our modeling and findings from natural case studies, massive quartz-mica greisen deposits seem to indicate relatively F-poor fluids with moderately low pH values ($F < 0.0001$ mol/kg and $pH > 3.2$) under the P-T conditions we explored within this work (Fig. 4.11). In contrast, large quartz-topaz greisen zones indicate F-richer fluids (>0.0001 mol/kg).

4.4.3. Implications

Aqueous fluids are related to the formation of some of the most economically important element mobilization processes in the Earth's crust. The accompanying fluid-rock interaction processes can lead to far-reaching changes in mineral assemblages and in the porosity and permeability of the affected rocks through dissolution-precipitation reactions and rock densification or mass removal (Putnis, 2002; Putnis and John, 2010; Ruiz-Agudo et al., 2014; Beinlich et al., 2020); these changes can, in turn, result in economic ore mineralization (Smith et al., 2000; Sheard et al., 2012; Williams-Jones et al., 2012; Li et al., 2013).

Notably, our reactive transport model allowed us to quantitatively decipher the factors controlling the fluid-rock interactions. We found that differences in F concentration and pH of the infiltrating fluid result in the formation of different types of greisen (Fig. 4.9). Additionally, our results indicated that the physical properties of the affected rock change significantly (Fig. 4.6 and 4.9). Our modeling results revealed that porosity increases significantly during greisenization, which, in turn, enhances the ability of the system to undergo pervasive alteration of large rock volumes. This enhanced porosity is transient because the secondary minerals eventually clog the pore space when they form (e.g., Putnis and John, 2010; Beinlich et al. 2020; Qiao et al., 2024). Obviously, porosity changes during metasomatic fluid-rock interactions are crucial to allow for sufficient mass transport.

Ore mineralizations in greisen are critically controlled by the (partially transient) mineral stability during the process, as well as the changing fluid chemistry (concrete citations in the discussion below). Our model shows that both of these parameters are tightly linked (Fig. 4.11). To understand the significance of our findings for the understanding of ore formation in greisen, specifically Sn, W, and (to a lesser degree) Li ores, it is useful to first review how minerals control ore element mobility before discussing direct control of the ore elements by the fluid via aqueous speciation.

Most ore formation in greisen seems to be related to the quartz-mica type (Breiter et al., 2017b; Launay et al., 2019; Monnier et al., 2019; Peterková and Dolejš, 2019), whereas the significance of quartz-topaz greisen for ore formation is less well understood (Korges et al., 2018; Breiter et al., 2017b). From the perspective of the major rock-forming minerals, the relative abundance of mica and topaz can influence the budget of certain elements. Zinnwaldite in the Zinnwald/Cínovec Sn-W deposit is lithium rich (LiO_2: 2.0–4.4 wt. %, Breiter et al., 2019), which, in conjunction with the large total amount of zinnwaldite, makes lithium interesting as a mining metal, in addition the traditionally targeted tungsten and tin (Müller et al., 2018). Muscovite in the Beauvoir greisen is typically rich in tin (mean value: 1031 µg/g, Monnier et al., 2022), which may be because muscovite incorporated tin from the dissolution of cassiterite and lepidolite during the greisenization stage (Šemprok et al., 2005; Monnier et al., 2022); the Beauvoir greisen has indeed recorded processes in which cassiterite was replaced by muscovite (Monnier et al., 2019). Tungsten exhibits a different behavior than tin; hydrothermal muscovite is very low in tungsten compared to the mica in the host rock, which indicates that tungsten was leached out by the fluid during greisenization (Monnier et al., 2020, 2022). Overall, these cases indicate that the abundance of mica in greisenization is crucial for the enrichment and depletion of these elements.

In addition to the direct release and consumption of ore elements in the consumed or newly formed minerals, greisenization reactions also release other components that can indirectly control economically interesting mineralizations. For example, in Panasqueira, muscovitization of the iron-bearing host rock released iron, which promoted the precipitation of wolframite (Lecumberri-Sanchez et al., 2017).

As discussed above, fluid compositions, especially regarding pH, as well as F and Cl concentration, are different during quartz-topaz and quartz-mica greisenization, which may lead to different ore element complexation for the different greisen types and therefore different ore mineralization. For quartz-mica greisen, fluoride concentration in the fluid is low, meaning that chloride complexes are likely the main species that mobilize the rare metals (e.g., Sn, REEs, etc., Migdisov et al., 2016; Korges et al., 2018). For example, an experimental study found that a reduced and acidic fluid was capable of transporting a high concentration of tin chloride complexes (Heinrich, 1990). Further, Korges et al. (2018) documented the fluid inclusions in the Zinnwald/Cínovec deposit, and they proposed that tin was mainly transported as chlorides ($SnCl_4(H_2O)_2$ and $SnCl_3^-$) during greisenization. Experimental data on the stability of tin chloride suggest that $SnCl_2^0$ and $SnCl_3^-$ are the dominant species when the chloride

concentration is over 0.1 mol/kg (Müller and Seward, 2001). In another study, Migdisov et al. (2016) evaluated the mechanisms of REEs transport and found that chloride plays the main role in REEs transportation. Furthermore, the greater stability of LREE-chlorides than HREE-chlorides results in the fractionation of REEs (Migdisov et al., 2009; Gysi et al., 2013; Tsay et al., 2014). Our simulation profile suggests that Cl^- is the dominant anion and acidic condition during the whole process of greisenization (Fig. 4.7), which indicates chloride complex could be one of the main species to transport these elements (e.g., Sn, REEs) in the process of greisenization.

The fluids involved in the formation of quartz-topaz greisen are generally more F-rich than those causing quartz-mica greisen formation, and also take a different path through the pH-c_F parameter space (Fig. 4.11). Fluorine likely influences the ore formation processes in two ways. First, fluorine could transport metals by forming fluoride complexes. Experiments on F complexation suggest that fluorine complexes of tungsten, such as $H_3WO_4F_2^-$, could be the dominant transport species in aqueous fluids with high F concentrations (Wang et al., 2021; Mei et al., 2024). Therefore quartz-topaz greisenization could also be responsible for tungsten enrichment. Numerous studies have shown that high field strength elements (HFSE) have high solubility at high HF concentrations and low pH values (Jiang et al., 2005; Ryzhenko et al., 2006; Zaraisky et al., 2010; Migdisov et al., 2011; Timofeev et al., 2015; Akinfiev et al., 2020), which indicates that these metals could be mobilized by corresponding fluoride complexes in the ore forming processes. Yet, fluorine could also be responsible for metal precipitation. Due to the low solubility of REE fluorides, F-rich environment can result in the deposition of REEs minerals like fluocerite - (Ce) and bastnaesite- (Ce) (Williams-Jones et al., 2012; Migdisov et al., 2016). Therefore, our findings suggest that there is a high mineralization potential for these elements during the process of quartz-topaz greisenization due to the F-rich fluid.

The distinctive fluid conditions of quartz-topaz and quartz-mica greisenization provide a wider environment for mineralization, and these conditions help explain the variable mineralization in greisen-related deposits. The decoupling of W and Sn mineralization observed in W-Sn deposits (Audétat et al., 2000; Zhao et al., 2021; Song et al., 2022) may be best explained by the fact that mica formation and breakdown redistribute Sn much more than W, whereas fluoride complexation (more prevalent during the formation of topaz-bearing greisen) is more relevant to W mobility.

4.5. Conclusions

Our numerical modeling reproduced the greisen sequences found in natural examples while also providing quantitative constrains on pH values and F concentrations of the involved fluids. Our results reveal that fluid composition controls the variation of greisen. Our major findings are as follows:

1) Both the F concentration and the pH value of the infiltrating fluid control the mineralogical variation

of greisen. Fluids with lower F concentrations enhance the dominant formation of quartz-mica greisen, whereas fluids with higher F concentrations promote the formation of quartz-topaz greisen. High F concentrations of the initial fluid cause mica-free quartz-topaz greisen to develop. Quartz-mica greisen assemblages are stable at pH values of 3.2–4.9, while quartz-topaz greisen assemblages are more flexible, in that they can tolerate a pH value lower than 5.8 of the infiltrating fluid.

2) The extensive porosity that develops during quartz-topaz greisen formation enables large quantities of fluid to affect the greisen zone.
3) The fluids equilibrating with quartz-topaz greisen correspond to F-dominant fluid conditions whereas fluids equilibrating with quartz-mica greisen tend to be Cl-rich fluids, suggesting that the differences in the main ligands for metal mobilization could result in different ore mineralization.

Acknowledgements

We thank Dr. Xin Zhong for valuable discussion. We would also like to thank Celeste Brennecka for checking over an earlier version of the manuscript. Funded by the Deutsche Forschungsgemeinschaft (DFG, German Research Foundation) – Project-ID 387284271 – SFB 1349 and China Scholarship Council (No. 201908110287).

Appendix A. Supplementary Material

The supplementary material includes figures of a P-T benchmark diagram of OH- and F- topaz solid solution and calculations of Na-rich system and K-rich system.

Data Availability

Data are available through Mendeley Data at https://doi.org/10.17632/y9f4gz9sft.1.

References

Akinfiev, N.N., Korzhinskaya, V.S., Kotova, N.P., Redkin, A.F., Zotov, A.V., 2020. Niobium and tantalum in hydrothermal fluids: Thermodynamic description of hydroxide and hydroxofluoride complexes. Geochimica et Cosmochimica Acta, 280, 102-115.

Audétat, A., Günther, D., Heinrich, C.A., 2000. Magmatic-hydrothermal evolution in a fractionating granite: A microchemical study of the Sn-W-F-mineralized Mole granite (Austrialia). Geochimica et Cosmochimica Acta, 64, 3373-3393.

Barton, M.D., 1982. The thermodynamic properties of topaz solid solutions and some petrologic applications. American Mineralogist, 67, 956-974.

Beinlich, A., John, T., Vrijmoed, J.C., Tominaga, M., Magna, T., Podladchikov, Y.Y., 2020. Instantaneous rock transformations in the deep crust driven by reactive fluid flow. Nature Geoscience, 13, 307-311.

Bethke, C.M., 1996. Geochemical Reaction Modeling: Concepts and Applications. Oxford University Press.

Breiter, K., Ďurišová, J., Dosbaba, M., 2017a. Quartz chemistry - A step to understanding magmatic-hydrothermal processes in ore-bearing granites: Cínovec/Zinnwald Sn-W-Li deposit, Central Europe. Ore Geology Reviews, 90, 25-35.

Breiter, K., Ďurišová, J., Hrstka, T., Korbelová, Z., Hložková Vaňková, M., Vašinová Galiová, M., Kanický, V., Rambousek, P., Knésl, I., Dobeš, P., Dosbaba, M., 2017b. Assessment of magmatic vs. metasomatic processes in rare-metal granites: A case study of the Cínovec/Zinnwald Sn-W-Li deposit, Central Europe. Lithos, 292-293, 198-217.

Breiter, K., Hložková, M., Korbelová, Z., Galiová, M.V., 2019. Diversity of lithium mica compositions in mineralized granite-greisen system: Cínovec Li-Sn-W deposit, Erzgebirge. Ore Geology Reviews, 106, 12-27.

Burt, D.M., 1981. Acidity-salinity diagrams-application to greisen and porphyry deposits. Economic Geology, 76, 832-843.

Chen, L.-L., Ni, P., Dai, B.-Z., Li, W.-S., Chi, Z., Pan, J.-Y., 2019. The Genetic Association between Quartz Vein- and Greisen-Type Mineralization at the Maoping W–Sn Deposit, Southern Jiangxi, China: Insights from Zircon and Cassiterite U–Pb Ages and Cassiterite Trace Element Composition. Minerals, 9.

Connolly, J.A.D., 2005. Computation of phase equilibria by linear programming: A tool for geodynamic modeling and its application to subduction zone decarbonation. Earth and Planetary Science Letters, 236, 524-541.

Connolly, J.A.D., 2009. The geodynamic equation of state: What and how. Geochemistry, Geophysics, Geosystems, 10, Q10014.

Crerar, D.A., 1975. A method for computing multicompontent chemical equilibria based on equilibrium constants. Geochimica et Cosmochimica Acta, 39, 1375-1384.

Dolejš, D., Baker, D.R., 2004. Thermodynamic analysis of the system Na_2O-K_2O-CaO-Al_2O_3-SiO_2-H_2O-F_2O_{-1}: Stability of fluorine-bearing minerals in felsic igneous suites. Contributions to Mineralogy and Petrology, 146, 762-778.

Dolejš, D., Baker, D.R., 2007. Liquidus Equilibria in the System K_2O-Na_2O-Al_2O_3-SiO_2-F_2O_{-1}-H_2O to 100 MPa: I. Silicate-Fluoride Liquid Immiscibility in Anhydrous Systems. Journal of Petrology, 48, 785-806.

Dolejš, D., Wagner, T., 2008. Thermodynamic modeling of non-ideal mineral-fluid equilibria in the system Si-Al-Fe-Mg-Ca-Na-K-H-O-Cl at elevated temperatures and pressures: Implications for hydrothermal mass transfer in granitic rocks. Geochimica et Cosmochimica Acta, 72, 526-553.

Govorov, I.N., 1977. Thermodynamics of ionic mineral equilibria and mineralogy of hydrothermal deposits. -Izd. Nauka, Moskva.

Gysi, A.P., Williams-Jones, A.E., 2013. Hydrothermal mobilization of pegmatite-hosted REE and Zr at Strange Lake, Canada: A reaction path model. Geochimica et Cosmochimica Acta, 122, 324-352.

Halter, W.E., Williams-Jones, A.E., Kontak, D.J., 1995. Origin and evolution of the greisenizing fluid at the East Kemptville tin deposit, Nova Scotia, Canada. Economic Geology, 93, 1026-1051.

Halter, W.E., Williams-Jones, A.E., Kontak, D.J., 1996. The role of greisenization in cassiterite precipitation at the East Kemptville tin deposit, Nova Scotia. Economic Geology, 91, 368-385.

Halter, W.E., Williams-Jones, A.E., Kontak, D.J., 1998. Modeling fluid-rock interaction during greisenization at the East Kemptville tin deposit: implications for mineralization. Chemical Geology, 150, 1-17.

Heinrich, C.A., 1990. The chemistry of hydrothermal Tin(-tungsten) ore deposition. Economic Geology, 85, 457-481.

Holland, T.J.B., Powell, R., 1998. An internally consistent thermodynamic data set for phases of petrological interest. Journal of Metamorphic Geology, 16, 309-343.

Huber, K., Vrijmoed, J.C., John, T., 2022. Formation of Olivine Veins by Reactive Fluid Flow in a Dehydrating Serpentinite. Geochemistry, Geophysics, Geosystems, 23, e2021GC010267.

Jiang, S.-Y., Wang, R.-C., Xu, X.-S., Zhao, K.-D., 2005. Mobility of high field strength elements (HFSE) in magmatic-, metamorphic-, and submarine-hydrothermal systems. Physics and Chemistry of the Earth, Parts A/B/C, 30, 1020-1029.

John, T., Gussone, N., Podladchikov, Y.Y., Bebout, G.E., Dohmen, R., Halama, R., Klemd, R., Magna, T., Seitz, H.-M., 2012. Volcanic arcs fed by rapid pulsed fluid flow through subducting slabs. Nature Geoscience, 5, 489-492.

Johnson, J.W., Oelkers, E.H., Helgeson, H.C., 1992. Supcrt92: A software package for calculating the standard molal thermodynamic properties of minerals, gases, aqueous species, and reactions from 1 to 5000 bar and 0 to 1000 °C. Computers & Geosciences, 18, 899-947.

Korges, M., Weis, P., Lüders, V., Laurent, O., 2018. Depressurization and boiling of a single magmatic fluid as a mechanism for tin-tungsten deposit formation. Geology, 46, 75-78.

Kühne, R., Wasternack, J., Schulze, H., 1972. Post-magmatische Metasomatose im Endo-Exokontakt der jüngeren postkinematischen Granite des Erzgebirges. Geologie, 21, 494-520.

Kusebauch, C., John, T., Barnes, J.D., Klügel, A., Austrheim, H.O., 2015. Halogen Element and Stable Chlorine Isotope Fractionation Caused by Fluid–Rock Interaction (Bamble Sector, SE Norway). Journal of Petrology, 56, 299-324.

Launay, G., Sizaret, S., Guillou-Frottier, L., Fauguerolles, C., Champallier, R., Gloaguen, E., 2019. Dynamic Permeability Related to Greisenization Reactions in Sn-W Ore Deposits: Quantitative Petrophysical and Experimental Evidence. Geofluids, 2019, 1-23.

Launay, G., Sizaret, S., Lach, P., Melleton, J., Gloaguen, E., Poujol, M., 2021. Genetic relationship between greisenization and Sn-W mineralization in vein and greisen deposits: Insights from the Panasqueira deposit (Portugal). BSGF - Earth Sciences Bulletin, 192, 2-29.

Lecumberri-Sanchez, P., Vieira, R., Heinrich, C.A., Pinto, F., Wälle, M., 2017. Fluid-rock interaction is decisive for the formation of tungsten deposits. Geology, 45, 579-582.

Leopardi, D., Gutzmer, J., Lehmann, B., Burisch, M., 2024. The Spatial and Temporal Evolution of the Sadisdorf Li-Sn-(W-Cu) Magmatic-Hydrothermal Greisen and Vein System, Eastern Erzgebirge, Germany. Economic Geology, 119, 771-803.

Li, J., Gao, J., John, T., Klemd, R., Su, W., 2013. Fluid-mediated metal transport in subduction zones and its link to arc-related giant ore deposits: Constraints from a sulfide-bearing HP vein in lawsonite eclogite (Tianshan, China). Geochimica et Cosmochimica Acta, 120, 326-362.

Loges, A., Manni, M., Louvel, M., Wilke, M., Jahn, S., Welter, E., Borchert, M., Qiao, S., Klemme, S., Keller, B.G., John, T., 2024. Complexation of Zr and Hf in fluoride-rich hydrothermal aqueous fluids and its significance for high field strength element fractionation. Geochimica et Cosmochimica Acta, 366, 167-181.

Loges, A., Migdisov, A.A., Wagner, T., Williams-Jones, A.E., Markl, G., 2013. An experimental study of the aqueous solubility and speciation of Y(III) fluoride at temperatures up to 250 °C. Geochimica et Cosmochimica Acta, 123, 403-415.

Loges, A., Scholz, G., de Sousa Amadeu, N., Shao, J., Schultze, D., Fuller, J., Paulus, B., Emmerling, F., Braun, T., John, T., 2022. Studies on the local structure of the F⁄OH site in topaz by magic angle spinning nuclear magnetic resonance and Raman spectroscopy. European Journal of Mineralogy, 34, 507-521.

Malvoisin, B., Podladchikov, Y.Y., Vrijmoed, J.C., 2015. Coupling changes in densities and porosity to fluid pressure variations in reactive porous fluid flow: Local thermodynamic equilibrium. Geochemistry, Geophysics, Geosystems, 16, 4362-4387.

Marignac, C., Cuney, M., 1991. What is the meaning of granite specialization for Sn, W deposit genesis? In Pagel, M., Leroy, J.L. (Eds.), Source, transport and deposition of metals. Balkema, Rotterdam, 771-774.

Mei, Y., Liu, W., Guan, Q., Brugger, J., Etschmann, B., Siegel, C., Wykes, J., Ram, R., 2024. Tungsten speciation in hydrothermal fluids. Geochimica et Cosmochimica Acta (In press).

Migdisov, A.A., Williams-Jones, A.E., Brugger, J., Caporuscio, F.A., 2016. Hydrothermal transport, deposition, and fractionation of the REE: Experimental data and thermodynamic calculations. Chemical Geology, 439, 13-42.

Migdisov, A.A., Williams-Jones, A.E., van Hinsberg, V., Salvi, S., 2011. An experimental study of the solubility of baddeleyite (ZrO_2) in fluoride-bearing solutions at elevated temperature. Geochimica et Cosmochimica Acta, 75, 7426-7434.

Migdisov, A.A., Williams-Jones, A.E., Wagner, T., 2009. An experimental study of the solubility and speciation of the Rare Earth Elements (III) in fluoride- and chloride-bearing aqueous solutions at temperatures up to 300 °C. Geochimica et Cosmochimica Acta, 73, 7087-7109.

Mikucki, E.J., 1998. Hydrothermal transport and depositional processes in Archean lode-gold systems: A review. Ore Geology Reviews, 13, 307-321.

Miron, G.D., Wagner, T., Kulik, D.A., Heinrich, C.A., 2016. Internally consistent thermodynamic data for aqueous species in the system Na-K-Al-Si-O-H-Cl. Geochimica et Cosmochimica Acta, 187, 41-78.

Monnier, L., Salvi, S., Jourdan, V., Sall, S., Bailly, L., Melleton, J., Béziat, D., 2020. Contrasting fluid behavior during two styles of greisen alteration leading to distinct wolframite mineralizations: The Echassières district (Massif Central, France). Ore Geology Reviews, 124, 103648.

Monnier, L., Salvi, S., Melleton, J., Bailly, L., Béziat, D., de Parseval, P., Gouy, S., Lach, P., 2019. Multiple Generations of Wolframite Mineralization in the Echassieres District (Massif Central, France). Minerals, 9, 637.

Monnier, L., Salvi, S., Melleton, J., Lach, P., Pochon, A., Bailly, L., Béziat, D., De Parseval, P., 2022. Mica trace-element signatures: Highlighting superimposed W-Sn mineralizations and fluid sources. Chemical Geology, 600, 120866.

Müller, A., Herklotz, G., Giegling, H., 2018. Chemistry of quartz related to the Zinnwald/Cínovec Sn-W-Li greisen-type deposit, Eastern Erzgebirge, Germany. Journal of Geochemical Exploration, 190, 357-373.

Müller, B., Seward, T.M., 2001. Spectrophotometric determination of the stability of tin(II) chloride complexes in aqueous solution up to 300 °C. Geochimica et Cosmochimica Acta, 65, 4187-4199.

Nardi, L.V.S., Formoso, M.L.L., Jarvis, K., Oliveira, L., Bastos Neto, A.C., Fontana, E., 2012. REE, Y, Nb, U, and Th contents and tetrad effect in zircon from a magmatic-hydrothermal F-rich system of Sn-rare metal-cryolite mineralized granites from the Pitinga Mine, Amazonia, Brazil. Journal of South American Earth Sciences, 33, 34-42.

Ni, P., Pan, J.-Y., Han, L., Cui, J.-M., Gao, Y., Fan, M.-S., Li, W.-S., Chi, Z., Zhang, K.-H., Cheng, Z.-L., Liu, Y.-P., 2023. Tungsten and tin deposits in South China: Temporal and spatial distribution, metallogenic models and prospecting directions. Ore Geology Reviews, 157, 105453.

Peterková, T., Dolejš, D., 2019. Magmatic-hydrothermal transition of Mo-W-mineralized granite-pegmatite-greisen system recorded by trace elements in quartz: Krupka district, Eastern Krušné hory/Erzgebirge. Chemical Geology, 523, 179-202.

Pinheiro, M.V.B., Fantini, C., Krambrock, K., Persiano, A.I.C., Dantas, M.S.S., Pimenta, M.A., 2002. OH/F substitution in topaz studied by Raman spectroscopy. Physical Review B, 65, 104301.

Plümper, O., John, T., Podladchikov, Y.Y., Vrijmoed, J.C., Scambelluri, M., 2017. Fluid escape from subduction zones controlled by channel-forming reactive porosity. Nature Geoscience, 10, 150-156.

Putnis, A., 2002. Mineral replacement reactions: from macroscopic observations to microscopic mechanisms. Mineralogical Magazine, 66, 689-708.

Putnis, A., 2015. Transient Porosity Resulting from Fluid-Mineral Interaction and its Consequences. Reviews in Mineralogy and Geochemistry, 80, 1-23.

Putnis, A., John, T., 2010. Replacement Processes in the Earth's Crust. Elements, 6, 159-164.

Qiao, S., John, T., Loges, A., 2024. Formation of Topaz-Greisen by a Boiling Fluid: A Case Study from the Sn-W-Li Deposit, Zinnwald/Cínovec. Economic Geology, 119, 805-828.

Ruiz-Agudo, E., Putnis, C.V., Putnis, A., 2014. Coupled dissolution and precipitation at mineral–fluid interfaces. Chemical Geology, 383, 132-146.

Ryzhenko, B.N., Kovalenko, N.I., Prisyagina, N.I., 2006. Titanium complexation in hydrothermal systems. Geochemistry International, 44, 879-895.

Scharrer, M., Fusswinkel, T., Markl, G., 2023. Triple-halogen (Cl-Br-I) fluid inclusion LA-ICP-MS microanalysis to unravel iodine behavior and sources during marine fluid infiltration into the basement in unconformity settings. Geochimica et Cosmochimica Acta, 357, 64-76.

Shapovalov, Y.B., Setkova, T.V., 2012. Experimental study of mineral equilibria in the system $K_2O(Li_2O)$-Al_2O_3-SiO_2-H_2O-HF at 300 to 600 °C and 100 MPa with application to natural greisen systems. American Mineralogist, 97, 1452-1459.

Shcherba, G.N., 1970. Greisens. International Geology Review, 12, 114-150.

Sheard, E.R., Williams-Jones, A. E., Heiligmann, M., Pederson, C., Trueman, D. L., 2012. Controls on the Concentration of Zirconium, Niobium, and the Rare Earth Elements in the Thor Lake Rare Metal Deposit, Northwest Territories, Canada. Economic Geology, 107, 81-104.

Sillitoe, R.H., 2010. Porphyry copper systems. Economic Geology, 105, 3-41.

Smith, M.P., Henderson, P, Campbell, L.S, 2000. Fractionation of the REE during hydrothermal processes: constraints from the Bayan Obo Fe-REE-Nb deposit, Inner Mongolia, China. Geochimica et Cosmochimica Acta, 64, 3141-3160.

Soloviev, S.G., Kryazhev, S., Dvurechenskaya, S., 2020. Geology, igneous geochemistry, mineralization, and fluid inclusion characteristics of the Kougarok tin-tantalum-lithium prospect, Seward Peninsula, Alaska, USA. Mineralium Deposita, 55, 79-106.

Song, S., Mao, J., Yuan, S., Jian, W., 2022. Decoupling of Sn and W mineralization in a highly fractionated reduced granitic magma province: a case study from the Youjiang basin and Jiangnan tungsten belt. Mineralium Deposita, 57, 1251-1267.

Štemprok, M., 1987. Greisenization (a review). Geologische Rundschau, 76, 169-175.

Štemprok, M, Dolejš, D., 2010. Fluid focusing, mass transfer and origin of fracture-controlled greisens in the Western Krusne hory granite pluton, Central Europe. Zeitschrift für geologische Wissenschaften, 38, 207-234.

Taetz, S., John, T., Bröcker, M., Spandler, C., Stracke, A., 2018. Fast intraslab fluid-flow events linked to pulses of high pore fluid pressure at the subducted plate interface. Earth and Planetary Science Letters, 482, 33-43.

Timofeev, A., Migdisov, A.A., Williams-Jones, A.E., 2015. An experimental study of the solubility and speciation of niobium in fluoride-bearing aqueous solutions at elevated temperature. Geochimica et Cosmochimica Acta, 158, 103-111.

Tsay, A., Zajacz, Z., Sanchez-Valle, C., 2014. Efficient mobilization and fractionation of rare-earth elements by aqueous fluids upon slab dehydration. Earth and Planetary Science Letters, 398, 101-112.

Vrijmoed, J.C., Podladchikov, Y.Y., 2022. Thermolab: A Thermodynamics Laboratory for Nonlinear Transport Processes in Open Systems. Geochemistry, Geophysics, Geosystems, 23, e2021GC010303.

Wang, X.-S., Williams-Jones, A.E., Hu, R.-Z., Shang, L.-B., Bi, X.-W., 2021. The role of fluorine in granite-related hydrothermal tungsten ore genesis: Results of experiments and modeling. Geochimica et Cosmochimica Acta, 292, 170-187.

Webster, J., Thomas, R., Förster, H.-J., Seltmann, R., Tappen, C., 2004. Geochemical evolution of halogen-enriched granite magmas and mineralizing fluids of the Zinnwald tin-tungsten mining district, Erzgebirge, Germany. Mineralium Deposita, 39, 452-472.

Weis, P., 2015. The dynamic interplay between saline fluid flow and rock permeability in magmatic-hydrothermal systems. Geofluids, 15, 350-371.

Williams-Jones, A.E., Migdisov, A.A., Samson, I.M., 2012. Hydrothermal Mobilisation of the Rare Earth Elements - a Tale of "Ceria" and "Yttria". Elements, 8, 355-360.

Witt, W.K., 1988. Evolution of high-temperature hydrothermal fluids associated with greisenization and feldspathic alteration of a tin-mineralized granite, northeast Queensland. Economic Geology, 83, 310-334.

Zajacz, Z., Halter, W.E., Pettke, T., Guillong, M., 2008. Determination of fluid/melt partition coefficients by LA-ICPMS analysis of co-existing fluid and silicate melt inclusions: Controls on element partitioning. Geochimica et Cosmochimica Acta, 72, 2169-2197.

Zhao, P., Chu, X., Williams-Jones, A.E., Mao, J., Yuan, S., 2021. The role of phyllosilicate partial melting in segregating tungsten and tin deposits in W-Sn metallogenic provinces. Geology, 50, 121-125.

Chapter 5. Conclusions and Outlook

5.1. Conclusions

Greisen-related ore deposits are an important source for rare metals such as W, Sn, Li. The most common types of greisen associated with ore deposits are quartz-topaz and quartz-mica greisen. However, the factors controlling the variation are not well investigated. In addition, fluoride is a key component in the greisen fluid, but its influences on the formation of greisen remain unclear. This dissertation presents a systematic study using the combination of the natural bulk-rock analysis, single mineral investigation, and numerical modeling study of the Zinnwald/Cínovec greisen. These findings provide a deeper understanding of greisen formation and the potential processes involved in ore formation.

The petrological and mineralogical study of the Zinnwald/Cínovec topaz-rich greisen indicates the feldspar and zinnwaldite were eventually replaced by the quartz and topaz. During this progress, almost no mica formed, distinguishing it from quartz-mica greisen. During the process of greisenization, greisen gained F, Si, LREEs, but lost HREEs, all alkalines (Na, K). Combined with the evidence of boiling fluid inclusions, these evidences suggest that phase separation due to the fluid boiling occurred. In this process, the vapor phase, enriched in F content, reacted with the wall rock, leading the replacement of feldspar and biotite by quartz and topaz. Increasing porosity during this process allows brine solutions to infiltrate into the greisen, with the pore space later sealed by the precipitation of quartz and fluorite due to oversaturation. These findings emphasize that an additional process, such as boiling, might be required to introduce the high F concentration required for the formation of quartz-topaz greisen.

Topaz is the most important F-bearing phase in the Zinnwald/Cínovec quartz-topaz greisen. Changes in the chemical composition of topaz reflect the chemical evolution of the greisen fluid in equilibrium with the greisen. A linear correlation ($y = 0.329x - 113.6$, where y represents F concentration and x the distance of Raman bands shifts around 155 and 562 cm^{-1}) is proposed between the distance of specific Raman band positions and F concentration in topaz, providing a method to quantitatively determine the F concentration using Raman spectroscopy. Based on cathodoluminescence (CL) zonation of single topaz crystals, two types of topaz were identified in the Zinnwald/Cínovec transect. Fluorine concentrations derived from Raman results show these two types have distinct F concentrations: higher concentration (> 19.2 wt. %) for light CL zone and lower concentration (<19.2 wt. %) for the dark CL zone. This approach reveals that topaz is a key mineral sensitive to the changes in the F concentration of the equilibrated fluid.

The study of natural sample provides a foundational understanding of the greisen system. The reactive transport model offers novel constraints on the formation of greisen, particularly on the

variation of greisen and the evolution of the equilibrated fluids. Fluids with various initial composition can lead to different types of greisen. The infiltrating fluid with a lower pH value lower F concentration result in the formation of greisen characterized by a sequence of quartz-topaz and quartz-mica. In contrast, acdic fluid enriched in F (>0.015 mol/kg), lead to mica-free greisen formation. Furthermore, quartz-topaz greisen corresponds to F-rich fluids, while quartz-mica greisen corresponds to Cl-rich fluids, potentially favoring the formation of different metal complexes, such as tungsten fluoride and tin chloride. This work highlights the crucial role of F in greisenization. Detailed constraints on fluid composition and variation of greisen enhance our understanding of the greisen system and related processes.

In summary, this dissertation presents a comprehensive study of greisen. Key findings of this dissertation emphasize the role of F in the formation of greisen, providing valuable insights into greisen research. Notably, the observed greisen variations suggest that greisen-related ore deposits are more diverse than previously thought. The reactive transport model proves to be a reliable method for studying the F-related processes, contributing significantly to our understanding of greisen systems

5.2. Outlook

1. Correlation Between Ore formation and Greisen

This dissertation primarily focuses on fluid-rock interactions, offering valuable insights into the greisen system. In the future, a detailed examination of ore minerals such as cassiterite and wolframite could be conducted, which are the predominant ore minerals in greisen-related deposits. A comprehensive analysis of these ore minerals, including their texture, composition, and correlation with specific types of greisen, is essential to understanding the mineralization process during greisenization. Previous studies have shown that tungsten is particularly enriched in quartz-topaz greisen (Štemprok et al., 2005). Therefore, examining the relationship between ore minerals and greisen minerals is crucial for elucidating the mechanisms of metal enrichment.

2. Fluid Inclusions Investigation for the Comparison Between Quartz-Topaz and Quartz-Mica Greisen

The reactive transport model conducted in this study simulated the formation of quartz-topaz and quartz-mica greisen, as well as a profile of fluid evolution. It is also necessary to compare natural samples from these two types of greisen, focusing on their chemical differences and transitional phases. Fluid inclusions (FIs) study is a routine method for investigating fluid evolution (Lu et al., 2003). Thus, an FIs study could be conducted to explore the differences in fluids that are in equilibrium with each greisen type. A systematic investigation of FIs would provide valuable information on the fluids associated with different types of greisen.

3. Improving of the reactive transport modeling

While the output of the reactive transport model offers valuable constraints on greisen formation, several aspects could still be improved. For instance, mica, a critical phase in greisen, often occurs as a solid solution between hydroxyl- and fluorine-endmembers. In this study, exclusively a hydroxyl mica has been used to represent natural mica, which may have influenced the stability fields of the calculated mineral assemblages. More accurate thermodynamic data on mica is needed for future simulations. Additionally, carbon dioxide (CO_2) is commonly present in hydrothermal fluids, and the dissociation of carbonic acid affects the system's pH values. For simplicity, CO_2-related phases were not included in the current model. Addressing these issues will be crucial for further refining the numerical models of greisen formation.

4. Investigation on Dominant Metal Speciation During Greisenization

The chemical evolution of fluids during greisenization indicates that different types of greisen may correspond to varying dominant ligands (e.g., F, Cl) for metal complexes. Experimental studies have explored the speciation of tungsten in fluids, such as WO_3F^-, $WO_3F_2^{2-}$, and $H_3WO_4F_2^-$ (Wang et al., 2021; Mei et al., 2024), and the speciation of tin in forms like Sn(OH)Cl and $[SnCl_4(H_2O)_2]^0$ (Duc-Tin et al., 2007; Schmidt, 2018). Further research into the behavior of these fluid phases during greisenization is necessary to deepen our understanding of greisen-related mineralization. Additionally, Nb, Ta, Zr, and Hf are potential ore metals that may be enriched during greisenization, and similar studies on their metal speciation should be pursued. Molecular dynamics (MD) simulations are a powerful tool for calculating the speciation of metals under varying P-T-x conditions. In the future, MD simulations could be employed to calculate metal speciation under different fluid compositions (F, Cl, pH) and temperature conditions.

References

Duc-Tin, Q., Audétat, A., Keppler, H., 2007. Solubility of tin in (Cl, F)-bearing aqueous fluids at 700 °C, 140 MPa: A LA-ICP-MS study on synthetic fluid inclusions. Geochimica et Cosmochimica Acta, 71, 3323-3335.

Lu, H., Liu, Yimao, Wang, Changlie, Xu, Youzhi, Li, Huaqin, 2003. Mineralization and fluid inclusion study of the Shizhuyuan W-Sn-Bi-Mo-F skarn deposit, Hunan Province, China. Economic Geology, 98, 955-974.

Mei, Y., Liu, W., Guan, Q., Brugger, J., Etschmann, B., Siegel, C., Wykes, J., Ram, R., 2024. Tungsten speciation in hydrothermal fluids. Geochimica et Cosmochimica Acta (in press).

Schmidt, C., 2018. Formation of hydrothermal tin deposits: Raman spectroscopic evidence for an important role of aqueous Sn(IV) species. Geochimica et Cosmochimica Acta, 220, 499-511.

Štemprok, M., Pivec, E., Langrová, A., 2005. The petrogenesis of a wolframite-bearing greisen in the Vykmanov granite stock, Western Krušné hory pluton (Czech Republic). Bulletin of Geosciences, 80, 163-184.

Wang, X.-S., Williams-Jones, A.E., Hu, R.-Z., Shang, L.-B., Bi, X.-W., 2021. The role of fluorine in granite-related hydrothermal tungsten ore genesis: Results of experiments and modeling. Geochimica et Cosmochimica Acta, 292, 170-187.

Acknowledgement

At this point, I am nearing the completion of my doctoral studies, which have spanned over five years. These years have been the most significant and meaningful period of my entire academic journey, shaping the direction of my future research. I am deeply grateful to everyone who has supported and helped me along the way.

First and foremost, I would like to express my sincere gratitude to my supervisor, Prof. Timm John, who entrusted me with this fascinating project. Throughout these years, Timm has guided me with patience and kindness, and I have learned an incredible amount from him. Under his supervision, I was able to correct many of my bad research habits and develop a more rigorous approach. I am also grateful to him for providing me with a nine-month scholarship, which supported me after my CSC contract. Additionally, I would like to extend my thanks to Dr. Anselm Loges. Anselm is an incredibly patient and supportive person who has always been willing to explain concepts and answer my questions. I fondly remember the time at Haus N, where both Timm and Anselm sat beside me, helping me revise my manuscript.

I am also deeply thankful to Dr. Johannes C. Vrijmoed. What I have learned from him is invaluable, and I believe his insights are crucial in my geological research. His guidance has given me a unique edge in the competitive field, and I look forward to continuing my studies in numerical modeling. I also want to thank Dr. Xin Zhong, who has been immensely helpful in Raman spectroscopy and numerical modeling. Xin has always been generous with his time, explaining any questions I had. My gratitude also goes to Dr. Moritz Liesegang and PD Dr. Elis Hoffmann for their assistance with electron microprobe analysis and MC-ICP-MS measurements, respectively.

I would like to thank all my colleagues, even those who have since moved to other cities: Dr. Josephine Moore, Dr. Susanne Stein, Gina Rüdiger, Dr. Andreas Beinlich, Serkan Korkmaz, Pietro Potenza, Betül Sezgin, Fadime Yildirim, Christiane Behr, Prof. Ke Zhu, Dr. Uwe Wiechert, Phillip Kingsbery, Dr. Konstantin Huber, Saskia Grund, Iris Wannhoff, Dr. Jonathan Lewis, Lingzhi Hu and Dr. Lisa Kaatz. I am equally grateful to my friends who made my time here less lonely: Yuning Wang, Dr. Hailan He, Dr. Yan Lu, Dr. Guangpu Xue, Dr. Xuefeng Pan, Dr. Chenxiao Lin, Dr. Xun Yang, Shixiong Jiang, Dr. Lixiang Chen, Yunyun Xiao, Zhennan Tian, and Tingting Wang, Cedric Fontaine, Denis Koshelev, Duck Tong.

I am grateful for the financial support afforded by China Scholarship Council (CSC).

Lastly, I want to thank my parents and sister for their unwavering support. Without them, I wouldn't have become the first person in my family—and in my village—to earn a doctoral degree.

Supplementary-Chapter 2

Formation of topaz-greisen by a boiling fluid: a case study from the Sn-W-Li deposit, Zinnwald/Cínovec

Shilei Qiao[1], Timm John[1,*] , Anselm Loges[1]

[1]Institut für Geologische Wissenschaften, Freie Universität Berlin, Malteserstr. 74-100, 12249 Berlin, Germany

Some supplementary contents Published as:

Qiao, S., John, T., Loges, A., 2024. Formation of Topaz-Greisen by a Boiling Fluid: A Case Study from the Sn-W-Li Deposit, Zinnwald/Cínovec. Economic Geology, 119, 805-828.

https://doi.org/10.5382/econgeo.5074

The article is not included in the online version of this dissertation for copyright reasons.

Table 2 A4. Raw data of chemical composition of Monazite by electron micro probe analysis

No.	P_2O_5	Y_2O_3	La_2O_3	Ce_2O_3	Pr_2O_3	Nd_2O_3	Sm_2O_3	Eu_2O_3	Gd_2O_3	Tb_2O_3	Dy_2O_3	Ho_2O_3	Er_2O_3	Tm_2O_3	Yb_2O_3	Lu_2O_3	Nb_2O_3	ThO_2	UO_2	ZrO_2	Total	Zone
327	39.74	0.03	12.14	24.15	2.05	8.87	1.74	0.11	1.28	0.15	0.44	0.06	bdl	0.12	0.04	bdl	bdl	8.54	0.31	0.13	99.91	HG
240	40.37	0.13	10.79	21.41	1.99	7.86	1.49	0.08	1.35	0.17	0.56	0.07	0.04	0.10	0.09	bdl	bdl	12.69	0.27	0.06	99.50	HG
238	41.61	0.17	11.99	25.43	2.41	9.69	2.04	0.14	1.80	0.20	0.63	0.11	0.06	0.16	0.06	bdl	bdl	3.86	0.36	bdl	100.72	HG
239	40.60	bdl	12.37	24.82	2.22	8.71	1.49	0.07	1.27	0.08	0.52	0.07	bdl	0.13	0.13	bdl	bdl	8.08	0.21	0.11	100.86	HG
328	40.73	bdl	14.82	28.58	2.50	9.41	1.60	0.09	1.12	0.10	0.36	0.07	bdl	0.10	0.08	bdl	bdl	1.06	0.07	0.21	100.90	HG
329	41.06	bdl	14.49	28.51	2.44	9.39	1.60	0.10	1.12	0.14	0.35	0.03	bdl	0.11	0.10	bdl	bdl	0.95	0.03	bdl	100.42	HG
330	40.24	0.06	13.76	25.99	2.14	8.73	1.55	0.10	1.08	0.10	0.30	bdl	0.03	0.10	0.06	bdl	bdl	5.63	0.17	0.09	100.13	HG
237	39.80	0.38	10.64	20.94	1.96	7.60	1.46	0.07	1.36	0.12	0.49	0.10	0.10	0.12	0.12	bdl	bdl	13.60	0.39	0.19	99.42	HG
236	39.98	0.19	11.38	22.95	2.00	8.51	1.67	0.10	1.39	0.12	0.48	bdl	0.07	0.14	0.10	bdl	bdl	10.34	0.35	bdl	99.75	HG
241	39.87	0.07	12.76	24.96	2.19	8.96	1.49	0.08	1.45	0.16	0.62	0.05	0.04	0.12	0.14	bdl	bdl	6.38	0.14	0.08	99.54	HG
242	39.59	bdl	12.80	25.39	2.27	8.69	1.52	0.08	1.31	0.15	0.63	0.05	0.04	0.13	0.09	bdl	bdl	6.22	0.21	bdl	99.15	HG
243	40.33	bdl	13.26	23.93	2.02	8.25	1.42	0.09	1.30	0.11	0.28	0.08	0.03	0.11	0.10	bdl	bdl	7.89	0.22	0.25	99.64	HG
244	37.00	bdl	12.98	25.40	2.09	8.17	1.31	0.08	1.15	0.09	0.31	0.08	bdl	0.10	0.10	bdl	bdl	4.85	0.11	0.17	93.97	HG
245	39.14	0.03	12.54	24.69	2.14	8.67	1.58	0.09	1.34	0.12	0.55	0.12	0.04	0.13	0.06	bdl	bdl	8.04	0.29	0.15	99.72	HG
246	39.31	0.16	12.21	23.29	2.12	8.56	1.53	0.08	1.35	0.14	0.45	0.05	0.04	0.09	0.08	bdl	bdl	9.43	0.29	0.11	99.30	HG
247	38.80	0.22	11.34	22.74	2.16	8.69	1.65	0.07	1.40	0.11	0.47	0.09	0.04	0.15	0.09	bdl	bdl	10.32	0.28	0.18	98.81	HG
248	38.91	0.10	11.83	23.32	2.12	8.64	1.67	0.05	1.40	0.13	0.36	0.07	0.04	0.14	0.05	bdl	bdl	8.94	0.33	0.12	98.19	HG
249	36.95	bdl	14.95	27.14	2.13	8.27	0.77	0.06	0.75	0.11	0.10	0.05	bdl	0.06	0.07	bdl	bdl	6.86	0.21	0.19	98.64	HG
250	39.80	0.05	10.29	20.70	2.05	7.76	1.40	0.04	1.38	0.13	0.53	0.07	0.10	0.10	0.11	bdl	bdl	13.31	0.47	bdl	98.29	HG
251	40.31	bdl	12.93	27.00	2.62	10.72	2.40	0.30	1.71	0.17	0.43	0.04	0.03	0.19	0.11	bdl	bdl	0.80	0.15	0.21	100.09	HG
252	38.90	bdl	12.82	24.74	2.35	8.92	1.64	0.10	1.46	0.17	0.52	0.05	0.05	0.12	0.11	bdl	bdl	6.40	0.18	0.17	98.70	HG
253	40.11	bdl	12.21	25.55	2.52	9.82	2.30	0.27	1.76	0.15	0.52	0.10	bdl	0.21	0.11	bdl	bdl	3.65	0.20	0.17	99.64	HG
254	40.16	bdl	12.31	26.07	2.74	10.75	2.60	0.32	1.97	0.18	0.65	0.09	0.04	0.20	0.10	bdl	bdl	0.83	0.13	0.17	99.31	HG
255	39.48	0.01	12.78	24.55	2.20	8.66	1.44	0.09	1.28	0.11	0.40	0.08	0.07	0.10	0.10	bdl	bdl	7.63	0.26	0.19	99.41	HG
256	38.96	0.30	10.87	21.31	1.90	7.53	1.36	0.07	1.30	0.15	0.67	0.08	0.10	0.12	0.07	bdl	bdl	13.32	0.45	0.06	98.62	HG
293	39.50	bdl	12.51	24.83	2.25	8.96	1.55	0.10	1.25	0.14	0.38	0.08	0.07	0.11	0.05	bdl	bdl	7.04	0.23	0.16	99.21	HG

Table 2 A4. Raw data of chemical composition of Monazite by electron micro probe analysis

No.	P_2O_5	Y_2O_3	La_2O_3	Ce_2O_3	Pr_2O_3	Nd_2O_3	Sm_2O_3	Eu_2O_3	Gd_2O_3	Tb_2O_3	Dy_2O_3	Ho_2O_3	Er_2O_3	Tm_2O_3	Yb_2O_3	Lu_2O_3	Nb_2O_3	ThO_2	UO_2	ZrO_2	Total	Zone
294	39.84	bdl	13.25	25.95	2.24	9.28	1.64	0.12	1.30	0.13	0.62	0.13	0.08	0.13	0.08	bdl	bdl	4.70	0.16	0.05	99.70	HG
295	40.02	bdl	13.30	25.88	2.17	8.94	1.59	0.10	1.20	0.15	0.58	0.09	0.05	0.12	0.13	bdl	bdl	5.92	0.18	bdl	100.41	HG
296	40.04	0.08	12.64	23.18	1.93	8.35	1.44	0.11	1.15	0.13	0.45	0.09	bdl	0.12	0.04	bdl	bdl	9.79	0.33	bdl	99.87	HG
297	40.34	bdl	12.57	25.19	2.23	8.93	1.58	0.08	1.25	0.12	0.49	bdl	bdl	0.12	0.10	bdl	bdl	6.88	0.21	bdl	100.13	HG
331	39.45	bdl	13.09	25.45	2.22	8.93	1.47	0.10	1.30	0.13	0.59	bdl	0.06	0.10	0.07	bdl	bdl	5.71	0.18	0.13	98.99	HG
Avg.	39.71	0.13	12.54	24.65	2.21	8.81	1.61	0.11	1.34	0.13	0.47	0.07	0.05	0.12	0.09	/	/	7.08	0.24	0.15	99.38	
st.dev	0.97	0.11	1.12	1.97	0.20	0.75	0.34	0.07	0.23	0.03	0.13	0.02	0.02	0.03	0.03	/	/	3.59	0.10	0.05	1.23	
97	40.94	0.12	12.14	26.02	2.51	9.75	2.10	0.19	1.61	0.19	0.75	0.10	0.08	0.16	0.12	bdl	bdl	3.55	0.49	0.24	101.05	LG
98	41.06	0.13	12.02	25.93	2.54	9.92	2.07	0.11	1.58	0.20	0.63	0.03	bdl	0.14	0.13	bdl	bdl	3.97	0.39	0.10	100.97	LG
99	39.76	0.13	11.51	22.96	2.24	8.31	1.54	0.06	1.26	0.14	0.53	bdl	bdl	0.12	0.10	bdl	bdl	9.69	0.33	0.08	98.78	LG
100	39.66	0.14	12.55	25.34	2.31	8.84	1.49	0.06	1.21	0.11	0.53	bdl	0.06	0.12	0.10	bdl	bdl	6.92	0.21	0.05	99.68	LG
101	40.23	0.10	12.64	23.53	2.21	8.57	1.44	0.05	1.17	0.09	0.31	0.05	bdl	0.07	0.08	bdl	bdl	9.06	0.24	0.14	99.99	LG
102	37.61	0.15	14.21	25.97	2.21	8.01	1.16	0.05	0.87	0.07	0.26	bdl	bdl	0.07	0.03	bdl	bdl	7.58	0.23	0.06	98.53	LG
103	39.80	0.10	11.76	24.71	2.43	9.43	1.82	0.05	1.52	0.18	0.53	0.09	0.06	0.14	0.11	bdl	bdl	6.30	0.27	bdl	99.30	LG
105	39.71	0.12	12.68	24.16	2.18	8.66	1.75	0.13	1.40	0.15	0.51	0.08	bdl	0.15	0.13	bdl	bdl	7.86	0.24	0.09	100.02	LG
106	40.63	0.12	11.65	24.31	2.53	9.81	2.04	0.06	1.68	0.19	0.64	0.15	0.05	0.15	0.14	bdl	bdl	5.39	0.33	0.09	99.94	LG
107	40.13	0.16	12.72	25.05	2.20	8.98	1.85	0.10	1.48	0.15	0.64	bdl	0.05	0.14	0.08	bdl	bdl	5.63	0.23	0.07	99.65	LG
109	40.00	0.15	12.05	27.75	2.64	10.18	1.59	0.08	1.04	0.13	0.44	0.05	bdl	0.08	0.12	bdl	bdl	4.26	0.10	0.18	100.84	LG
110	40.71	0.13	12.10	29.85	2.87	10.49	1.39	0.05	0.82	0.07	0.18	0.05	bdl	0.11	0.09	bdl	bdl	2.61	0.02	bdl	101.55	LG
111	39.82	0.13	12.07	27.85	2.83	10.59	1.59	0.00	1.04	0.09	0.27	bdl	bdl	0.07	0.08	bdl	bdl	3.70	0.22	bdl	100.37	LG
112	39.81	0.12	11.47	26.16	2.54	9.94	1.51	0.06	1.07	0.11	0.20	bdl	bdl	0.10	0.11	bdl	bdl	7.56	0.12	0.13	101.04	LG
113	39.49	0.13	12.66	25.66	2.36	9.33	1.51	0.07	1.04	0.06	0.30	bdl	bdl	0.10	0.12	bdl	bdl	7.38	0.28	0.15	100.63	LG
114	40.24	0.13	12.30	23.60	2.07	8.34	1.43	0.08	1.15	0.12	0.47	0.05	0.04	0.12	0.11	bdl	bdl	9.64	0.40	0.11	100.38	LG
180	38.98	0.11	11.40	22.41	2.10	8.09	1.39	0.06	1.24	0.19	0.62	bdl	0.09	0.13	0.10	bdl	bdl	11.75	0.38	0.30	99.36	LG
181	39.91	0.13	11.59	22.58	2.05	8.30	1.52	0.06	1.29	0.15	0.46	0.07	0.04	0.12	0.05	bdl	bdl	11.12	0.32	bdl	99.74	LG
182	39.52	0.13	11.67	22.87	2.21	8.24	1.46	0.04	1.18	0.15	0.53	0.04	0.04	0.11	0.10	bdl	bdl	10.42	0.37	0.11	99.19	LG
183	40.29	0.12	11.22	22.99	2.25	8.83	1.61	0.05	1.28	0.17	0.48	0.05	0.07	0.16	0.13	bdl	bdl	9.89	0.50	bdl	100.10	LG
184	40.21	0.11	11.17	22.65	2.25	8.82	1.83	0.06	1.43	0.13	0.51	0.10	0.06	0.12	0.10	bdl	bdl	9.79	0.47	0.05	99.86	LG

Table 2 A4. Raw data of chemical composition of Monazite by electron micro probe analysis

No.	P_2O_5	Y_2O_3	La_2O_3	Ce_2O_3	Pr_2O_3	Nd_2O_3	Sm_2O_3	Eu_2O_3	Gd_2O_3	Tb_2O_3	Dy_2O_3	Ho_2O_3	Er_2O_3	Tm_2O_3	Yb_2O_3	Lu_2O_3	Nb_2O_3	ThO_2	UO_2	ZrO_2	Total	Zone
185	39.50	0.09	13.57	25.43	2.28	8.56	1.32	0.08	0.98	0.10	0.33	0.03	0.03	0.08	0.06	bdl	bdl	7.10	0.20	0.14	99.88	LG
186	40.76	0.13	11.51	25.90	2.47	9.71	1.89	0.08	1.35	0.08	0.53	0.18	0.05	0.11	0.11	bdl	bdl	4.96	0.35	bdl	100.14	LG
187	40.89	0.08	12.36	24.19	2.33	8.80	1.60	0.04	1.29	0.14	0.44	0.09	bdl	0.11	0.16	bdl	bdl	8.06	0.23	bdl	100.78	LG
188	40.43	0.16	12.48	25.22	2.33	8.93	1.50	0.04	1.18	0.13	0.50	0.07	0.04	0.14	0.04	bdl	bdl	6.67	0.33	0.17	100.35	LG
257	39.23	0.00	14.80	29.22	2.40	8.93	0.97	0.05	0.54	0.02	0.24	bdl	bdl	0.06	0.07	bdl	bdl	2.25	0.07	0.09	98.93	LG
258	39.68	0.07	12.60	24.25	2.13	8.68	1.56	0.07	1.31	0.13	0.37	0.04	0.06	0.11	0.06	bdl	bdl	7.94	0.20	0.18	99.41	LG
259	39.76	0.06	13.21	24.18	2.04	8.33	1.44	0.11	1.18	0.13	0.31	bdl	bdl	0.08	0.08	bdl	bdl	8.16	0.12	0.12	99.31	LG
260	37.51	0.28	9.45	19.12	1.83	7.12	1.34	0.06	1.30	0.13	0.52	0.04	0.07	0.11	0.07	bdl	bdl	13.76	0.58	0.37	93.63	LG
332	39.56	bdl	12.51	24.40	2.18	8.72	1.57	0.07	1.24	0.10	0.50	0.03	0.03	0.14	0.12	bdl	bdl	7.95	0.15	bdl	99.27	LG
333	39.89	0.15	15.29	28.68	2.20	8.11	0.96	0.07	0.56	0.07	0.18	0.06	bdl	0.06	0.14	bdl	bdl	2.60	0.12	bdl	99.15	LG
334	38.97	0.16	10.49	21.20	1.96	7.89	1.38	0.08	1.31	0.15	0.66	0.05	0.10	0.14	0.09	bdl	bdl	13.58	0.45	0.06	98.70	LG
261	39.42	0.07	12.79	25.57	2.35	8.89	1.48	0.07	1.30	0.11	0.53	0.10	0.05	0.12	0.07	bdl	bdl	6.06	0.15	0.18	99.31	LG
264	40.29	0.43	14.43	28.23	2.37	9.09	1.45	0.08	1.25	0.13	0.44	0.07	0.05	0.09	0.05	bdl	bdl	0.57	0.00	0.05	99.04	LG
265	40.16	0.15	14.45	27.54	2.20	8.59	1.33	0.10	0.99	0.08	0.39	bdl	bdl	0.09	0.08	bdl	bdl	3.17	0.11	0.15	99.57	LG
266	38.59	0.29	10.02	19.27	1.81	7.49	1.38	0.09	1.39	0.17	0.79	0.05	0.10	0.10	0.10	bdl	bdl	13.69	0.60	0.03	95.94	LG
267	41.36	bdl	8.30	23.97	3.02	15.04	3.81	0.04	2.49	0.22	0.71	0.04	bdl	0.28	0.09	bdl	bdl	1.01	0.14	bdl	100.50	LG
268	40.73	bdl	12.21	23.36	2.05	8.28	1.49	0.07	1.24	0.09	0.44	0.12	bdl	0.09	0.11	bdl	bdl	9.54	0.24	0.06	100.13	LG
298	39.35	0.04	13.00	25.20	2.26	9.19	1.58	0.07	1.19	0.15	0.64	0.04	0.05	0.14	0.12	bdl	bdl	5.88	0.20	0.12	99.20	LG
299	39.24	0.12	12.06	23.51	2.14	8.51	1.52	0.08	1.24	0.14	0.39	0.09	bdl	0.13	0.10	bdl	bdl	9.52	0.33	0.13	99.26	LG
300	39.71	0.13	11.95	23.25	2.09	8.40	1.54	0.08	1.25	0.14	0.54	0.11	bdl	0.10	0.10	bdl	bdl	9.70	0.37	bdl	99.47	LG
301	39.53	0.32	11.00	26.55	2.62	10.66	1.94	0.04	1.24	0.12	0.45	0.04	0.04	0.15	0.13	bdl	bdl	3.20	0.21	0.08	98.31	LG
269	40.62	0.28	9.96	25.41	2.71	12.17	2.89	0.05	2.14	0.20	0.68	0.05	0.05	0.26	0.15	bdl	bdl	1.65	0.18	0.05	99.49	LG
270	39.17	0.30	11.68	23.39	2.15	8.51	1.67	0.13	1.46	0.12	0.51	0.06	0.04	0.11	0.08	bdl	bdl	8.67	0.35	0.28	98.67	LG
271	39.05	0.23	12.59	23.77	2.00	8.05	1.37	0.11	1.10	0.07	0.48	bdl	0.08	0.12	0.11	bdl	bdl	9.52	0.36	0.21	99.22	LG
272	39.57	0.20	12.59	24.06	2.04	8.20	1.36	0.07	1.16	0.12	0.35	0.05	bdl	0.12	0.08	bdl	bdl	8.66	0.23	bdl	98.86	LG
273	39.99	0.24	11.81	23.63	2.12	8.28	1.44	0.08	1.22	0.10	0.64	0.06	0.03	0.08	0.05	bdl	bdl	9.46	0.29	0.27	99.78	LG
303	40.52	bdl	13.47	28.79	2.41	9.03	1.44	0.10	1.00	0.09	0.41	0.08	bdl	0.12	0.12	bdl	bdl	1.95	0.21	0.11	99.85	LG
304	40.74	0.05	12.98	28.23	2.42	9.05	1.44	0.10	1.09	0.13	0.44	0.06	0.09	0.11	0.09	bdl	bdl	3.06	0.26	0.13	100.45	LG

Table 2 A4. Raw data of chemical composition of Monazite by electron micro probe analysis

No.	P_2O_5	Y_2O_3	La_2O_3	Ce_2O_3	Pr_2O_3	Nd_2O_3	Sm_2O_3	Eu_2O_3	Gd_2O_3	Tb_2O_3	Dy_2O_3	Ho_2O_3	Er_2O_3	Tm_2O_3	Yb_2O_3	Lu_2O_3	Nb_2O_3	ThO_2	UO_2	ZrO_2	Total	Zone
305	40.59	0.05	12.50	27.42	2.45	9.14	1.49	0.10	1.13	0.14	0.44	bdl	0.03	0.10	0.03	bdl	bdl	3.34	0.29	0.17	99.39	LG
306	39.72	0.26	12.24	23.43	2.06	8.05	1.38	0.05	1.12	0.13	0.39	0.07	0.06	0.13	0.10	bdl	bdl	9.94	0.38	bdl	99.50	LG
307	40.24	0.22	13.25	24.41	1.97	7.93	1.42	0.11	1.23	0.15	0.42	0.09	0.05	0.10	0.07	bdl	bdl	7.89	0.29	0.09	99.91	LG
308	39.82	0.20	12.51	26.48	2.49	10.16	1.82	0.06	1.42	0.14	0.61	0.03	0.03	0.14	0.08	bdl	bdl	3.16	0.10	bdl	99.25	LG
310	40.30	0.20	12.67	26.74	2.50	10.24	1.81	0.04	1.35	0.12	0.52	0.04	0.05	0.10	0.07	bdl	bdl	1.85	0.08	0.25	99.10	LG
312	39.67	0.20	12.14	23.92	2.10	8.59	1.56	0.05	1.22	0.10	0.40	0.09	bdl	0.13	0.07	bdl	bdl	8.83	0.21	0.09	99.38	LG
313	39.69	0.18	12.43	24.93	2.23	9.28	1.68	0.10	1.35	0.11	0.52	0.07	bdl	0.12	0.07	bdl	bdl	6.86	0.15	0.16	99.95	LG
314	39.45	0.17	12.60	24.84	2.11	9.15	1.59	0.09	1.22	0.11	0.46	0.09	bdl	0.11	0.13	bdl	bdl	7.01	0.12	0.24	99.47	LG
315	40.77	0.65	11.05	28.38	2.75	10.73	1.97	0.05	1.35	0.18	0.64	0.08	0.04	0.13	0.06	bdl	bdl	0.83	0.08	0.16	99.91	LG
317	39.93	0.25	12.37	24.69	2.22	8.87	1.54	0.08	1.26	0.16	0.54	0.06	0.03	0.10	0.07	bdl	bdl	7.54	0.10	0.12	99.92	LG
319	39.05	bdl	14.72	26.99	2.08	8.11	0.86	0.08	0.70	0.07	0.17	0.11	0.05	0.03	0.10	bdl	bdl	5.91	0.23	0.15	99.41	LG
321	38.76	bdl	15.46	27.66	2.19	8.35	0.86	0.07	0.66	0.04	0.17	bdl	bdl	0.05	0.11	bdl	bdl	5.42	0.15	0.15	100.10	LG
322	38.85	bdl	15.43	27.89	2.20	8.42	0.83	0.08	0.58	0.07	0.14	bdl	bdl	0.04	0.06	bdl	bdl	5.03	0.26	0.05	99.92	LG
323	37.19	bdl	13.28	27.54	2.28	8.56	0.82	0.06	0.57	0.05	0.25	bdl	bdl	0.05	0.13	bdl	bdl	7.29	0.27	0.26	98.58	LG
Avg.	39.79	0.16	12.38	25.13	2.29	9.02	1.56	0.07	1.21	0.12	0.46	0.07	0.05	0.11	0.09	/	/	6.72	0.25	0.14	99.55	
st.dev	0.81	0.10	1.34	2.23	0.24	1.18	0.44	0.03	0.32	0.04	0.15	0.03	0.02	0.04	0.03	/	/	3.26	0.13	0.08	1.12	
117	39.55	0.12	11.78	24.47	2.17	8.38	1.32	0.07	1.02	0.12	0.55	0.09	0.03	0.14	0.13	bdl	bdl	9.84	0.16	0.16	100.10	A
121	38.57	0.14	11.70	22.66	1.93	7.58	1.38	0.09	1.19	0.13	0.66	0.08	0.06	0.11	0.13	bdl	bdl	12.04	0.46	0.25	99.13	A
155	39.92	0.12	11.81	23.44	2.20	8.94	1.55	0.09	1.23	0.12	0.47	0.04	0.04	0.09	0.11	bdl	bdl	9.31	0.24	0.25	99.97	A
156	39.74	0.15	13.09	25.28	2.29	8.58	1.33	0.03	1.09	0.11	0.44	0.04	bdl	0.12	0.10	bdl	bdl	6.94	0.21	0.08	99.61	A
158	40.93	0.13	11.59	22.27	2.15	8.58	1.59	0.06	1.28	0.12	0.37	0.06	0.03	0.13	0.12	bdl	bdl	11.17	0.36	bdl	100.92	A
159	39.99	0.14	11.50	22.89	2.10	8.03	1.60	0.12	1.42	0.20	0.62	0.12	0.07	0.14	0.10	bdl	bdl	10.94	0.31	0.16	100.45	A
160	40.22	0.12	11.43	22.09	2.02	8.04	1.46	0.07	1.30	0.12	0.61	0.04	0.06	0.15	0.08	bdl	bdl	12.01	0.32	bdl	100.14	A
161	40.80	0.11	11.59	21.55	2.08	7.74	1.56	0.08	1.26	0.11	0.28	0.07	bdl	0.12	0.08	bdl	bdl	12.80	0.26	bdl	100.53	A
162	40.64	0.13	11.28	21.06	2.01	7.91	1.64	0.11	1.34	0.13	0.35	0.09	bdl	0.12	0.05	bdl	bdl	13.62	0.26	bdl	100.74	A
163	40.11	0.16	11.32	22.22	2.15	8.37	1.47	0.06	1.42	0.15	0.61	0.09	0.03	0.12	0.06	bdl	bdl	11.55	0.29	bdl	100.16	A
165	39.90	0.12	13.16	24.52	2.09	8.27	1.34	0.07	1.07	0.08	0.49	0.09	bdl	0.10	0.14	bdl	bdl	8.61	0.20	0.34	100.58	A
166	39.25	0.13	12.53	24.47	2.27	8.53	1.33	0.05	1.09	0.07	0.37	0.08	0.03	0.13	0.10	bdl	bdl	8.18	0.21	bdl	98.80	A

Table 2 A4. Raw data of chemical composition of Monazite by electron micro probe analysis

No.	P_2O_5	Y_2O_3	La_2O_3	Ce_2O_3	Pr_2O_3	Nd_2O_3	Sm_2O_3	Eu_2O_3	Gd_2O_3	Tb_2O_3	Dy_2O_3	Ho_2O_3	Er_2O_3	Tm_2O_3	Yb_2O_3	Lu_2O_3	Nb_2O_3	ThO_2	UO_2	ZrO_2	Total	Zone
167	39.42	0.12	12.02	23.98	2.29	8.56	1.55	0.07	1.24	0.12	0.51	0.05	bdl	0.14	0.06	bdl	bdl	9.73	0.32	0.16	100.34	A
170	39.32	0.13	10.67	22.89	2.27	9.05	1.82	0.05	1.46	0.11	0.47	0.10	0.06	0.15	0.12	bdl	bdl	10.06	0.39	bdl	99.13	A
171	39.59	0.13	11.06	22.17	2.14	8.35	1.69	0.07	1.36	0.13	0.46	0.06	0.05	0.14	0.13	bdl	bdl	11.27	0.37	0.26	99.43	A
172	39.38	0.14	10.96	22.48	2.13	8.54	1.66	0.03	1.37	0.11	0.46	0.04	0.05	0.13	0.04	bdl	bdl	11.30	0.41	0.14	99.37	A
174	38.01	0.10	10.55	24.94	2.61	10.64	1.81	0.05	1.17	0.09	0.20	bdl	bdl	0.13	0.07	bdl	bdl	8.92	0.18	0.09	99.55	A
175	39.46	0.13	12.91	24.92	2.20	8.58	1.40	0.02	1.03	0.06	0.32	0.04	bdl	0.10	0.11	bdl	bdl	8.12	0.23	0.17	99.83	A
176	39.17	0.15	12.92	24.50	2.28	8.42	1.46	0.02	1.02	0.11	0.38	0.11	bdl	0.11	0.09	bdl	bdl	8.29	0.24	0.14	99.39	A
177	40.48	0.12	7.97	25.94	3.31	14.84	3.69	0.03	2.10	0.18	0.42	0.06	bdl	0.29	0.12	bdl	bdl	1.48	0.01	0.07	101.11	A
178	39.65	0.13	11.31	23.02	2.32	8.84	1.76	0.08	1.26	0.12	0.48	0.07	bdl	0.14	0.14	bdl	bdl	10.87	0.25	0.07	100.50	A
179	38.87	0.11	10.35	23.71	2.50	11.40	2.87	0.07	2.10	0.22	0.74	0.03	0.04	0.21	0.07	bdl	bdl	5.42	0.12	0.18	99.03	A
274	41.30	0.47	16.40	27.96	2.15	8.22	1.48	0.07	1.14	0.14	0.50	0.03	0.05	0.08	0.12	bdl	bdl	0.66	0.10	0.14	100.99	A
275	40.76	0.57	15.81	27.46	2.22	8.63	1.47	0.09	1.18	0.14	0.38	0.05	0.08	0.09	0.08	bdl	bdl	0.56	0.20	0.09	99.88	A
276	40.58	0.14	15.84	28.44	2.28	8.54	1.50	0.09	1.09	0.12	0.42	0.08	bdl	0.10	0.09	bdl	bdl	0.40	0.07	0.07	99.84	A
277	40.19	0.01	12.18	22.99	2.07	8.09	1.52	0.14	1.33	0.13	0.39	0.10	bdl	0.12	0.05	bdl	bdl	10.29	0.24	0.04	99.88	A
278	40.43	0.69	12.74	28.49	2.57	8.92	1.34	0.05	0.79	0.11	0.38	0.07	0.09	0.05	0.16	bdl	bdl	2.57	0.17	bdl	99.61	A
279	41.02	0.00	8.31	23.96	3.16	14.54	3.86	0.02	2.81	0.29	0.77	0.05	bdl	0.30	0.10	bdl	bdl	0.86	0.11	0.05	100.20	A
280	41.06	0.00	8.73	23.82	3.06	14.72	3.89	0.08	2.95	0.31	0.85	0.04	bdl	0.30	0.08	bdl	bdl	0.34	0.14	0.16	100.52	A
281	40.50	0.00	9.05	24.52	2.93	14.08	3.69	0.04	2.81	0.26	0.83	bdl	0.03	0.30	0.11	bdl	bdl	0.33	0.07	0.17	99.74	A
Avg.	39.96	0.16	11.75	24.10	2.33	9.40	1.87	0.06	1.43	0.14	0.49	0.07	0.05	0.14	0.10	/	/	7.62	0.23	0.15	99.98	
st.dev	0.79	0.15	1.97	1.97	0.35	2.19	0.81	0.03	0.55	0.06	0.16	0.03	0.02	0.07	0.03	/	/	4.46	0.11	0.08	0.61	
123	39.13	0.12	11.27	21.99	2.08	8.02	1.45	0.05	1.27	0.17	0.63	0.06	0.06	0.13	0.08	bdl	bdl	12.68	0.32	0.12	99.61	R1
124	39.75	0.10	11.64	22.40	2.17	8.04	1.38	0.06	1.22	0.16	0.57	0.10	0.09	0.13	0.13	bdl	bdl	11.68	0.30	0.08	99.98	R1
125	39.25	0.11	11.25	21.84	2.07	8.01	1.42	0.08	1.31	0.13	0.56	0.11	0.07	0.14	0.11	bdl	bdl	12.96	0.40	0.16	99.96	R1
126	39.78	0.13	11.81	23.63	2.16	8.32	1.33	0.06	1.25	0.14	0.55	0.06	bdl	0.15	0.06	bdl	bdl	9.79	0.32	0.15	99.67	R1
127	38.82	0.16	11.46	25.67	2.51	10.33	2.07	0.03	1.49	0.13	0.51	0.09	bdl	0.14	0.11	bdl	bdl	5.65	0.34	0.13	99.65	R1
128	39.08	0.13	9.68	24.02	2.55	10.85	2.42	0.04	1.79	0.20	0.71	0.11	0.06	0.20	0.14	bdl	bdl	6.73	0.55	bdl	99.25	R1
130	39.44	0.12	14.21	29.05	2.42	9.24	1.05	0.05	0.53	0.03	0.13	0.08	bdl	0.05	0.07	bdl	bdl	1.88	0.12	0.15	98.61	R1
131	38.77	0.12	11.90	28.42	2.73	10.00	1.44	0.04	0.78	0.04	0.21	0.10	bdl	0.10	0.09	bdl	bdl	3.82	0.33	0.33	99.22	R1

Table 2 A4. Raw data of chemical composition of Monazite by electron micro probe analysis

No.	P_2O_5	Y_2O_3	La_2O_3	Ce_2O_3	Pr_2O_3	Nd_2O_3	Sm_2O_3	Eu_2O_3	Gd_2O_3	Tb_2O_3	Dy_2O_3	Ho_2O_3	Er_2O_3	Tm_2O_3	Yb_2O_3	Lu_2O_3	Nb_2O_3	ThO_2	UO_2	ZrO_2	Total	Zone
132	40.46	0.15	14.92	28.15	2.39	8.91	1.06	0.03	0.86	0.07	0.32	0.08	bdl	0.05	0.06	bdl	bdl	2.90	0.04	0.10	100.56	R1
133	37.76	0.14	12.16	28.69	2.78	9.96	1.18	0.05	0.68	0.05	0.27	bdl	bdl	0.09	0.11	bdl	bdl	5.05	0.14	0.14	99.25	R1
134	38.26	0.12	13.18	27.86	2.62	9.30	1.10	0.03	0.72	0.06	0.27	bdl	bdl	0.11	0.07	bdl	bdl	5.66	0.12	0.11	99.64	R1
135	37.96	0.14	13.43	27.20	2.39	8.95	1.02	0.03	0.79	0.08	0.29	bdl	bdl	0.08	0.08	bdl	bdl	6.46	0.18	0.15	99.22	R1
136	38.91	0.14	13.07	28.06	2.52	9.62	1.17	0.02	0.81	0.06	0.21	0.05	bdl	0.06	0.10	bdl	bdl	4.61	bdl	0.06	99.49	R1
138	40.40	0.13	15.30	28.63	2.54	9.11	1.42	0.05	1.00	0.12	0.33	0.03	bdl	0.08	0.05	bdl	bdl	0.86	0.29	0.15	100.50	R1
146	40.68	0.13	15.31	28.83	2.30	8.67	1.25	0.10	0.93	0.13	0.36	0.07	bdl	0.11	0.12	bdl	bdl	1.35	0.09	0.00	100.44	R1
147	39.66	0.11	11.81	25.70	2.65	10.25	1.86	0.02	1.33	0.14	0.44	0.05	0.04	0.19	0.12	bdl	bdl	4.54	0.22	0.29	99.41	R1
151	36.99	0.15	10.53	25.94	2.77	10.11	1.62	0.00	1.09	0.10	0.36	0.05	0.06	0.14	0.12	bdl	bdl	7.45	0.47	0.09	98.03	R1
152	40.20	0.12	16.03	29.23	2.10	7.47	0.96	0.09	0.51	0.05	0.20	bdl	bdl	0.03	0.12	bdl	bdl	1.82	0.08	bdl	99.01	R1
153	40.17	0.11	17.31	29.33	2.03	6.35	0.67	0.05	0.39	0.04	0.09	0.03	bdl	0.04	0.09	bdl	bdl	2.65	0.16	0.15	99.67	R1
282	39.66	0.54	9.84	25.53	2.70	11.77	2.36	0.03	1.78	0.17	0.65	0.07	0.05	0.20	0.09	bdl	bdl	3.37	0.26	bdl	99.07	R1
283	39.42	0.74	9.66	24.69	2.68	11.60	2.51	0.04	1.85	0.20	0.71	0.05	0.08	0.21	0.12	bdl	bdl	3.53	0.27	0.14	98.51	R1
324	39.19	0.16	11.50	22.63	1.95	8.07	1.43	0.10	1.21	0.15	0.59	0.04	0.08	0.11	0.07	bdl	bdl	11.53	0.42	0.15	99.38	R1
325	39.50	0.22	10.74	21.85	1.93	7.76	1.51	0.10	1.34	0.14	0.58	bdl	0.07	0.11	0.11	bdl	bdl	12.67	0.36	0.14	99.13	R1
284	40.84	0.00	16.46	28.56	2.21	8.64	1.07	0.07	0.87	0.13	0.34	0.05	0.03	0.05	0.09	bdl	bdl	1.36	bdl	0.18	100.93	R1
285	38.95	0.00	15.17	28.39	2.28	8.96	1.32	0.07	0.87	0.10	0.37	0.08	0.04	0.08	0.08	bdl	bdl	2.22	0.08	0.47	99.53	R1
286	39.17	0.17	12.93	26.28	2.35	9.76	1.69	0.06	1.28	0.15	0.51	0.04	0.03	0.14	0.12	bdl	bdl	4.49	0.22	0.15	99.54	R1
287	39.16	0.15	12.74	26.24	2.40	9.78	1.87	0.07	1.22	0.15	0.38	0.06	0.03	0.14	0.09	bdl	bdl	4.52	0.23	0.15	99.36	R1
288	38.69	0.51	10.80	24.61	2.44	10.51	2.13	0.06	1.66	0.21	0.62	0.13	0.09	0.19	0.13	bdl	bdl	5.96	0.34	0.04	99.09	R1
289	38.47	0.00	14.05	25.83	2.19	8.40	1.41	0.06	1.08	0.14	0.25	0.06	bdl	0.12	0.09	bdl	bdl	6.35	0.15	0.16	98.79	R1
290	39.77	0.33	14.04	27.43	2.22	8.23	1.29	0.05	0.89	0.13	0.39	bdl	bdl	0.09	0.08	bdl	bdl	4.36	0.24	0.15	99.72	R1
291	40.33	0.20	15.62	28.64	2.25	7.90	1.25	0.03	0.86	0.11	0.37	0.08	0.03	0.06	0.09	bdl	bdl	1.56	0.16	0.11	99.64	R1
292	39.25	0.01	13.92	26.52	2.29	8.95	1.53	0.05	1.10	0.13	0.37	bdl	bdl	0.13	0.05	bdl	bdl	4.47	0.22	0.08	99.07	R1
Avg.	39.31	0.17	12.93	26.31	2.36	9.12	1.48	0.05	1.09	0.12	0.41	0.07	0.06	0.11	0.10	/	/	5.47	0.25	0.15	99.47	
st.dev	0.86	0.16	2.09	2.41	0.24	1.21	0.44	0.02	0.37	0.05	0.17	0.03	0.02	0.05	bdl	/	/	3.59	0.12	0.09	0.60	
190	41.24	0.14	14.33	27.82	2.44	9.57	1.82	0.08	1.37	0.17	0.55	0.03	bdl	0.14	0.08	bdl	bdl	0.85	0.04	bdl	100.70	R2
191	40.66	0.14	13.98	29.14	2.42	9.55	1.50	0.09	1.12	0.10	0.19	0.05	bdl	0.06	0.05	bdl	bdl	1.37	0.07	0.07	100.54	R2

Table 2 A4. Raw data of chemical composition of Monazite by electron micro probe analysis

No.	P_2O_5	Y_2O_3	La_2O_3	Ce_2O_3	Pr_2O_3	Nd_2O_3	Sm_2O_3	Eu_2O_3	Gd_2O_3	Tb_2O_3	Dy_2O_3	Ho_2O_3	Er_2O_3	Tm_2O_3	Yb_2O_3	Lu_2O_3	Nb_2O_3	ThO_2	UO_2	ZrO_2	Total	Zone
192	40.78	0.09	10.77	27.90	3.02	12.12	2.26	0.04	1.35	0.16	0.46	0.09	bdl	0.18	0.13	bdl	bdl	0.80	0.10	bdl	100.25	R2
193	40.93	0.12	10.49	27.47	3.06	12.45	2.47	0.06	1.61	0.17	0.55	bdl	bdl	0.18	0.08	bdl	bdl	0.41	0.08	bdl	100.14	R2
194	41.17	0.12	12.40	28.24	2.77	10.96	1.99	0.05	1.34	0.14	0.44	0.09	0.05	0.13	0.12	bdl	bdl	0.21	0.17	bdl	100.37	R2
195	40.98	0.16	12.03	27.45	2.72	11.00	2.38	0.07	1.60	0.15	0.58	0.02	bdl	0.19	0.09	bdl	bdl	0.11	0.12	0.07	99.70	R2
196	40.52	0.11	13.07	28.56	2.63	10.06	1.31	0.02	0.74	0.05	0.14	0.07	bdl	0.04	0.10	bdl	bdl	3.53	0.18	bdl	101.13	R2
199	39.38	0.14	10.81	25.86	2.87	11.87	2.16	0.05	1.26	0.08	0.24	0.05	bdl	0.16	0.08	bdl	bdl	4.37	0.04	0.16	99.58	R2
202	38.96	0.12	17.09	29.62	2.13	7.76	0.65	0.06	0.32	bdl	0.13	bdl	bdl	0.05	0.09	bdl	bdl	2.78	0.16	bdl	99.95	R2
203	38.93	0.12	16.12	28.49	2.24	7.98	0.75	0.08	0.48	0.04	0.08	bdl	bdl	0.03	0.07	bdl	bdl	4.56	0.12	bdl	100.08	R2
204	41.60	0.14	16.08	29.68	2.44	8.63	1.23	0.07	0.80	0.07	0.34	bdl	bdl	0.05	0.08	bdl	bdl	0.20	bdl	bdl	101.41	R2
205	41.05	0.11	16.22	29.52	2.33	8.50	1.16	0.04	0.78	0.10	0.23	bdl	bdl	0.07	0.05	bdl	bdl	0.21	bdl	0.09	100.46	R2
206	41.45	0.12	16.51	30.07	2.37	8.65	1.04	0.01	0.74	0.09	0.20	0.06	bdl	0.03	0.08	bdl	bdl	0.35	bdl	0.02	101.80	R2
207	41.01	0.12	16.43	29.25	2.37	8.43	1.23	0.08	0.99	0.07	0.47	0.08	bdl	0.09	0.06	bdl	bdl	0.10	bdl	0.17	100.96	R2
208	40.87	0.13	13.75	27.57	2.38	8.53	1.32	0.04	0.98	0.14	0.50	0.07	0.05	0.07	0.11	bdl	bdl	1.54	bdl	0.07	98.12	R2
210	41.94	0.14	15.15	28.02	2.46	9.15	1.49	0.05	1.04	0.14	0.42	0.03	bdl	0.12	0.13	bdl	bdl	0.96	bdl	bdl	101.21	R2
211	40.84	0.13	15.22	29.37	2.48	8.91	1.15	0.06	0.88	0.05	0.30	0.03	bdl	0.07	0.05	bdl	bdl	0.42	0.08	0.07	100.10	R2
212	41.14	0.10	13.76	27.77	2.50	9.65	1.69	0.05	1.38	0.18	0.54	0.11	0.03	0.13	0.10	bdl	bdl	0.31	0.13	bdl	99.57	R2
213	41.59	0.13	11.06	25.38	2.73	11.84	2.72	0.15	2.28	0.27	0.88	0.10	0.05	0.20	0.07	bdl	bdl	0.15	0.05	bdl	99.64	R2
214	41.85	0.15	11.11	25.56	2.72	11.57	2.92	0.14	2.43	0.31	1.05	0.10	0.10	0.20	0.13	bdl	bdl	0.02	0.07	bdl	100.42	R2
215	39.59	0.13	12.41	25.77	2.42	9.42	1.86	0.08	1.51	0.14	0.49	0.06	0.07	0.16	0.11	bdl	bdl	5.11	0.16	0.14	99.63	R2
216	40.32	0.10	14.15	27.58	2.35	9.00	1.40	0.05	1.03	0.12	0.24	bdl	bdl	0.11	0.09	bdl	bdl	3.59	0.18	0.05	100.38	R2
217	40.79	0.10	14.97	29.81	2.34	9.06	1.19	0.09	0.79	0.11	0.36	bdl	bdl	0.05	0.09	bdl	bdl	1.32	bdl	0.10	101.17	R2
218	41.34	0.15	16.72	28.73	2.30	8.47	1.24	0.05	0.85	0.08	0.38	0.03	bdl	0.08	0.10	bdl	bdl	0.37	0.09	0.04	101.00	R2
219	40.78	0.18	11.81	28.71	2.78	11.48	2.08	0.06	1.38	0.12	0.47	0.03	bdl	0.15	0.10	bdl	bdl	0.13	0.05	bdl	100.32	R2
220	40.67	0.14	12.03	28.16	2.85	11.65	2.18	0.06	1.45	0.11	0.43	0.03	bdl	0.13	0.12	bdl	bdl	0.21	bdl	bdl	100.21	R2
221	40.86	0.14	11.11	26.96	2.78	12.22	2.49	0.06	1.74	0.15	0.46	0.03	bdl	0.17	0.03	bdl	bdl	0.34	0.08	bdl	99.62	R2
222	38.47	0.13	8.97	25.39	3.13	14.42	2.78	0.00	1.72	0.06	0.33	bdl	bdl	0.22	0.07	bdl	bdl	2.91	0.07	0.14	98.81	R2
223	41.79	0.08	9.34	24.83	2.90	13.55	3.12	0.00	2.26	0.18	0.68	0.12	0.04	0.23	0.06	bdl	bdl	1.76	0.17	0.11	101.24	R2
224	40.94	0.14	9.44	26.23	3.15	14.64	3.08	0.05	1.98	0.20	0.50	0.05	bdl	0.23	0.10	bdl	bdl	0.35	0.13	bdl	101.22	R2

Table 2 A4. Raw data of chemical composition of Monazite by electron micro probe analysis

No.	P_2O_5	Y_2O_3	La_2O_3	Ce_2O_3	Pr_2O_3	Nd_2O_3	Sm_2O_3	Eu_2O_3	Gd_2O_3	Tb_2O_3	Dy_2O_3	Ho_2O_3	Er_2O_3	Tm_2O_3	Yb_2O_3	Lu_2O_3	Nb_2O_3	ThO_2	UO_2	ZrO_2	Total	Zone
225	40.98	0.15	14.56	28.44	2.36	8.62	1.30	0.10	0.87	0.12	0.44	0.08	bdl	0.06	0.13	bdl	bdl	2.56	0.15	0.13	101.07	R2
226	40.20	0.13	10.69	26.18	2.86	12.02	2.71	0.05	1.64	0.20	0.49	0.09	bdl	0.17	0.06	bdl	bdl	1.53	0.10	0.29	99.40	R2
228	40.60	0.16	13.72	27.45	2.38	9.53	1.66	0.07	1.24	0.11	0.40	0.05	bdl	0.14	0.05	bdl	bdl	2.61	0.17	bdl	100.34	R2
229	40.75	0.11	14.94	29.42	2.47	8.97	1.17	0.02	0.86	0.10	0.41	0.04	bdl	0.09	0.10	bdl	bdl	0.60	0.19	0.17	100.38	R2
230	41.10	0.12	14.84	28.84	2.37	8.67	1.24	0.07	0.96	0.10	0.52	bdl	0.04	0.05	0.15	bdl	bdl	0.56	0.17	bdl	99.81	R2
231	40.70	0.12	16.11	29.00	2.32	8.26	1.21	0.05	0.78	0.06	0.29	bdl	bdl	0.06	0.09	bdl	bdl	1.24	bdl	0.03	100.33	R2
232	41.40	0.13	14.85	28.25	2.42	9.44	1.69	0.08	1.11	0.13	0.43	0.05	bdl	0.09	0.09	bdl	bdl	0.98	0.07	0.03	101.24	R2
233	41.02	0.12	11.17	24.71	2.68	11.70	2.60	0.05	1.66	0.19	0.44	0.17	0.03	0.20	0.08	bdl	bdl	3.98	0.12	0.07	100.99	R2
234	40.66	0.12	14.05	27.92	2.33	9.34	1.27	0.10	0.81	0.07	0.24	0.13	bdl	0.09	0.14	bdl	bdl	3.68	0.09	bdl	101.05	R2
235	40.21	0.13	14.27	28.17	2.43	9.22	1.63	0.06	1.14	0.12	0.18	0.13	bdl	0.13	0.08	bdl	bdl	2.85	0.08	bdl	100.84	R2
Avg.	40.75	0.13	13.41	27.83	2.57	10.17	1.78	0.06	1.23	0.13	0.41	0.07	0.05	0.12	0.09	/	/	1.50	0.11	0.10	100.38	
st.dev	0.77	0.02	2.29	1.46	0.26	1.81	0.67	0.03	0.49	0.06	0.19	0.04	0.02	0.06	0.03	/	/	1.49	0.05	0.07	0.76	

Table 2 A5 Raw data of chemical composition of albite by electron micro probe analysis

No.	SiO_2	Al_2O_3	FeO	MgO	CaO	BaO	Na_2O	K_2O	SrO	Total	Zone
zw001-1-Ab1-1	69.68	18.77	bdl	bdl	0.06	bdl	9.71	0.16	bdl	98.39	Greisen
zw001-1-Ab1-2	69.02	19.13	bdl	bdl	bdl	bdl	10.41	0.14	bdl	98.72	Greisen
zw001-1-Ab1-3	68.93	19.18	0.05	bdl	0.04	bdl	10.40	0.16	bdl	98.78	Greisen
zw001-1-Ab1-4	68.77	18.95	bdl	bdl	0.06	bdl	10.18	0.16	bdl	98.14	Greisen
zw001-1-Ab1-5	68.82	19.15	bdl	bdl	0.12	0.05	9.94	0.15	bdl	98.23	Greisen
zw001-1-Ab2-6	68.61	19.05	0.08	bdl	0.08	bdl	10.30	0.16	bdl	98.29	Greisen
zw001-1-Ab3-7	68.65	19.19	bdl	bdl	0.10	0.03	10.52	0.15	bdl	98.63	Greisen
Avg.	68.93	19.06	0.06	/	0.08	0.04	10.21	0.15	/	98.45	
St. dev	0.36	0.15	0.02	/	0.03	0.02	0.29	0.01	/	0.25	
zw001-1-3-9	68.80	18.85	0.05	bdl	bdl	bdl	11.07	0.17	bdl	98.93	Albitite
zw001-1-3-11	68.83	19.00	0.09	bdl	0.03	0.03	11.09	0.16	bdl	99.22	Albitite
zw001-1-3-12	68.91	19.04	bdl	bdl	bdl	bdl	10.97	0.18	bdl	99.12	Albitite
zw001-1-3-13	68.41	18.98	bdl	bdl	0.05	bdl	10.99	0.17	bdl	98.63	Albitite
zw001-1-4-6	69.00	18.91	bdl	bdl	bdl	bdl	11.01	0.17	bdl	99.08	Albitite
zw001-1-4-7	68.87	18.97	0.03	bdl	bdl	bdl	10.97	0.16	bdl	99.01	Albitite
zw001-1-4-8	68.87	19.01	bdl	bdl	0.05	bdl	11.15	0.20	bdl	99.30	Albitite
zw001-1-4-9	68.82	19.30	0.03	bdl	0.17	bdl	10.76	0.14	bdl	99.21	Albitite
zw001-1-4-10	68.97	18.91	bdl	bdl	bdl	bdl	10.93	0.17	bdl	99.03	Albitite
zw001-2-3-1	69.04	18.99	0.07	bdl	0.04	bdl	11.09	0.12	bdl	99.35	Albitite
zw001-2-3-2	69.17	18.80	0.03	bdl	bdl	bdl	11.23	0.18	bdl	99.42	Albitite
zw001-2-3-3	69.05	19.14	0.04	bdl	0.09	bdl	10.88	0.16	bdl	99.37	Albitite
zw001-2-3-4	69.18	18.91	0.05	bdl	bdl	0.06	10.93	0.14	bdl	99.28	Albitite
zw001-2-3-5	68.61	19.10	0.10	bdl	0.25	bdl	11.00	0.18	bdl	99.24	Albitite
zw001-2-3-6	69.32	18.94	bdl	bdl	bdl	bdl	11.17	0.07	bdl	99.51	Albitite
zw001-2-3-7	69.51	19.02	bdl	bdl	bdl	0.03	11.10	0.16	bdl	99.85	Albitite
zw001-2-3-8	69.33	19.27	0.04	bdl	0.09	0.06	10.91	0.18	0.03	99.90	Albitite
Avg.	68.98	19.01	0.05	bdl	0.10	0.05	11.02	0.16	0.03	99.26	
St. dev	0.27	0.13	0.03	bdl	0.08	0.02	0.12	0.03	/	0.31	
zw001-1-3-1	68.73	18.95	0.03	bdl	bdl	bdl	10.95	0.17	0.10	98.94	Albitite
zw001-1-3-2	68.65	19.17	0.03	bdl	0.33	bdl	10.91	0.21	bdl	99.29	Albitite
zw001-1-3-3	68.12	19.43	bdl	bdl	0.61	bdl	10.64	0.18	bdl	99.00	Albitite
zw001-1-3-4	68.51	18.98	0.14	bdl	0.13	bdl	10.87	0.19	bdl	98.81	Albitite
zw001-1-3-6	68.35	18.98	0.03	bdl	0.30	bdl	10.82	0.16	bdl	98.64	Albitite
zw001-1-3-7	68.28	19.07	bdl	bdl	0.16	bdl	10.79	0.21	bdl	98.54	Albitite
zw001-1-3-8	68.66	19.05	0.14	bdl	0.11	bdl	10.89	0.22	bdl	99.07	Albitite
zw001-1-4-1	68.67	19.21	bdl	bdl	0.20	bdl	10.96	0.21	bdl	99.28	Albitite
zw001-1-4-2	68.86	19.14	0.04	bdl	0.07	bdl	10.91	0.20	bdl	99.21	Albitite
zw001-1-4-3	68.11	19.57	bdl	bdl	0.70	bdl	10.63	0.18	bdl	99.21	Albitite
zw001-1-4-4	68.34	19.51	bdl	bdl	0.70	0.03	10.79	0.20	bdl	99.57	Albitite
zw001-1-4-5	68.62	19.53	0.03	bdl	0.46	bdl	10.76	0.21	bdl	99.62	Albitite
zw001-1-5-1	68.60	19.44	bdl	bdl	0.35	bdl	11.03	0.17	bdl	99.61	Albitite
zw001-1-5-2	68.60	19.43	bdl	bdl	0.37	bdl	11.01	0.17	bdl	99.62	Albitite
zw001-1-5-3	68.68	19.47	0.04	bdl	0.37	0.03	11.00	0.16	bdl	99.75	Albitite

Table 2 A5 Raw data of chemical composition of albite by electron micro probe analysis

No.	SiO_2	Al_2O_3	FeO	MgO	CaO	BaO	Na_2O	K_2O	SrO	Total	Zone
zw001-1-5-4	68.98	19.35	0.05	bdl	0.23	bdl	10.83	0.20	bdl	99.64	Albitite
zw001-1-5-5	68.45	19.48	0.06	bdl	0.41	bdl	10.98	0.19	bdl	99.58	Albitite
zw001-1-5-6	68.23	19.37	0.03	bdl	0.30	bdl	11.19	0.17	bdl	99.29	Albitite
zw001-2-1-1	68.78	19.08	0.03	bdl	0.16	0.03	11.07	0.16	bdl	99.31	Albitite
zw001-2-1-2	68.63	19.24	bdl	bdl	0.41	bdl	10.87	0.27	bdl	99.43	Albitite
zw001-2-1-3	68.83	19.09	bdl	bdl	0.13	bdl	10.96	0.17	bdl	99.19	Albitite
zw001-2-1-4	68.45	19.48	bdl	bdl	0.61	bdl	10.39	0.15	bdl	99.11	Albitite
zw001-2-1-5	68.32	19.25	0.12	bdl	0.32	bdl	11.08	0.23	bdl	99.31	Albitite
zw001-2-1-6	69.04	19.15	0.07	bdl	0.13	bdl	11.10	0.14	bdl	99.63	Albitite
zw001-2-1-7	69.07	18.81	0.05	bdl	0.04	0.03	10.94	0.15	bdl	99.09	Albitite
zw001-2-1-8	68.54	19.17	bdl	bdl	0.28	bdl	10.92	0.17	bdl	99.09	Albitite
zw001-2-1-9	69.44	18.88	bdl	bdl	0.03	bdl	10.99	0.15	bdl	99.52	Albitite
zw001-2-1-10	68.52	19.11	0.06	bdl	0.20	bdl	10.94	0.26	bdl	99.09	Albitite
zw001-2-2-1	68.44	19.51	bdl	bdl	0.58	0.05	10.59	0.25	bdl	99.45	Albitite
zw001-2-2-2	69.31	19.08	0.03	bdl	bdl	bdl	10.82	0.18	0.03	99.46	Albitite
zw001-2-2-3	68.90	19.23	0.03	bdl	0.22	bdl	10.85	0.25	bdl	99.48	Albitite
zw001-2-2-4	69.43	19.21	bdl	bdl	0.10	bdl	10.91	0.19	bdl	99.89	Albitite
zw001-2-2-5	69.01	19.19	0.06	bdl	0.24	0.03	10.75	0.16	bdl	99.44	Albitite
zw001-2-2-6	68.99	18.90	0.05	bdl	bdl	bdl	11.01	0.17	bdl	99.12	Albitite
zw001-2-2-7	68.89	19.25	0.11	bdl	0.36	bdl	10.92	0.15	bdl	99.69	Albitite
zw001-2-2-8	68.12	19.48	0.11	bdl	0.59	0.03	10.61	0.25	bdl	99.18	Albitite
zw001-2-2-9	68.59	19.23	0.06	bdl	0.24	bdl	10.92	0.14	bdl	99.18	Albitite
zw001-2-2-10	68.52	19.28	0.04	bdl	0.31	0.05	11.14	0.20	bdl	99.54	Albitite
zw001-2-4-1	69.26	18.92	0.07	bdl	0.06	bdl	11.26	0.17	0.06	99.81	Albitite
zw001-2-4-2	68.54	19.35	bdl	bdl	0.41	bdl	10.61	0.21	bdl	99.15	Albitite
zw001-2-4-3	69.09	19.02	bdl	bdl	bdl	bdl	11.08	0.16	bdl	99.39	Albitite
zw001-2-4-4	69.47	18.94	0.12	bdl	bdl	bdl	10.94	0.14	bdl	99.62	Albitite
zw001-2-4-5	69.31	18.94	bdl	bdl	bdl	bdl	10.88	0.15	bdl	99.31	Albitite
zw001-2-4-6	69.10	19.15	0.05	bdl	0.10	bdl	11.25	0.16	bdl	99.83	Albitite
zw001-2-4-7	68.41	19.56	0.05	bdl	0.49	bdl	10.61	0.17	bdl	99.28	Albitite
zw001-2-5-1	73.96	16.18	0.04	bdl	0.29	0.03	9.28	0.14	bdl	99.91	Albitite
zw001-2-5-2	69.04	19.07	0.04	bdl	0.09	bdl	11.01	0.15	bdl	99.42	Albitite
zw001-2-5-3	68.72	19.24	bdl	bdl	0.26	bdl	10.94	0.15	bdl	99.32	Albitite
zw001-2-5-4	68.93	19.13	0.03	bdl	0.17	bdl	10.83	0.16	bdl	99.27	Albitite
zw001-2-5-5	69.18	19.11	0.07	bdl	0.05	bdl	11.00	0.16	bdl	99.56	Albitite
zw001-2-5-6	70.09	18.28	0.05	bdl	0.16	bdl	10.63	0.15	bdl	99.35	Albitite
zw001-2-6-1	69.21	19.05	0.10	bdl	bdl	bdl	10.88	0.19	bdl	99.44	Albitite
zw001-2-6-2	68.37	19.33	0.16	bdl	0.38	bdl	10.68	0.18	bdl	99.11	Albitite
zw001-2-6-3	68.26	19.38	0.04	bdl	0.49	bdl	10.83	0.27	bdl	99.29	Albitite
zw001-2-6-4	69.13	19.05	0.06	bdl	0.06	bdl	11.06	0.16	bdl	99.51	Albitite
zw001-2-6-5	68.97	19.06	0.03	bdl	0.10	bdl	10.98	0.18	bdl	99.31	Albitite
zw001-2-6-6	68.65	19.05	0.08	bdl	0.13	bdl	10.95	0.18	bdl	99.05	Albitite
zw001-2-6-7	68.61	19.01	0.05	bdl	0.20	bdl	10.94	0.19	bdl	99.01	Albitite
zw001-1-2-01	69.00	18.81	bdl	bdl	bdl	bdl	11.01	0.16	bdl	99.00	Albitite
zw001-1-2-2	69.30	19.02	0.07	bdl	0.09	bdl	11.12	0.15	bdl	99.75	Albitite

Table 2 A5 Raw data of chemical composition of albite by electron micro probe analysis

No.	SiO_2	Al_2O_3	FeO	MgO	CaO	BaO	Na_2O	K_2O	SrO	Total	Zone
zw001-1-2-3	68.78	19.09	bdl	bdl	0.08	bdl	10.73	0.15	bdl	98.83	Albitite
zw001-1-2-4	68.99	19.15	bdl	bdl	0.09	0.04	10.97	0.16	bdl	99.41	Albitite
zw001-1-2-5	68.86	19.00	bdl	bdl	bdl	bdl	10.57	0.23	bdl	98.66	Albitite
zw001-1-2-6	68.49	19.22	0.03	bdl	0.23	bdl	10.89	0.20	bdl	99.07	Albitite
zw001-1-2-7	68.76	19.22	bdl	bdl	0.35	bdl	10.76	0.20	bdl	99.31	Albitite
zw001-1-2-8	68.91	19.15	0.03	bdl	0.11	0.03	10.93	0.17	bdl	99.32	Albitite
Avg.	68.86	19.12	0.06	/	0.27	0.03	10.87	0.18	0.06	99.32	
St. dev	0.74	0.43	0.04	/	0.18	0.01	0.26	0.03	0.04	0.30	
zw001-2-10-3	67.92	19.69	bdl	bdl	0.97	bdl	10.48	0.24	bdl	99.31	Rhyolite 1
zw001-2-10-2	68.34	19.20	0.04	bdl	0.51	bdl	10.79	0.15	bdl	99.02	Rhyolite 1
zw001-2-10-1	68.81	19.00	0.20	bdl	0.03	bdl	10.61	0.32	bdl	99.00	Rhyolite 1
zw001-2-10-6	68.59	19.08	0.04	bdl	0.24	bdl	10.90	0.18	bdl	99.03	Rhyolite 1
zw001-2-11-1	68.69	18.99	bdl	bdl	0.19	bdl	11.02	0.21	bdl	99.14	Rhyolite 1
zw001-2-11-2	68.79	19.12	0.03	bdl	0.09	bdl	10.93	0.17	bdl	99.13	Rhyolite 1
zw001-2-11-3	69.23	18.90	bdl	bdl	bdl	0.04	11.05	0.16	bdl	99.40	Rhyolite 1
zw001-2-11-4	68.88	19.05	0.03	bdl	0.07	0.04	11.12	0.18	bdl	99.37	Rhyolite 1
zw001-2-11-5	68.97	19.05	0.06	bdl	0.04	bdl	10.83	0.18	bdl	99.17	Rhyolite 1
zw001-2-11-6	68.79	19.13	0.03	bdl	0.17	bdl	10.80	0.18	0.04	99.13	Rhyolite 1
zw001-2-12-1	68.98	18.80	bdl	bdl	bdl	bdl	11.04	0.19	bdl	99.02	Rhyolite 1
zw001-2-12-2	68.88	18.98	0.05	bdl	0.04	bdl	10.99	0.14	bdl	99.07	Rhyolite 1
zw001-2-12-4	68.73	19.04	0.04	bdl	0.03	bdl	11.02	0.17	bdl	99.03	Rhyolite 1
zw001-2-12-5	68.58	19.16	0.09	bdl	0.10	bdl	10.86	0.16	bdl	98.99	Rhyolite 1
zw001-2-12-7	68.95	18.89	bdl	bdl	0.09	bdl	10.93	0.15	bdl	99.02	Rhyolite 1
zw001-2-12-8	69.01	19.02	bdl	bdl	0.08	bdl	10.81	0.12	bdl	99.06	Rhyolite 1
zw001-2-12-9	68.72	19.00	0.05	bdl	bdl	0.05	11.06	0.16	bdl	99.06	Rhyolite 1
zw001-2-13-2	68.64	18.93	0.05	bdl	0.07	bdl	11.06	0.15	0.10	99.02	Rhyolite 1
zw001-2-13-3	68.95	19.23	0.05	bdl	0.16	bdl	11.12	0.15	bdl	99.67	Rhyolite 1
zw001-2-13-4	68.91	18.93	0.09	bdl	bdl	0.03	10.98	0.19	0.04	99.16	Rhyolite 1
zw001-2-13-5	69.14	19.10	0.03	bdl	0.03	bdl	11.09	0.19	bdl	99.59	Rhyolite 1
zw001-2-13-6	69.18	18.89	0.05	bdl	0.06	bdl	11.04	0.18	bdl	99.41	Rhyolite 1
zw001-2-20-1	68.93	19.39	0.03	bdl	0.28	bdl	11.06	0.14	bdl	99.83	Rhyolite 1
zw001-2-20-2	67.61	18.79	0.03	bdl	1.86	bdl	11.07	0.16	bdl	99.49	Rhyolite 1
zw001-2-20-4	69.09	18.97	0.07	bdl	0.07	bdl	10.91	0.15	bdl	99.28	Rhyolite 1
zw001-2-20-5	68.55	19.50	0.03	bdl	0.22	bdl	10.91	0.16	bdl	99.37	Rhyolite 1
zw001-2-20-6	69.18	19.18	bdl	bdl	0.24	bdl	10.94	0.17	bdl	99.72	Rhyolite 1
zw001-2-20-7	68.90	19.19	0.03	bdl	0.16	0.05	11.02	0.16	bdl	99.51	Rhyolite 1
zw001-2-20-8	69.17	19.16	bdl	bdl	0.16	bdl	10.99	0.15	bdl	99.63	Rhyolite 1
zw001-2-21-1	69.08	19.05	0.07	bdl	0.03	bdl	11.11	0.22	bdl	99.57	Rhyolite 1
zw001-2-21-2	68.91	19.07	0.05	bdl	0.06	bdl	11.14	0.21	bdl	99.44	Rhyolite 1
zw001-2-21-3	69.21	19.07	0.03	bdl	0.09	bdl	10.79	0.16	bdl	99.34	Rhyolite 1
zw001-2-21-4	69.04	18.90	bdl	bdl	0.06	bdl	10.99	0.18	bdl	99.18	Rhyolite 1
zw001-2-21-5	69.19	19.13	0.05	bdl	0.06	0.03	10.97	0.16	bdl	99.59	Rhyolite 1
zw001-2-21-6	69.17	19.02	0.05	bdl	0.03	0.01	10.99	0.17	bdl	99.43	Rhyolite 1
Avg.	68.85	19.07	0.05	/	0.20	0.03	10.95	0.17	0.06	99.29	
St. dev	0.35	0.18	0.04	/	0.36	0.01	0.14	0.04	0.04	0.25	

Table 2 A5 Raw data of chemical composition of albite by electron micro probe analysis

No.	SiO_2	Al_2O_3	FeO	MgO	CaO	BaO	Na_2O	K_2O	SrO	Total	Zone
zw001-4-14-1	68.98	19.02	0.12	bdl	0.05	bdl	11.09	0.20	bdl	99.47	Rhyolite 2
zw001-4-14-2	68.94	19.37	0.03	bdl	0.26	bdl	11.12	0.15	bdl	99.86	Rhyolite 2
zw001-4-14-3	69.42	19.07	bdl	bdl	0.07	0.04	10.95	0.16	bdl	99.71	Rhyolite 2
zw001-4-14-4	68.65	19.57	bdl	bdl	0.50	bdl	10.86	0.17	bdl	99.78	Rhyolite 2
zw001-4-15-2	69.02	19.08	0.06	bdl	0.03	bdl	10.79	0.19	bdl	99.18	Rhyolite 2
zw001-4-15-3	67.00	20.28	0.04	bdl	1.23	bdl	10.41	0.15	bdl	99.11	Rhyolite 2
zw001-4-15-4	69.09	19.30	bdl	bdl	0.24	0.04	11.06	0.17	bdl	99.92	Rhyolite 2
zw001-4-15-5	66.80	21.81	bdl	bdl	0.09	0.04	10.39	0.14	bdl	99.30	Rhyolite 2
zw001-4-15-6	69.13	19.11	0.09	bdl	0.10	bdl	10.79	0.23	bdl	99.47	Rhyolite 2
zw001-4-16-1	68.51	19.17	0.03	bdl	0.18	bdl	11.01	0.14	bdl	99.04	Rhyolite 2
zw001-4-16-2	68.70	19.24	0.05	bdl	0.14	bdl	10.79	0.18	bdl	99.10	Rhyolite 2
zw001-4-16-3	68.74	19.07	bdl	bdl	0.33	bdl	10.93	0.15	bdl	99.24	Rhyolite 2
zw001-4-16-4	68.87	19.17	0.03	bdl	0.22	bdl	10.81	0.16	bdl	99.26	Rhyolite 2
zw001-4-16-5	68.89	19.05	0.04	bdl	0.13	bdl	10.79	0.15	bdl	99.06	Rhyolite 2
zw001-4-17-1	69.05	19.07	0.03	bdl	0.14	bdl	11.12	0.15	bdl	99.56	Rhyolite 2
zw001-4-17-2	69.00	18.91	bdl	bdl	0.11	bdl	11.12	0.21	bdl	99.36	Rhyolite 2
zw001-4-17-3	68.83	18.96	0.03	bdl	0.10	bdl	11.01	0.16	bdl	99.09	Rhyolite 2
zw001-4-17-4	68.68	19.10	0.05	bdl	0.18	bdl	10.84	0.18	bdl	99.02	Rhyolite 2
zw001-4-17-5	68.70	19.09	0.04	bdl	0.23	bdl	10.89	0.15	bdl	99.10	Rhyolite 2
zw001-4-17-6	69.23	18.91	0.03	bdl	0.04	0.04	10.91	0.15	bdl	99.31	Rhyolite 2
zw001-4-17-7	68.96	19.11	0.04	bdl	0.12	0.03	11.07	0.13	bdl	99.47	Rhyolite 2
zw001-4-18-1	68.57	19.37	bdl	bdl	0.44	bdl	10.81	0.16	bdl	99.39	Rhyolite 2
zw001-4-18-2	68.86	19.11	0.06	bdl	0.22	bdl	10.81	0.16	bdl	99.21	Rhyolite 2
zw001-4-18-3	69.08	18.91	bdl	bdl	0.09	bdl	10.95	0.18	bdl	99.23	Rhyolite 2
zw001-4-18-4	68.86	19.05	0.03	bdl	0.15	bdl	10.88	0.17	bdl	99.13	Rhyolite 2
zw001-4-18-5	68.87	18.98	0.03	bdl	bdl	bdl	10.99	0.20	bdl	99.08	Rhyolite 2
zw001-4-19-1	68.28	18.98	0.03	bdl	0.15	bdl	11.12	0.18	bdl	98.74	Rhyolite 2
zw001-4-19-2	68.99	19.06	0.06	bdl	0.04	bdl	11.09	0.17	bdl	99.42	Rhyolite 2
zw001-4-19-3	69.02	19.09	0.07	bdl	0.16	bdl	11.16	0.15	bdl	99.64	Rhyolite 2
zw001-4-19-4	68.71	19.19	0.11	bdl	0.19	0.04	10.87	0.23	bdl	99.33	Rhyolite 2
zw001-4-19-5	68.58	19.25	0.04	bdl	0.44	bdl	10.57	0.21	bdl	99.09	Rhyolite 2
zw001-4-19-6	68.42	19.11	0.07	bdl	0.40	0.04	10.65	0.18	bdl	98.86	Rhyolite 2
zw001-4-19-7	69.29	18.92	0.06	bdl	0.03	0.03	10.78	0.16	bdl	99.28	Rhyolite 2
zw001-2-14-1	68.97	18.97	bdl	bdl	0.06	0.03	10.98	0.17	bdl	99.20	Rhyolite 2
zw001-2-14-2	69.16	19.01	bdl	bdl	0.04	bdl	10.92	0.19	bdl	99.34	Rhyolite 2
zw001-2-14-3	69.19	18.87	bdl	bdl	0.06	bdl	11.20	0.20	bdl	99.54	Rhyolite 2
zw001-2-14-4	69.23	18.97	0.07	bdl	bdl	0.04	11.30	0.16	bdl	99.78	Rhyolite 2
zw001-2-14-5	69.04	19.05	bdl	bdl	bdl	bdl	11.01	0.17	bdl	99.30	Rhyolite 2
zw001-2-14-6	68.99	18.84	0.05	bdl	bdl	bdl	11.00	0.16	0.05	99.09	Rhyolite 2
zw001-4-20-1	68.98	19.02	0.13	bdl	0.03	bdl	11.19	0.11	bdl	99.50	Rhyolite 2
zw001-4-20-2	68.94	18.87	0.03	bdl	bdl	bdl	11.15	0.06	bdl	99.06	Rhyolite 2
zw001-4-20-3	68.80	18.90	bdl	bdl	0.05	bdl	11.25	0.09	bdl	99.10	Rhyolite 2
zw001-4-20-4	68.99	18.87	0.05	bdl	bdl	bdl	11.09	0.08	bdl	99.10	Rhyolite 2
zw001-4-20-7	68.71	18.85	0.04	bdl	0.03	0.03	10.71	0.09	bdl	98.45	Rhyolite 2
zw001-4-20-8	68.78	18.95	0.05	bdl	bdl	bdl	11.07	0.11	bdl	98.97	Rhyolite 2

Table 2 A5 Raw data of chemical composition of albite by electron micro probe analysis

No.	SiO_2	Al_2O_3	FeO	MgO	CaO	BaO	Na_2O	K_2O	SrO	Total	Zone
zw001-4-21-1	68.81	18.88	bdl	bdl	0.10	0.05	11.08	0.16	bdl	99.09	Rhyolite 2
zw001-4-21-2	68.84	18.90	0.03	bdl	0.06	bdl	11.23	0.17	bdl	99.25	Rhyolite 2
zw001-4-21-3	68.71	18.98	bdl	bdl	0.11	bdl	11.05	0.14	bdl	99.00	Rhyolite 2
zw001-4-21-4	68.68	19.14	0.04	bdl	0.30	bdl	10.98	0.16	bdl	99.30	Rhyolite 2
zw001-4-21-5	68.94	19.01	0.03	bdl	0.06	bdl	11.05	0.19	bdl	99.28	Rhyolite 2
zw001-4-21-6	68.97	18.83	0.07	bdl	0.13	0.03	11.08	0.15	bdl	99.26	Rhyolite 2
zw001-4-21-7	69.53	19.08	0.03	bdl	0.03	0.03	11.07	0.10	bdl	99.86	Rhyolite 2
Avg.	68.83	19.12	0.05	/	0.17	0.04	10.96	0.16	0.05	99.27	
St. dev	0.45	0.44	0.03	/	0.20	0.01	0.19	0.03	0.00	0.28	

Table 2 A6 Raw data of chemical composition of Mica by electron micro probe analysis

No.	SiO_2	TiO_2	Al_2O_3	FeO	MnO	MgO	Na_2O	K_2O	SnO_2	F	Total	Zone
zw001-01-97	41.48	0.77	20.13	19.38	0.36	0.39	0.07	9.82	bdl	4.14	94.78	Greisen
zw001-01-99	42.98	0.59	21.36	17.94	0.35	0.50	0.06	9.40	bdl	4.51	95.79	Greisen
zw001-01-100	41.27	0.74	20.02	19.51	0.43	0.30	0.08	9.59	bdl	5.28	94.98	Greisen
zw001-01-94	41.07	0.74	20.33	20.09	0.35	0.34	0.07	9.20	bdl	3.96	94.51	Greisen
zw001-01-95	41.34	0.73	20.11	19.19	0.41	0.32	0.10	9.63	bdl	4.78	94.59	Greisen
zw001-01-96	40.99	0.81	19.98	19.98	0.41	0.35	0.11	9.62	bdl	4.96	95.12	Greisen
zw001-01-89	40.36	0.99	19.56	21.40	0.36	0.58	bdl	9.15	bdl	4.31	94.90	Greisen
zw001-01-90	41.15	1.34	20.31	21.28	0.27	0.81	0.03	9.27	bdl	2.68	96.02	Greisen
zw001-01-91	39.54	1.56	19.52	22.47	0.36	0.60	0.12	9.45	bdl	2.55	95.09	Greisen
zw001-01-92	38.88	1.44	18.61	24.28	0.44	0.57	0.12	9.39	bdl	3.32	95.68	Greisen
avg.	40.90	0.97	19.99	20.55	0.37	0.48	0.08	9.45	/	4.05	95.15	
std. dv	1.12	0.35	0.70	1.84	0.05	0.16	0.03	0.21	/	0.93	0.52	
zw001-01-83	40.05	0.91	19.85	21.97	0.37	0.60	0.07	9.62	bdl	3.56	95.50	Albitite
zw001-01-84	39.34	0.89	19.03	22.29	0.40	0.65	0.04	9.47	0.03	4.14	94.51	Albitite
zw001-01-85	38.72	0.60	18.67	23.93	0.41	0.76	0.14	9.73	bdl	5.00	95.85	Albitite
zw001-01-86	39.87	0.67	19.78	21.57	0.37	0.51	0.15	9.68	bdl	4.61	95.28	Albitite
zw001-01-87	39.61	0.62	19.52	21.82	0.38	0.75	0.12	9.72	bdl	4.24	95.01	Albitite
zw001-01-79	40.33	1.01	20.35	19.81	0.36	0.60	0.09	9.63	bdl	4.41	94.74	Albitite
zw001-01-81	42.35	0.49	20.47	17.96	0.33	0.75	0.15	9.20	bdl	5.58	94.94	Albitite
zw001-01-82	40.53	0.81	20.31	20.28	0.39	0.62	0.03	9.08	bdl	4.45	94.62	Albitite
zw001-01-75	39.76	1.16	19.06	22.66	0.37	0.59	0.09	9.54	bdl	3.44	95.24	Albitite
zw001-01-77	42.24	0.47	20.13	18.46	0.38	0.48	0.12	9.29	bdl	5.88	94.97	Albitite
zw001-01-70	40.81	0.70	19.76	20.18	0.37	0.51	0.10	9.27	bdl	5.38	94.81	Albitite
zw001-01-73	39.21	1.10	19.19	22.66	0.39	0.64	0.07	9.76	bdl	3.49	95.03	Albitite
zw001-02-2	40.28	0.91	19.16	21.22	0.36	0.39	0.05	9.33	bdl	5.36	94.80	Albitite
zw001-02-3	39.71	1.04	19.12	21.87	0.36	0.46	0.09	9.52	bdl	4.38	94.70	Albitite
zw001-02-4	39.90	0.96	19.40	21.52	0.40	0.49	0.05	9.62	bdl	4.16	94.76	Albitite
zw001-02-6	38.84	1.51	18.46	23.83	0.40	0.56	0.05	9.78	bdl	3.08	95.21	Albitite
zw001-02-12	39.40	1.15	19.36	22.14	0.33	0.87	0.08	9.62	bdl	2.92	94.64	Albitite
avg.	40.06	0.88	19.51	21.42	0.37	0.60	0.09	9.52	/	4.36	94.98	
std.dv	1.01	0.27	0.59	1.65	0.02	0.13	0.04	0.21	/	0.88	0.35	
zw001-02-23	40.03	1.08	18.99	21.27	0.29	1.11	0.11	9.59	bdl	4.97	95.35	Rhyolite
zw001-02-25	39.12	1.04	18.48	22.58	0.31	1.08	0.09	9.47	bdl	4.91	95.01	Rhyolite
zw001-02-26	38.13	1.54	17.95	24.09	0.33	1.22	0.07	9.62	bdl	3.79	95.14	Rhyolite
zw001-02-27	40.84	1.01	19.25	21.07	0.30	1.12	0.03	9.70	bdl	5.10	96.30	Rhyolite
zw001-02-28	38.27	1.27	18.02	24.07	0.33	1.25	0.15	9.59	bdl	4.39	95.49	Rhyolite
zw001-02-29	39.46	1.24	18.57	21.89	0.32	1.24	0.11	9.41	bdl	4.80	95.00	Rhyolite
zw001-02-19	38.11	1.57	17.67	26.03	0.32	1.31	0.19	9.58	0.05	2.98	96.55	Rhyolite
zw001-02-33	36.81	5.98	17.40	22.95	0.28	1.27	0.10	8.71	bdl	3.27	95.38	Rhyolite
zw001-02-34	39.76	1.20	20.13	22.56	0.25	1.14	bdl	9.33	bdl	2.45	95.81	Rhyolite
zw001-02-35	39.67	0.89	18.91	21.03	0.31	1.14	0.14	9.81	bdl	4.96	94.77	Rhyolite
zw001-02-36	41.57	0.59	20.40	18.42	0.33	0.72	0.09	9.78	bdl	4.55	94.54	Rhyolite
zw001-02-38	42.66	0.87	21.24	17.38	0.31	0.56	0.10	9.53	bdl	4.13	95.03	Rhyolite

Table 2 A6 Raw data of chemical composition of Mica by electron micro probe analysis

No.	SiO_2	TiO_2	Al_2O_3	FeO	MnO	MgO	Na_2O	K_2O	SnO_2	F	Total	Zone
zw001-02-41	41.41	0.94	19.80	19.85	0.41	0.44	0.07	9.76	bdl	5.16	95.66	Rhyolite
zw001-02-51	41.35	0.95	19.62	19.41	0.43	0.45	0.14	9.48	bdl	5.19	94.83	Rhyolite
zw001-02-52	41.71	0.85	20.00	18.62	0.41	0.45	0.14	9.50	bdl	5.28	94.74	Rhyolite
zw001-02-53	41.45	0.98	19.90	19.34	0.39	0.44	0.08	9.72	bdl	4.25	94.75	Rhyolite
zw001-02-56	41.25	1.02	19.96	19.77	0.39	0.47	0.08	9.41	bdl	5.02	95.26	Rhyolite
zw001-02-57	43.10	0.56	21.42	16.44	0.26	0.76	0.11	9.48	bdl	4.14	94.55	Rhyolite
zw001-02-58	41.47	0.79	20.26	19.13	0.32	0.55	0.08	9.74	bdl	4.74	95.09	Rhyolite
zw001-02-59	41.63	0.71	20.48	18.54	0.30	0.70	0.10	9.73	bdl	4.25	94.65	Rhyolite
zw001-02-60	41.58	0.80	20.36	19.29	0.35	0.50	0.10	9.66	bdl	4.38	95.18	Rhyolite
zw001-02-62	43.00	0.51	20.89	17.67	0.30	0.67	0.08	9.60	bdl	4.53	95.34	Rhyolite
zw001-02-63	42.30	0.86	20.17	18.25	0.36	0.32	0.03	9.45	bdl	5.52	94.93	Rhyolite
zw001-02-64	42.97	0.81	20.71	17.51	0.33	0.45	0.09	9.28	bdl	4.68	94.86	Rhyolite
zw001-02-68	42.07	0.72	20.27	18.62	0.37	0.67	0.12	9.76	bdl	5.62	95.85	Rhyolite
avg.	40.79	1.15	19.63	20.23	0.33	0.80	0.10	9.55	/	4.52	95.20	
std.dv	1.72	1.04	1.12	2.44	0.05	0.34	0.04	0.23	/	0.77	0.52	

Table 2 A7 Raw data of chemical composition of K-feldspar by electron micro probe analysis

No.	SiO_2	Al_2O_3	FeO	CaO	BaO	Na_2O	K_2O	SrO	Total (%)	Zone
zw001-1-kfs1-1	45.879	38.995	0.56	bdl	bdl	0.038	4.723	bdl	90.61	Greisen
zw001-1-kfs1-2	48.397	35.846	0.745	bdl	bdl	0.03	6.862	bdl	92.435	Greisen
zw001-1-kfs1-3	42.608	42.701	0.422	bdl	0.042	bdl	1.984	bdl	88.124	Greisen
zw001-1-kfs1-4	41.337	42.588	0.383	bdl	bdl	bdl	1.396	bdl	86.168	Greisen
zw001-1-kfs1-5	45.716	38.251	0.63	bdl	bdl	bdl	4.852	bdl	89.859	Greisen
zw001-1-kfs1-6	47.563	38.001	0.736	bdl	0.041	0.047	4.683	bdl	91.502	Greisen
zw001-1-kfs1-7	46.716	39.733	0.629	bdl	0.034	bdl	4.13	0.072	92.056	Greisen
zw001-1-kfs2-8	45.291	39.58	0.585	bdl	bdl	bdl	3.838	bdl	89.751	Greisen
zw001-1-kfs2-9	43.574	40.097	0.563	bdl	bdl	0.053	3.698	bdl	88.373	Greisen
zw001-1-kfs2-10	43.999	42.496	0.521	bdl	bdl	bdl	1.919	0.078	89.419	Greisen
Avg.	45.11	39.83	0.58	bdl	0.04	0.04	3.81	0.08	89.83	
St. dev.	2.22	2.25	0.12	bdl	0.00	0.01	1.66	0.00	1.94	
zw001-1-1-01	65.09	17.90	bdl	bdl	0.08	0.58	15.98	bdl	99.64	Albitite
zw001-1-1-02	65.11	17.94	bdl	bdl	0.10	0.86	15.73	0.11	99.86	Albitite
zw001-1-1-4	65.48	17.98	0.04	bdl	0.05	0.92	15.69	bdl	100.16	Albitite
zw001-1-1-5	65.11	17.82	bdl	bdl	0.03	0.73	15.80	bdl	99.52	Albitite
zw001-1-1-6	64.79	18.02	bdl	bdl	0.21	0.39	16.39	bdl	99.82	Albitite
zw001-1-1-7	65.00	17.90	0.03	bdl	0.09	0.64	15.97	bdl	99.63	Albitite
zw001-1-3-14	65.09	17.92	0.03	bdl	0.09	0.20	16.55	bdl	99.86	Albitite
zw001-1-3-15	64.98	17.92	bdl	bdl	0.09	0.30	16.57	bdl	99.87	Albitite
zw001-1-3-16	65.31	17.84	0.05	bdl	0.07	0.57	16.04	bdl	99.88	Albitite
zw001-1-3-17	65.45	17.90	bdl	bdl	0.05	0.83	15.68	bdl	99.94	Albitite
zw001-1-3-18	65.43	17.76	bdl	bdl	bdl	0.61	16.00	bdl	99.82	Albitite
zw001-1-3-19	64.95	17.81	bdl	bdl	0.04	0.58	16.03	bdl	99.44	Albitite
zw001-1-4-11	65.33	17.90	0.06	bdl	0.03	0.93	15.73	bdl	100.02	Albitite
zw001-1-4-12	64.86	18.01	bdl	bdl	0.09	0.46	16.26	bdl	99.69	Albitite
zw001-1-4-13	64.96	17.85	bdl	bdl	0.07	0.28	16.57	bdl	99.74	Albitite
zw001-1-4-14	65.16	17.98	bdl	bdl	0.05	0.35	16.46	bdl	100.01	Albitite
zw001-1-4-15	65.10	17.80	bdl	bdl	0.03	0.32	16.57	bdl	99.81	Albitite
zw001-1-4-16	64.70	17.78	bdl	bdl	0.11	0.19	16.56	bdl	99.34	Albitite
zw001-1-5-7	65.31	17.98	bdl	bdl	0.04	0.93	15.55	bdl	99.83	Albitite
zw001-1-5-8	65.27	17.84	0.04	bdl	0.08	0.86	15.63	bdl	99.71	Albitite
zw001-1-5-11	65.17	17.98	0.03	bdl	bdl	0.87	15.73	bdl	99.79	Albitite
zw001-2-3-9	64.88	17.92	0.05	bdl	0.14	0.39	16.33	bdl	99.71	Albitite
zw001-2-3-10	64.90	18.04	0.06	bdl	0.27	0.24	16.53	bdl	100.06	Albitite
zw001-2-3-11	65.27	17.95	0.04	bdl	0.19	0.83	15.71	bdl	99.99	Albitite
zw001-2-3-12	65.21	18.04	bdl	bdl	0.29	0.81	15.57	0.06	99.99	Albitite
zw001-2-3-13	65.13	18.06	bdl	bdl	0.31	0.34	16.30	bdl	100.15	Albitite
zw001-2-3-14	64.92	18.11	bdl	bdl	0.17	0.66	15.90	bdl	99.76	Albitite
zw001-2-3-15	64.98	17.85	bdl	bdl	0.19	0.85	15.68	bdl	99.58	Albitite
zw001-2-3-17	64.94	17.98	0.10	bdl	0.20	0.39	16.38	bdl	99.97	Albitite
Avg.	65.10	17.92	0.05	bdl	0.12	0.58	16.06	0.09	99.81	
St. dev.	0.20	0.09	0.02	bdl	0.08	0.25	0.36	0.03	0.20	

Table 2 A7 Raw data of chemical composition of K-feldspar by electron micro probe analysis

No.	SiO_2	Al_2O_3	FeO	CaO	BaO	Na_2O	K_2O	SrO	Total (%)	Zone
zw001-2-7-1	65.14	17.89	0.05	bdl	0.16	0.98	15.44	bdl	99.67	Rhyolite 1
zw001-2-7-2	65.16	17.91	bdl	bdl	0.13	0.70	15.95	bdl	99.84	Rhyolite 1
zw001-2-7-3	65.38	18.01	0.05	bdl	0.14	0.87	15.64	bdl	100.08	Rhyolite 1
zw001-2-7-8	65.16	17.81	0.09	bdl	0.03	0.93	15.72	bdl	99.74	Rhyolite 1
zw001-2-7-11	65.42	18.03	0.03	bdl	0.11	0.94	15.66	bdl	100.18	Rhyolite 1
zw001-2-7-13	64.99	17.91	0.03	bdl	0.11	0.71	15.87	bdl	99.63	Rhyolite 1
zw001-2-7-14	65.20	17.98	0.03	bdl	0.06	0.96	15.47	bdl	99.69	Rhyolite 1
zw001-2-7-15	65.21	17.89	0.05	bdl	0.08	0.91	15.62	bdl	99.76	Rhyolite 1
zw001-2-7-16	64.71	17.79	0.06	bdl	0.07	0.72	15.72	0.08	99.13	Rhyolite 1
zw001-2-8-1	65.18	17.99	0.03	bdl	0.23	0.78	15.75	bdl	99.96	Rhyolite 1
zw001-2-8-2	64.96	18.04	0.06	bdl	0.36	0.83	15.57	bdl	99.81	Rhyolite 1
zw001-2-8-3	65.24	18.17	0.05	bdl	0.26	1.01	15.30	bdl	100.04	Rhyolite 1
zw001-2-8-4	64.93	18.11	bdl	bdl	0.34	0.93	15.54	bdl	99.85	Rhyolite 1
zw001-2-8-7	65.41	18.25	bdl	bdl	0.47	0.91	15.47	bdl	100.53	Rhyolite 1
zw001-2-8-8	65.14	18.30	0.10	bdl	0.31	1.04	15.22	bdl	100.11	Rhyolite 1
zw001-2-9-1	65.16	17.77	0.07	bdl	bdl	0.98	15.63	bdl	99.63	Rhyolite 1
zw001-2-9-2	64.86	17.96	0.04	bdl	0.10	0.82	15.77	bdl	99.54	Rhyolite 1
zw001-2-9-3	65.20	17.83	0.09	bdl	0.05	0.93	15.68	0.05	99.83	Rhyolite 1
zw001-2-9-4	64.65	17.93	0.04	bdl	0.27	0.87	15.65	bdl	99.41	Rhyolite 1
zw001-2-9-7	65.42	17.95	0.12	bdl	0.04	1.18	15.25	bdl	99.96	Rhyolite 1
zw001-2-9-9	64.89	17.93	0.03	bdl	0.08	0.94	15.56	bdl	99.42	Rhyolite 1
zw001-2-9-10	65.12	17.97	0.06	bdl	0.07	1.07	15.45	bdl	99.74	Rhyolite 1
zw001-2-9-11	65.18	17.81	0.05	bdl	0.09	0.92	15.71	bdl	99.75	Rhyolite 1
zw001-2-9-12	65.12	17.96	0.07	bdl	0.04	0.92	15.77	bdl	99.87	Rhyolite 1
zw001-2-9-13	65.08	17.69	0.06	bdl	0.03	0.82	15.69	bdl	99.36	Rhyolite 1
zw001-2-9-14	65.26	17.82	0.08	bdl	0.03	0.90	15.80	0.04	99.92	Rhyolite 1
zw001-2-9-15	64.81	17.81	0.08	bdl	bdl	0.96	15.74	0.04	99.44	Rhyolite 1
zw001-2-9-16	65.37	17.83	0.10	bdl	bdl	0.90	15.74	bdl	99.95	Rhyolite 1
zw001-2-9-17	65.23	17.96	0.05	bdl	bdl	0.78	15.74	bdl	99.75	Rhyolite 1
zw001-2-10-8	65.16	17.78	0.08	bdl	bdl	0.91	15.79	0.08	99.79	Rhyolite 1
zw001-2-10-9	65.31	17.80	0.08	bdl	bdl	0.95	15.61	0.09	99.85	Rhyolite 1
zw001-2-10-10	65.32	17.79	0.10	bdl	0.08	1.09	15.41	bdl	99.79	Rhyolite 1
zw001-2-10-11	64.97	17.90	0.07	bdl	0.04	0.85	15.65	0.08	99.55	Rhyolite 1
zw001-2-15-1	64.89	17.91	0.08	bdl	bdl	0.99	15.39	bdl	99.28	Rhyolite 1
zw001-2-15-4	64.89	17.90	0.06	bdl	0.06	1.05	15.36	0.04	99.36	Rhyolite 1
zw001-2-15-5	64.84	17.76	0.07	bdl	0.05	0.59	15.99	bdl	99.30	Rhyolite 1
zw001-2-15-6	64.91	17.87	0.05	bdl	0.03	0.86	15.76	0.04	99.51	Rhyolite 1
zw001-2-15-7	65.05	17.87	0.10	bdl	0.04	1.03	15.34	bdl	99.42	Rhyolite 1
zw001-2-15-8	65.22	17.96	0.09	bdl	bdl	1.08	15.34	0.13	99.83	Rhyolite 1
zw001-2-15-9	65.03	17.94	0.09	bdl	bdl	1.19	15.29	bdl	99.57	Rhyolite 1
zw001-2-16-5	64.70	17.98	0.05	bdl	0.34	0.78	15.70	bdl	99.55	Rhyolite 1
zw001-2-16-9	64.85	18.03	0.06	bdl	0.30	0.94	15.54	0.03	99.74	Rhyolite 1
zw001-2-17-1	65.83	18.02	0.07	bdl	bdl	0.94	15.58	bdl	100.44	Rhyolite 1
zw001-2-17-3	65.28	18.12	0.04	bdl	bdl	0.97	15.60	bdl	100.01	Rhyolite 1
zw001-2-17-4	65.25	18.04	0.11	bdl	bdl	0.93	15.66	bdl	99.98	Rhyolite 1

Table 2 A7 Raw data of chemical composition of K-feldspar by electron micro probe analysis

No.	SiO_2	Al_2O_3	FeO	CaO	BaO	Na_2O	K_2O	SrO	Total (%)	Zone
zw001-2-17-5	65.32	17.87	0.06	bdl	0.05	0.89	15.73	0.12	100.03	Rhyolite 1
zw001-2-17-6	65.35	17.94	0.07	bdl	0.07	0.97	15.54	bdl	99.94	Rhyolite 1
zw001-2-17-7	65.44	18.06	0.08	bdl	0.03	0.96	15.51	bdl	100.08	Rhyolite 1
zw001-2-17-8	65.03	17.96	0.07	bdl	0.03	0.94	15.69	bdl	99.71	Rhyolite 1
zw001-2-17-9	65.15	17.96	0.08	bdl	bdl	1.08	15.53	0.03	99.85	Rhyolite 1
zw001-2-17-10	65.20	17.94	0.09	bdl	0.04	0.70	15.89	bdl	99.85	Rhyolite 1
zw001-2-17-11	65.25	17.78	0.07	bdl	bdl	0.79	15.70	bdl	99.59	Rhyolite 1
zw001-2-17-12	65.50	17.92	0.09	bdl	bdl	0.91	15.72	bdl	100.15	Rhyolite 1
zw001-2-14-7	65.30	17.79	0.06	bdl	0.03	0.59	16.05	bdl	99.80	Rhyolite 1
zw001-2-14-8	65.50	17.93	0.06	bdl	0.09	0.99	15.61	bdl	100.18	Rhyolite 1
zw001-2-14-9	65.46	17.92	0.09	bdl	bdl	0.85	15.81	bdl	100.13	Rhyolite 1
zw001-2-14-11	65.07	17.80	0.07	bdl	0.07	0.61	15.92	0.04	99.59	Rhyolite 1
zw001-2-18-1	65.39	17.97	0.07	bdl	bdl	0.99	15.56	0.06	100.04	Rhyolite 1
zw001-2-18-2	65.67	17.93	0.07	bdl	bdl	0.94	15.57	bdl	100.18	Rhyolite 1
zw001-2-18-3	65.52	17.89	0.05	bdl	bdl	0.93	15.64	bdl	100.04	Rhyolite 1
zw001-2-18-4	65.45	17.96	0.07	bdl	bdl	0.88	15.72	bdl	100.09	Rhyolite 1
zw001-2-18-5	65.18	17.84	0.07	bdl	bdl	1.04	15.53	bdl	99.69	Rhyolite 1
zw001-2-18-7	65.48	17.89	0.04	bdl	bdl	0.94	15.57	bdl	99.93	Rhyolite 1
zw001-2-18-8	65.44	18.00	0.06	bdl	bdl	1.00	15.63	bdl	100.12	Rhyolite 1
zw001-2-19-2	65.38	18.06	0.10	bdl	0.08	1.05	15.53	bdl	100.20	Rhyolite 1
zw001-2-19-3	64.95	17.93	0.06	bdl	0.05	0.65	16.04	bdl	99.67	Rhyolite 1
Avg.	65.18	17.93	0.07	bdl	0.12	0.91	15.63	0.06	99.81	
St. dev.	0.24	0.11	0.02	bdl	0.11	0.13	0.18	0.03	0.28	
zw001-4-1-2	65.00	17.89	bdl	bdl	0.08	0.85	15.68	bdl	99.50	Rhyolite 2
zw001-4-1-4	65.10	17.91	0.03	bdl	0.05	0.69	16.03	bdl	99.82	Rhyolite 2
zw001-4-1-5	65.27	17.85	0.11	bdl	bdl	1.00	15.56	bdl	99.81	Rhyolite 2
zw001-4-1-6	65.66	18.11	0.08	bdl	0.06	1.07	15.57	bdl	100.55	Rhyolite 2
zw001-4-1-7	65.10	17.91	0.09	bdl	0.03	1.02	15.50	bdl	99.64	Rhyolite 2
zw001-4-1-8	65.15	17.96	0.05	bdl	bdl	0.94	15.60	bdl	99.71	Rhyolite 2
zw001-4-1-9	65.09	17.92	0.05	bdl	0.04	0.81	15.84	bdl	99.76	Rhyolite 2
zw001-4-2-1	65.32	17.85	0.07	bdl	0.05	0.91	15.52	bdl	99.73	Rhyolite 2
zw001-4-2-2	65.12	17.70	0.06	bdl	0.04	0.93	15.66	bdl	99.52	Rhyolite 2
zw001-4-2-4	65.40	17.82	0.07	bdl	0.03	0.94	15.49	bdl	99.74	Rhyolite 2
zw001-4-2-5	65.04	17.94	0.10	bdl	0.05	1.02	15.32	bdl	99.46	Rhyolite 2
zw001-4-2-6	65.40	18.01	0.09	bdl	0.05	1.12	15.28	bdl	99.95	Rhyolite 2
zw001-4-2-7	65.16	17.70	0.06	bdl	bdl	0.88	15.66	bdl	99.47	Rhyolite 2
zw001-4-2-8	65.54	17.91	0.06	bdl	bdl	0.84	15.66	bdl	100.04	Rhyolite 2
zw001-4-2-9	65.18	18.06	0.08	bdl	0.08	1.03	15.38	bdl	99.79	Rhyolite 2
zw001-4-2-10	65.18	17.84	0.04	bdl	bdl	0.87	15.73	bdl	99.65	Rhyolite 2
zw001-4-3-1	64.73	17.94	0.09	bdl	bdl	0.97	15.50	bdl	99.24	Rhyolite 2
zw001-4-3-2	64.65	17.92	0.06	bdl	bdl	1.05	15.40	bdl	99.11	Rhyolite 2
zw001-4-3-3	65.08	17.82	0.06	bdl	0.06	0.98	15.45	bdl	99.45	Rhyolite 2
zw001-4-3-4	65.20	17.86	0.06	bdl	bdl	1.01	15.52	bdl	99.66	Rhyolite 2
zw001-4-3-5	65.27	17.82	0.04	bdl	bdl	0.92	15.48	bdl	99.54	Rhyolite 2
zw001-4-3-6	65.16	17.87	0.06	bdl	bdl	1.12	15.36	bdl	99.58	Rhyolite 2

Table 2 A7 Raw data of chemical composition of K-feldspar by electron micro probe analysis

No.	SiO_2	Al_2O_3	FeO	CaO	BaO	Na_2O	K_2O	SrO	Total (%)	Zone
zw001-4-3-7	65.14	17.84	0.06	bdl	bdl	0.97	15.47	bdl	99.50	Rhyolite 2
zw001-4-4-2	64.94	17.91	0.10	bdl	bdl	1.02	15.49	bdl	99.48	Rhyolite 2
zw001-4-4-3	65.41	17.80	0.07	bdl	bdl	0.97	15.54	bdl	99.79	Rhyolite 2
zw001-4-4-4	65.22	18.01	0.06	bdl	bdl	0.85	15.54	bdl	99.69	Rhyolite 2
zw001-4-4-5	65.22	17.88	0.06	bdl	bdl	0.91	15.59	bdl	99.67	Rhyolite 2
zw001-4-4-7	64.89	17.89	0.07	bdl	bdl	0.85	15.74	bdl	99.47	Rhyolite 2
zw001-4-5-1	65.16	17.90	0.07	bdl	bdl	1.15	15.14	bdl	99.41	Rhyolite 2
zw001-4-5-3	65.03	17.90	0.05	bdl	bdl	1.16	15.35	bdl	99.48	Rhyolite 2
zw001-4-5-4	65.10	17.82	0.06	bdl	bdl	1.18	15.38	bdl	99.54	Rhyolite 2
zw001-4-5-5	65.18	17.88	0.06	bdl	bdl	0.84	15.85	bdl	99.81	Rhyolite 2
zw001-4-5-6	65.15	18.04	0.10	bdl	0.05	0.95	15.64	bdl	99.94	Rhyolite 2
zw001-4-5-7	64.93	17.79	0.05	bdl	0.06	1.02	15.66	bdl	99.52	Rhyolite 2
zw001-4-6-1	64.99	17.93	0.09	bdl	0.05	0.93	15.62	bdl	99.60	Rhyolite 2
zw001-4-6-2	64.96	17.96	0.08	bdl	0.06	0.85	15.58	bdl	99.49	Rhyolite 2
zw001-4-6-4	65.26	17.86	0.06	bdl	0.07	0.90	15.70	bdl	99.83	Rhyolite 2
zw001-4-6-6	65.43	17.70	0.07	bdl	bdl	0.96	15.49	bdl	99.64	Rhyolite 2
zw001-4-6-7	64.93	17.74	0.07	bdl	0.03	0.90	15.61	bdl	99.28	Rhyolite 2
zw001-4-7-1	64.75	17.79	0.08	bdl	0.05	0.96	15.46	bdl	99.09	Rhyolite 2
zw001-4-7-2	64.97	17.81	0.07	bdl	bdl	0.97	15.65	bdl	99.47	Rhyolite 2
zw001-4-7-3	65.01	17.73	0.06	bdl	bdl	0.90	15.59	bdl	99.32	Rhyolite 2
zw001-4-7-4	65.12	17.76	0.07	bdl	bdl	0.87	15.70	bdl	99.53	Rhyolite 2
zw001-4-7-5	65.04	17.68	0.06	bdl	bdl	0.93	15.64	bdl	99.36	Rhyolite 2
zw001-4-7-6	65.02	17.77	0.06	bdl	bdl	0.87	15.70	bdl	99.43	Rhyolite 2
zw001-4-7-7	65.20	17.75	0.03	bdl	0.03	0.91	15.68	bdl	99.61	Rhyolite 2
zw001-4-7-8	65.14	17.76	0.10	bdl	0.06	0.94	15.55	bdl	99.56	Rhyolite 2
Avg.	65.13	17.86	0.07		0.05	0.95	15.57	#DIV/0!	99.60	
St. dev.	0.19	0.10	0.02		0.01	0.10	0.16	#DIV/0!	0.25	

Supplementary-Chapter 4
Controls of F content and pH on the formation of greisen quantified by reactive transport modeling

Shilei Qiao [a,*], Anselm Loges [a], Johannes C. Vrijmoed [a], Timm John [a]

[a] Institut für Geologische Wissenschaften, Freie Universität Berlin, Malteserstr. 74-100, 12249 Berlin, Germany

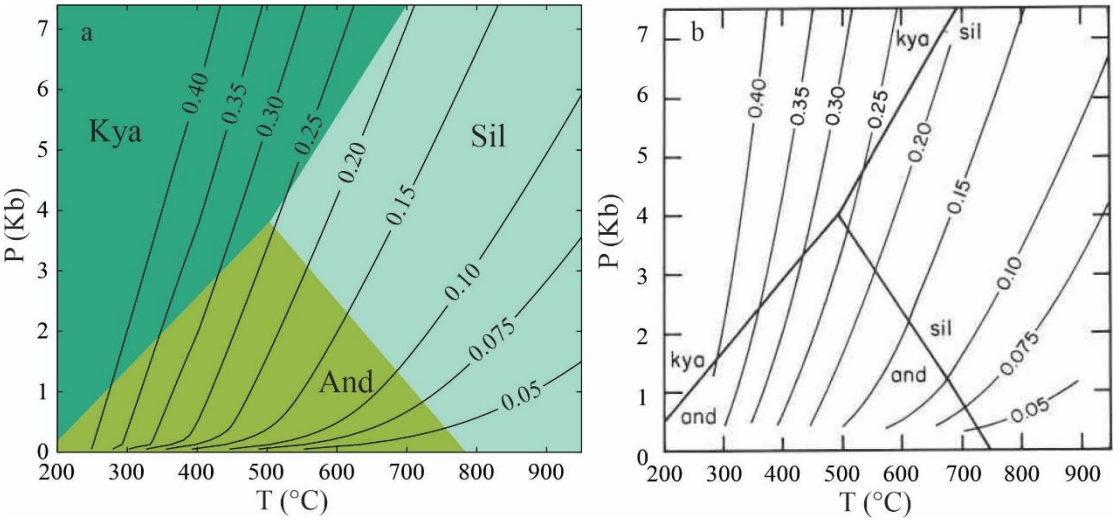

Fig. 4 A1. (a) P-T phase diagram with the isopleths of hydroxyl-topaz in the solid solution of topaz, which is benchmarked by the calculation in Barton, 1982 (b). The identical topology of these two figures indicates the solid solution topaz implied in our calculation is proper. And: andalusite; Kya: kyanite; Sil: sillimanite.

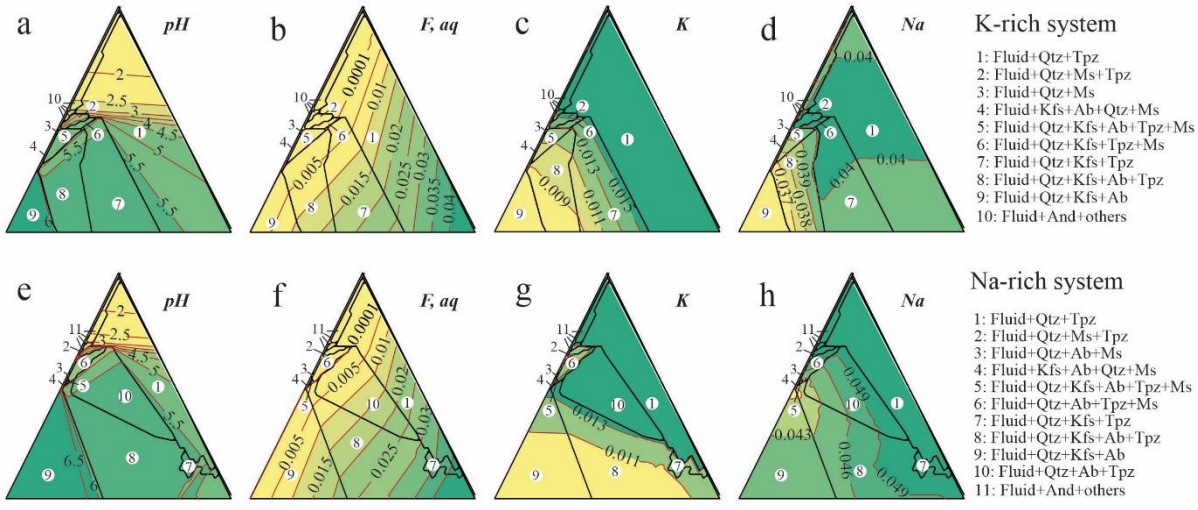

Fig. 4 A2. Phase diagram with pH, F, K and Na concentration (mol/kg) of fluid in equilibrium with the solid phase in K-rich system (a-d) and Na-rich system (e-h). Different Na and K concentration mainly

influence the stability field of albite and K-feldspar, which results in difference in mineral assemblage. However, they don't influence the stability of topaz. Values range from low to high, indicated by yellow to dark green, representing species concentration or pH levels. Ab: albite; And: andalusite; Kfs: K-feldspar; Ms: mica; Qtz: quartz; Tpz: topaz.

Matlab Code for the reactive transport modeling

Gibbs energy minizier

```
clear,clf,addpath ./Solutions ./Utilities
run_name = 'ternary_Tpz_320_15w_r150';
p = parcluster('local');
parpool(p, 28);
T = 320 + 273.15; % T in Kelvin
P = 1e8;          % P in Pascal
X1 = linspace(0,1,150);% interpret this as weight fraction HF
X2 = linspace(0,1,151);% interpret this as weight fraction HCl
[C1_2d,C2_2d] = ndgrid(X1,X2);
C3_2d        = 1-C1_2d-C2_2d;
% Names of phases to consider
phs_name = {'test4','q,tc-ds55','mic,tc-ds55','ab,tc-ds55','Topaz' ...
   'mu,tc-ds55','and,tc-ds55','syv,tc-ds55','hlt,tc-ds55','cor,tc-ds55'};
%Components in the system
Cname    = {'Si','Al','K','Na','F','Cl','H','O','e'};
%Initialize the phase data
td       = init_thermo(phs_name,Cname,'solution_models_HP98_HCl');
p                = props_generate(td); % Grid of compositions for mixtures
molm             = molmass_fun(Cname);
molm1 = [0 0 0 0 1 0 1 0 0]*molm; %HF
molm2 = [0 0 0 0 0 1 1 0 0]*molm; %HCl
molm3 = [0 0 0 0 0 0 2 1 0]*molm; %H2O
C1_mol = C1_2d/molm1; %HF in molar
```

```
C2_mol = C2_2d/molm2;
C3_mol = C3_2d/molm3;
X1_nd  = C1_mol./(C1_mol+C2_mol+C3_mol); % Ratio of HF
X2_nd  = C2_mol./(C1_mol+C2_mol+C3_mol);
X3_nd  = C3_mol./(C1_mol+C2_mol+C3_mol);
X1_2d  = C1_mol./(C1_mol+C2_mol+C3_mol);
X2_2d  = C2_mol./(C1_mol+C2_mol+C3_mol);
X3_2d  = C3_mol./(C1_mol+C2_mol+C3_mol);
%{'Si','Al','K','F','Cl','H','O'};
Nsys0 = [0 0 0 0 1 0 1 0 0]; % HF;
Nsys1 = [0 0 0 0 0 1 1 0 0]; % HCl
Nsys2 = [0 0 0 0 0 0 2 1 0]; % H2O
Nq    = [1 0 0 0 0 0 0 2 0]; % q;
Nw    = [0 0 0 0 0 0 2 1 0]; % H2O;
NNaCl = [0 0 0 1 0 1 0 0 0]; % NaCl
NKCl  = [0 0 1 0 0 1 0 0 0];  %KCl
NHCl  = [0 0 0 0 0 1 1 0 0];  %HCl
NAb   = [3 1 0 1 0 0 0 8 0];  %albite
NHF   = [0 0 0 0 1 0 1 0 0];  %HF
NMic  = [3 1 1 0 0 0 0 8 0];  %microcline
NNa2O = [0 0 0 2 0 0 0 1 0];  %Na2O
NK2O  = [0 0 2 0 0 0 0 1 0];
id = X1_nd(:)+X2_nd(:)<=1 & X1_nd(:)+X2_nd(:)>=0;
X1_nd = X1_nd(id);X2_nd = X2_nd(id);
% max number of iterations
options.nref     = 20;

% tolerance to stop iterations
options.eps_dg   = 1e-12;
```

```
53
54  % tolerance to stop iterations when z window becomes below this
55  options.dz_tol   = 1e-14;
56
57  % the window over which the refined grid is generated
58  options.z_window = ones(size(phs_name))*0.0085;
59
60  % the factor to determine new dz spacing
61  options.dz_fact  = ones(size(phs_name))*1.5;
62
63  % the factor to control how the z_window is narrowed each iteration
64  options.ref_fact = 1.5;
65
66  % show refinement graphically
67  options.disp_ref = 0;
68  options.solver   = 0;
69  parfor iPT = 1:length(X1_nd(:))
70      Nsys = Nsys0*X1_nd(iPT) + Nsys1*X2_nd(iPT) + Nsys2*(1-X1_nd(iPT)-
71          X2_nd(iPT)) + 15*Nw  +0.11*NMic+0.08*NAb+0.01*NK2O+0.05*NNa2O+
72          0.5*NNaCl+0.1*NKCl+0.3*Nq;
73      [alph_all{iPT},Npc_all{iPT},pc_id_ref{iPT},p_ref{iPT},g_min{iPT}] =
74          tl_minimizer(T,P,Nsys,phs_name,p,td,options);
75      disp(iPT/length(X1_nd(:)))
76  end
77  save(['linprog_run_' run_name],'-v7.3');%Save results
78
```

Post processing code to calculate the Lookup tables

```
clear,figure(1),clf,addpath ../ ../Utilities/ ../Solutions/
% abbrevations of mineral names
phs_abbr = {'F','Qtz','Kfs','Ab','Tpz','Ms','And','Syl','Hlt','Cor'};%
load('linprog_run_ternary_Tpz_320_15w_r150.mat');
molm     = molmass_fun(Cname); %molar mass of elements
solv_tol  = 100;
fluid     = phs_name(1);
% Initialization of the variables

%mineral modes
phs_modes = zeros(length(X1_nd(:)),length(phs_name));
%fluid components
Cf       = zeros(length(X1_nd(:)),length(Cname));
Nf       = zeros(length(X1_nd(:)),length(Cname));
Ns       = zeros(length(X1_nd(:)),length(Cname));
% fluid components in weight percent
p_fl_wt   = zeros(length(X1_nd(:)),length(td(1).p_name));
%fluid components in m/kg
Cf_p      = zeros(length(X1_nd(:)),length(td(1).p_name));
%solid components in m/kg
Cs       = zeros(length(X1_nd(:)),length(Cname));
%density of fluid
rhof_tab  = zeros(length(X1_nd(:)),1);
%density of solid
rhos_tab  = zeros(length(X1_nd(:)),1);
%volume ratio of fluid
phif_tab  = zeros(length(X1_nd(:)),1);
%volume ratio of solid
```

```
phis_tab  = zeros(length(X1_nd(:)),1);
iT = 1;% index for a specific T
% Postprocessing
for iPT = 1:length(X1_nd(:))
    [pc_id,phi,Cwt,Npc,rho,mu,p_out,phiw,g,alph] =
        postprocess_fun(T,P,td,alph_all{iPT},Npc_all{iPT},molm,p_ref{iPT},pc_id_ref{iPT},phs_name,
        solv_tol,'CORK','S14');
    asm_id(iPT,1:length(phi)) = pc_id;
    phs_modes(iPT,pc_id) = phi;
    fluid_id =  strcmp(phs_name(pc_id),fluid);
    solid_id = ~strcmp(phs_name(pc_id),fluid);
    if sum(fluid_id)>0 %kick out the value below 0 for the fluid components
        Cf(iPT,:)    = Cwt(:,fluid_id)*phiw(fluid_id)/sum(Cwt(:,fluid_id)*phiw(fluid_id));
        Nf(iPT,:)    = Npc(:,fluid_id);
        Cf_p(iPT,:)  = p_out{pc_id(fluid_id)};
        p_fl_wt(iPT,:) = (p_out{1}.*(molm'*td(1).n_em'))/(p_out{1}*(molm'*td(1).n_em')');
        rhof_tab(iPT) = rho(fluid_id)'*phi(fluid_id)/sum(phi(fluid_id));
        phif_tab(iPT) = phi(fluid_id);
    end
    if sum(solid_id)>0 %look for the stable phase
        rhos_tab(iPT) = rho(solid_id)'*phi(solid_id)/sum(phi(solid_id));
        phis_tab(iPT) = sum(phi(solid_id));
        Cs(iPT,:)    = Cwt(:,solid_id)*phiw(solid_id)/sum(Cwt(:,solid_id)*phiw(solid_id));
        Ns(iPT,:)    = Npc(:,solid_id)*alph(solid_id)/sum(alph(solid_id));
    end
end

solid_id   = find(~strcmp(phs_name,fluid));
solid_names = phs_name(solid_id);
solid_abbr  = phs_abbr(solid_id);
```

```
%calculate the mineral abundance
vol_frac_solids = phs_modes(:,solid_id)./sum(phs_modes(:,solid_id),2);
solid_names = solid_names(sum(vol_frac_solids)>0);
solid_abbr = solid_abbr(sum(vol_frac_solids)>0);
vol_frac_solids = vol_frac_solids(:,sum(vol_frac_solids)>0);
chk_phi = phis_tab-(1-phif_tab);max(chk_phi(:))
Cf_wt = Cf;%weight fraction
Cs_wt = Cs;
% Re-organize the variables into grid points
Csys1_2d        = C1_2d;
Csys2_2d        = C2_2d;
[x2d,y2d]       = cart2bary(C1_2d,C2_2d);
asm_id_all      = zeros(length(X1)*length(X2)*length(T)*length(P),size(asm_id,2));
asm_id_all(id,:) = asm_id;
asm_id          = reshape(asm_id_all,[length(X1)*length(X2),length(T),size(asm_id,2)]);
Cf_all      = zeros(length(X1)*length(X2)*length(T)*length(P),size(Cf,2));
Cf_all(id,:) = Cf_wt;
Cf          = reshape(Cf_all,[length(X1),length(X2),length(T),size(Cf,2)]);
Nf_all      = zeros(length(X1)*length(X2)*length(T)*length(P),size(Nf,2));
Nf_all(id,:) = Nf;
Nf          = reshape(Nf_all,[length(X1),length(X2),length(T),size(Nf,2)]);
Cf_p_all      = zeros(length(X1)*length(X2)*length(T)*length(P),size(Cf_p,2));
Cf_p_all(id,:) = Cf_p;
Cf_p          = reshape(Cf_p_all,[length(X1),length(X2),length(T),size(Cf_p,2)]);
Cs_tpz_all      = zeros(length(X1)*length(X2)*length(T)*length(P),size(Ctpz,2));
reshape(Cs_tpz_all,[length(X1),length(X2),length(T),size(Ctpz,2)]);
pwt_fluid_all      = nan(length(X1)*length(X2)*length(T)*length(P),size(p_fl_wt,2));
pwt_fluid_all(id,:) = p_fl_wt;
pwt_fluid          = reshape(pwt_fluid_all,[length(X1),length(X2),length(T),size(p_fl_wt,2)]);
```

```
Cs_all      = zeros(length(X1)*length(X2)*length(T)*length(P),size(Cs,2));
Cs_all(id,:) = Cs_wt;
Cs          = reshape(Cs_all,[length(X1),length(X2),length(T),size(Cs,2)]);
phs_modes_all      = zeros(length(X1)*length(X2)*length(T)*length(P),size(phs_modes,2));
phs_modes_all(id,:) = phs_modes;
phs_modes          = reshape(phs_modes_all,[length(X1),length(X2),length(T),size(phs_modes,2)]);
vol_frac_solids_all      = zeros(length(X1)*length(X2)*length(T)*length(P),size(vol_frac_solids,2));
vol_frac_solids_all(id,:) = vol_frac_solids;
vol_frac_solids          =
reshape(vol_frac_solids_all,[length(X1),length(X2),length(T),size(vol_frac_solids,2)]);
rhos_all      = zeros(length(X1)*length(X2)*length(T)*length(P),size(rhos_tab,2));
rhos_all(id,:) = rhos_tab;
rhos_tab      = reshape(rhos_all,[length(X1),length(X2),length(T)]);
rhof_all      = zeros(length(X1)*length(X2)*length(T)*length(P),size(rhof_tab,2));
rhof_all(id,:) = rhof_tab;
rhof_tab      = reshape(rhof_all,[length(X1),length(X2),length(T)]);
phif_all      = zeros(length(X1)*length(X2)*length(T)*length(P),size(phif_tab,2));
phif_all(id,:) = phif_tab;
phif_tab      = reshape(phif_all,[length(X1),length(X2),length(T)]);
% look for the points with sum of HF and HCl over 1
[i_nan,j_nan] = find(X1_2d+X2_2d>1);

% phase diagram
tl_psection(x2d,y2d,Cname,squeeze(asm_id(:,iT,:)),phs_abbr,1,[0,0],8);axis off,axis square;text(1.2,-
0.01,'HF','FontSize',18),text(0.55,1.05,'HCl','FontSize',18),text(-0.1,-0.01,'H_2O','FontSize',18)
set(gca, 'FontSize', 18);

for i = 1:length(i_nan)
    vol_frac_solids(i_nan(i),j_nan(i),:,:) = nan;
end
```

```
118
119  %mineral abundance
120  figure(2),clf,colormap jet
121  ncol = floor(sqrt(length(solid_names)));
122  nrow = ceil(length(solid_names)/ncol);
123  for ip = 1:length(solid_names)
124      subplot(nrow,ncol,ip),pcolor(x2d,y2d,
125          squeeze(vol_frac_solids(:,:,1,ip))),title(solid_names(ip)),colorbar,shading flat,axis([0 1/sind(60) 0
126          1]),axis off,axis square
127  end
128
129  %concentration of fluid components
130  for ic=1:length(Cname)
131      figure(ic+2)
132
133      tl_psection(x2d,y2d,Cname,squeeze(asm_id(:,iT,:)),phs_abbr,1,[0,0],8);
134      hold on
135      if ic==3
136          contourf(x2d,y2d,squeeze(Cf(:,:,1,ic)),[0 0.01 0.012 0.014 0.016 0.018 0.02 0.022 0.024  0.026
137              0.0263 0.028],'ShowText','on','Color','r'),title(Cname(ic)),colormap sky,colorbar,shading
138              flat,axis([0 1/sind(60) 0 1]),axis off,axis square
139      else
140          contourf(x2d,y2d,squeeze(Cf(:,:,1,ic))),title(Cname(ic)),colormap sky,colorbar,shading flat,axis([0
141              1/sind(60) 0 1]),axis off,axis square
142      end
143  end
```

Calculate the fluid speciations based on the Lookup table

```
clear, clf
addpath ../,addpath ../Solutions/, addpath ../Utilities/, addpath ../EOS
load lookup_ternary_Tpz_320_15w_r150
Nf_tab       = Nf(:,:,iT,:);
% Input for fluid speciation
T            = 320 + 273.15;
P            = 1e8;
solvent      = {'H2O,tc-ds633'};
% fluid phase to consider
spcs         =
{'H+,Miron','OH-,Miron','HF,aq,supcrt','Cl-,Miron','HCl0,Miron','K+,Miron','Na+,Miron','F-,supcrt','K
Cl0,Miron','KOH0,Miron','NaCl0,Miron','NaOH0,Miron','SiO20,Miron','Al(OH)30,Miron'};
spcs_name    = {'H+','OH-','HF^0','Cl^-','HCl^0','K^+','Na^+','F^-
','KCl^0','KOH^0','NaCl^0','NaOH^0','SiO2,aq'};
Cname_spcs   = {'K','F','Cl','Na','H','O','Si','Al','e'};
flspcs       = [solvent,spcs];
td_spcs      = init_thermo(flspcs,Cname_spcs);
[g0,Nphs]    = tl_gibbs_energy(T,P,flspcs,td_spcs);
[rho_w,eps_di] = water_props(T,P,{'H2O,tc-ds633'},'JN91','JN91');
indep_id     = 1:4;
% bulk composition of fluid
B(1,:)  = reshape(Nf_tab(:,:,strcmp(Cname,'K')),size(Nf_tab,1)*size(Nf_tab,2),size(Nf_tab,3));
B(2,:)  = reshape(Nf_tab(:,:,strcmp(Cname,'F')),size(Nf_tab,1)*size(Nf_tab,2),size(Nf_tab,3));
B(3,:)  = reshape(Nf_tab(:,:,strcmp(Cname,'Cl')),size(Nf_tab,1)*size(Nf_tab,2),size(Nf_tab,3));
B(4,:)  = reshape(Nf_tab(:,:,strcmp(Cname,'Na')),size(Nf_tab,1)*size(Nf_tab,2),size(Nf_tab,3));
[g_fl,N_fl,molality,chk,logK,v] = tl_fluid_spec(T,B,solvent,spcs,indep_id,g0,Nphs,rho_w,eps_di);
molality(X1_2d+X2_2d>1,:) = nan;
% Calculate the variables
pH_tab = reshape(-log10(molality(:,1)),size(Csys1_2d,1),size(Csys1_2d,2));
```

```
H_tab  = reshape(molality(:,1),size(Csys1_2d,1),size(Csys1_2d,2));
HF_tab  = reshape(molality(:,3),size(Csys1_2d,1),size(Csys1_2d,2));
F_tab  = reshape(molality(:,8),size(Csys1_2d,1),size(Csys1_2d,2));
HCl0_tab= reshape(molality(:,5),size(Csys1_2d,1),size(Csys1_2d,2));
F_tal=HF_tab+F_tab;
Na_tab= reshape(molality(:,7)+molality(:,11)+molality(:,12),size(Csys1_2d,1),size(Csys1_2d,2));
K_tab= reshape(molality(:,6)+molality(:,9)+molality(:,10),size(Csys1_2d,1),size(Csys1_2d,2));
Cl_tab=reshape(molality(:,4)+molality(:,5)+molality(:,9)+molality(:,11),size(Csys1_2d,1),size(Csys1_
2d,2));
figure(1)  %Fig. 11a
tl_psection(x2d,y2d,Cname,squeeze(asm_id(:,iT,:)),phs_abbr,1,[0,0],8);
axis([0 1/sind(60) 0 1]),axis off,axis square;text(1.2,-0.01,'HF','FontSize',18),
text(0.55,1.05,'HCl','FontSize',18),text(-0.1,-0.01,'H_2O','FontSize',18);
set(gca, 'FontSize', 25);
hold on,[C,h]=contour(x2d,y2d,pH_tab,[2.0  2.5  3 3.5 4 4.5 5 5.5 6],'ShowText','on','Color','b'),
shading flat, colormap sky,clabel(C,h,'FontSize',30),axis([0 1/sind(60) 0 1]),
axis off,axis square,set(gca,'FontSize',18);
figure(2) %Fig. 11b
tl_psection(x2d,y2d,Cname,squeeze(asm_id(:,iT,:)),phs_abbr,1,[0,0],8);axis([0 1/sind(60) 0 1]),
axis off,axis square;text(1.2,-0.01,'HF','FontSize',18),
text(0.55,1.05,'HCl','FontSize',18),text(-0.1,-0.01,'H_2O','FontSize',18);
hold on,[C,h]=contour(x2d,y2d,F_tal,[0 0.0001  0.005 0.01 0.015 0.02 0.025 0.03 0.035
0.04],'ShowText','on','Color','r'),
shading flat, colormap sky, clabel(C,h,'FontSize',30),
axis([0 1/sind(60) 0 1]),axis off,axis square;
save fluid_speciation_ternary_Tpz_320_15w_r150 pH_tab HF_tab F_tab Na_tab K_tab H_tab
```

Reactive transport code

```
clear,figure(1),clf,colormap jet,figure(2),clf,colormap jet,addpath ../,addpath ../Solutions/,
addpath ../Utilities/ ../EOS
load lookup_ternary_Tpz_320_15w_r150
load fluid_speciation_ternary_Tpz_320_15w_r150
iT          = 1;
Nf_tab      = Nf(:,:,iT,:);
Cs_tab      = Cs(:,:,iT,:);
Cf_tab      = pwt_fluid(:,:,iT,:);
Cf_p_tab    = Cf_p(:,:,iT,:);
Cs_im_tab   = squeeze(Cs(:,:,iT,strcmp(Cname,'Al')));
rhos_tab    = rhos_tab(:,:,iT)/max(rhos_tab(:));
rhof_tab    = rhof_tab(:,:,iT)/max(rhof_tab(:));
phif_tab    = phif_tab(:,:,iT);
phs_modes_tab = squeeze(vol_frac_solids(:,:,iT,:));
asm_id      = squeeze(asm_id(:,iT,:));
asm_id(X1_2d+X2_2d>1,:,:) = nan;
% Input for fluid speciation
T           = 320 + 273.15;
P           = 1e8;
solvent     = {'H2O,tc-ds633'};
spcs        =
{'H+,Miron','OH-,Miron','HF,aq,supcrt','Cl-,Miron','HCl0,Miron','K+,Miron','Na+,Miron','F-,supcrt','K
Cl0,Miron','KOH0,Miron','NaCl0,Miron','NaOH0,Miron','SiO20,Miron'};
spcs_name   = {'H+','OH-','HF^0','Cl^-','HCl^0','K^+','Na^+','F^-
','KCl^0','KOH^0','NaCl^0','NaOH^0','SiO20'};
Cname_spcs  = {'K','F','Cl','Na','H','O','Si','e'};%'Si','Al',
flspcs      = [solvent,spcs];
td_spcs     = init_thermo(flspcs,Cname_spcs);
[g0,Nphs]   = tl_gibbs_energy(T,P,flspcs,td_spcs);
```

```
[rho_w,eps_di] = water_props(T,P,{'H2O,tc-ds633'},'JN91','JN91');
indep_id       = 1:4;

% Physics
Lx   = 1;
Dc   = 1;
qD   = 10; %50
nmob = [10,1]; % HF, HCl
Cini = [0.0005,0.25];   % background
% Boundary composition
Cbnd = [0.137 0.48];    % 134000   run a
%Cbnd = [0.16 0.48];    % 159000   run b
%Cbnd = [0.5 0.4];      % 22000    run d
%Cbnd = [0.2828 0.647]; % 16000    run c
% Look for the line
% Cbnd = [0.235 0.58];  %middle
% Cbnd = [0.2 0.53];  %middle
% Cbnd = [0.164 0.48]; %middle
% Cbnd = [0.306 0.68]; %middle
% Cbnd = [0.2707 0.63]; %middle

% Numerics
nx = 300; % grid numbers
nt = 134000; %Number of time steps
nout = 1000; % Maxium number of Pf iterations
% Preprocess
dx = Lx/(nx-1); %step size
x  = 0:dx:Lx; %Domain length
% Initialize
```

```
% Initial system composition
Csys      = ones(nx,length(nmob)).*repmat(Cini,nx,1);
% Set the boundary composition for the system
Csys(1,:) = Cbnd;
Cf        = zeros(size(Csys)); %Initial fluid composition
Cs        = zeros(size(Csys)); %Initial solid composition
phs_modes = zeros(nx,length(solid_names)); %Initial mineral modes
Crhotot   = zeros(nx,length(nmob)); %
phi       = zeros(nx,1) + 0.005; %Initial porosity

% Process
cnt=0;
for it = 1:nt %Time loop
   % Local equilibrium density in solid from lookup table
   rhos  = interpn(Csys1_2d,Csys2_2d,rhos_tab,Csys(:,1),Csys(:,2));
   % Local equilibrium density in fluid from lookup table
   rhof  = interpn(Csys1_2d,Csys2_2d,rhof_tab,Csys(:,1),Csys(:,2));
   % Local equilibrium Al in fluid from lookup table
   Cs_im = interpn(Csys1_2d,Csys2_2d,Cs_im_tab,Csys(:,1),Csys(:,2));
   % Store initial values
   if it == 1,phi_srho_sCs_im0 = (1 - phi).*rhos.*Cs_im;end
   % mass balance of immobile species in solid
   phi               = 1 - phi_srho_sCs_im0./(Cs_im.*rhos);
   phi(phi<0)= 0;phi(phi>1)=1;
   % Shorthand notation
   rhot   = phi.*rhof + (1-phi).*rhos;
   rhotc  = 0.5*(rhot(1:end-1) + rhot(2:end));
   rhofc  = 0.5*(rhof(1:end-1) + rhof(2:end));
   % phi value between the nodes
```

```
88      phic   = 0.5*(phi(1:end-1) + phi(2:end));
89      % interpolation using Csys in wt frac
90      for i_mob = 1:length(nmob)
91              Cf(:,i_mob)=interpn(Csys1_2d,Csys2_2d,Cf_tab(:,:,nmob(i_mob)),Csys(:,1),Csys(:,2));
92         Crhotot(:,i_mob)    = Csys(:,i_mob).*rhot;
93      end
94      % time step
95         dt=min(dx^2/max(abs(Dc*rhofc.*phic)./rhotc)/2.1,0.45*dx/max(abs(rhof./rhot.*qD)));
96      for i_mob = 1:length(nmob)
97         % incomplete diffusion flux
98         qC = -Dc*rhofc.*phic.*diff(Cf(:,i_mob))/dx;
99         % shortcut notation
100             rhofCfc = 0.5*(rhof(1:end-1).*Cf(1:end-1,i_mob) +rhof(2:end).*Cf(2:end,i_mob));
101        % Correct mass concentration balance, assuming Vx_s = 0;
102             Crhotot(2:end-1,i_mob) = Crhotot(2:end-1,i_mob) - dt*(diff(qC + rhofCfc.*qD)/dx);
103        % postprocess Csys in wt fraction
104        Csys(:,i_mob)         = Crhotot(:,i_mob)./rhot;
105     end
106     if sum(sum(Csys,2)>1)>0,break,end
107     Csys(Csys<0)= 0;Csys(Csys>1)=1;
108     if mod(it,nout)==0
109        cnt=cnt+1;
110        % bulk composition of fluid in mole
111             B(1,:)=interpn(Csys1_2d,Csys2_2d,Nf_tab(:,:,strcmp(Cname,'K')),Csys(:,1),Csys(:,2))';
112             B(2,:)=interpn(Csys1_2d,Csys2_2d,Nf_tab(:,:,strcmp(Cname,'F')),Csys(:,1),Csys(:,2))';
113            B(3,:)=interpn(Csys1_2d,Csys2_2d,Nf_tab(:,:,strcmp(Cname,'Cl')),Csys(:,1),Csys(:,2))';
114             B(4,:)=interpn(Csys1_2d,Csys2_2d,Nf_tab(:,:,strcmp(Cname,'Na')),Csys(:,1),Csys(:,2))';
115             [g_fl,N_fl,molality,chk,logK,v]=tl_fluid_spec(T,B,solvent,spcs,indep_id,g0,Nphs,rho_w,eps
116             _di);
117        for ip = 1:length(solid_names)
```

```
                phs_modes(:,ip)=interpn(Csys1_2d,Csys2_2d,phs_modes_tab(:,:,ip),Csys(:,1),Csys(:,2)
                );
    end
    % Variable values of grid nodes
        HF_fluid=
        interpn(Csys1_2d,Csys2_2d,Cf_tab(:,:,2),Csys(:,1),
        Csys(:,2))';
        HCl_fluid  = interpn(Csys1_2d,Csys2_2d,Cf_tab(:,:,1),Csys(:,1),Csys(:,2))';
       Na_solid=interpn(Csys1_2d,Csys2_2d,Cs_tab(:,:,strcmp(Cname,'Na')),Csys(:,1),Csys(:,2));
       K_solid=interpn(Csys1_2d,Csys2_2d,Cs_tab(:,:,strcmp(Cname,'K')),Csys(:,1),Csys(:,2));
       F_solid=interpn(Csys1_2d,Csys2_2d,Cs_tab(:,:,strcmp(Cname,'F')),Csys(:,1),Csys(:,2));
       Si_solid=interpn(Csys1_2d,Csys2_2d,Cs_tab(:,:,strcmp(Cname,'Si')),Csys(:,1),Csys(:,2));
       Al_solid=interpn(Csys1_2d,Csys2_2d,Cs_tab(:,:,strcmp(Cname,'Al')),Csys(:,1),Csys(:,2));
    H_aq      = interpn(Csys1_2d,Csys2_2d,H_tab,Csys(:,1),Csys(:,2))';
    F_aq      = interpn(Csys1_2d,Csys2_2d,F_tab,Csys(:,1),Csys(:,2))';
    f1=figure(1);clf
    % mineral modes profile
    subplot(211),colororder(['b';'r']),yyaxis left,a=area(x,phs_modes);
    ylabel('Mineral modes'),set(gca,'yminortick','on'),axis tight,
    legend(solid_abbr);title(['it =  ' num2str(it)]);
        set(gca,'XDir','normal','xminortick','on','yminortick','on','FontSize',30);yyaxis right,...
    plot(x,phi,'-r','Linewidth',3),ylabel('\phi'),ylim([0 0.16]),...
    % plot porosity on the top of mineral modes profile
    ylabel('\phi'),legend([solid_abbr  '\phi']);
        a(1).FaceColor='#FFFF00';a(2).FaceColor='#00FD90';a(3).FaceColor='#FF819B';a(5).Face
        Color='#535026';a(4).FaceColor='#7E2F8E';a(6).FaceColor='#FEFEFE';
    xticks([0 0.1 0.2 0.3 0.4 0.5 0.6 0.7 0.8 0.9 1]);
    % plot fluid pH value and F
    subplot(212),colororder(['b';'r']),yyaxis left,
    plot(x,-log10(molality(:,1)),'Linewidth',3,'Color','b'),
```

```
148         ylim([2 6]),ylabel('pH'),yyaxis right,
149         plot(x,molality(:,3)+molality(:,8),'Linewidth',3,'Color','r'),
150         ylim([0 6*10^-5]), ylabel('F,aq (mole/kg)');legend('pH','F,aq'),
151               set(gca,'XDir','normal','xminortick','on','yminortick','on','FontSize',30);
152         xticks([0 0.1 0.2 0.3 0.4 0.5 0.6 0.7 0.8 0.9 1]);
153         [Xsys1,Xsys2] = cart2bary(Csys(:,1),Csys(:,2));
154         [Xf1,Xf2]     = cart2bary(HF_fluid,HCl_fluid);
155         % plot pH and F on the top of phase diagram
156         figure(2),
157               [asm_name,asm_legend,asm_ind] =
158               tl_psection(x2d,y2d,Cname,asm_id,phs_abbr,1,[0,0],8);axis([0 1/sind(60) 0 1]),
159               Axis off,axissquare;text(1.2,0.01,'HF','FontSize',18),
160               text(0.55,1.05,'HCl','FontSize',18),
161         text(-0.1,-0.01,'H_2O','FontSize',18)
162         hold on,
163               [c,h]=contour(x2d,y2d,pH_tab,[2 2.1 2.2 2.3 2.4 2.5 2.6 2.7 2.8 2.9 3 5.8 5.9  6 6.1 6.2 ],'--
164               ','Color','b');clabel(c,h,'FontSize',20);
165              [c,h]=contour(x2d,y2d,F_tab,[ 0.001    0.003 0.005  0.01  0.015  0.02  0.025  0.03  0.035
166              0.04],'--','Color','r');axis([0 1/sind(60) 0 1]),axis off,axis square;clabel(c,h,'FontSize',20);
167         % Reaction path
168               plot(Xsys1,Xsys2,'o','LineWidth',4,'Color','#91D8F7','MarkerFaceColor','#91D8F7','MarkerE
169               dgeColor','none','MarkerSize',12);
170         drawnow
171       end
172   end
173   Solid=[Si_solid,Al_solid,Na_solid,K_solid];
174   solidname={'Si,s','Al,s','Na,s','K,s'};
175
176   %save the data into table
177   V=[x',Solid,phs_modes,molality,phi,-log10(molality(:,1))];
178   [m,n]=size(V);
```

```
179 data_cell=mat2cell(V,ones(m,1),ones(n,1));
180 title=['Distance',solidname,solid_abbr,spcs_name,'porosity','pH'];
181 result=[title;data_cell];
182 filename='tpzms1.xls';
183 xlswrite(filename,result);
```

Related Publications and Conference Contributions

Publications

1. Anselm Loges, Marco Manni, Marion Louvel, Max Wilke, Sandro Jahn, Edmund Welter, Manuela Borchert, **Shilei Qiao**, Stephan Klemme, Bettina G. Keller, Timm John, 2024. Complexation of Zr and Hf in fluoride-rich hydrothermal aqueous fluids and its significance for high field strength element fractionation, Geochimica et Cosmochimica Acta, 366: 167-181.

2. **Shilei Qiao**, Timm John, Anselm Loges, 2024. Formation of topaz-greisen by a boiling fluid: a case study from the Sn-W-Li deposit, Zinnwald/Cínovec. Economic Geology, 119: 805-828.

3. **Shilei Qiao**, Anselm Loges, Johannes C. Vrijmoed, Timm John, 2024. Controls of F content and pH on the formation of greisen quantified by reactive transport modeling, Geochimica et Cosmochimica Acta (under review).

4. Anselm Loges, **Shilei Qiao**, Xin Zhong and Timm John, 2024. Determination of Fluorine Concentration in Topaz Using Raman Spectroscopy, American Mineralogist (in prep.).

Conferences

1. **Shilei Qiao**, Anselm Loges, Timm John, 2022 May, EGU General Assembly 2022, Vienna, Austria. Element redistribution by greisenization in rhyolite, Zinnwald/Cínovec (Oral presentation).

2. **Shilei Qiao**, Anselm Loges, Johannes C. Vrijmoed, Timm John, 2023 September, GeoBerlin 2023, Berlin, Germany. Numerical modeling unravels differences in greisenization processes (Oral presentation).